PLASMONICALLY ENHANCED HOT ELECTRON BASED OPTOELECTRONIC DEVICES

A DISSERTATION SUBMITTED TO

THE GRADUATE SCHOOL OF ENGINEERING AND SCIENCE

OF BILKENT UNIVERSITY

IN PARTIAL FULFILLMENT OF THE REQUIREMENTS FOR

THE DEGREE OF

DOCTOR OF PHILOSOPHY

IN

ELECTRICAL AND ELECTRONICS ENGINEERING

By

Fatih Bilge Atar

June, 2015

PLASMONICALLY ENHANCED HOT ELECTRON BASED OPTOELECTRONIC DEVICES

By Fatih Bilge Atar

June, 2015

We certify that we have read this thesis and that in our opinion it is fully adequate, in scope and in quality, as a dissertation for the degree of Doctor of Philosophy.

Assist. Prof. Dr. Ali Kemal Okyay(Advisor)

Prof. Dr. Mehmet Bayındır

Assoc. Prof. Dr. Hilmi Volkan Demir

Assoc. Prof. Dr. Mustafa Alevli

Assist. Prof. Dr. İbrahim Yılmaz

Approved for the Graduate School of Engineering and Science:

Prof. Dr. Levent Onural
Director of the Graduate School

ABSTRACT

PLASMONICALLY ENHANCED HOT ELECTRON BASED OPTOELECTRONIC DEVICES

Fatih Bilge Atar
Ph.D. in Electrical and Electronics Engineering
Advisor: Assist. Prof. Dr. Ali Kemal Okyay
June, 2015

Hot electron based optoelectronic devices have been regarded as cost-effective candidates to their conventional counterparts. The efficiency of conventional optoelectronic devices that rely on semiconductor photo-absorbers are mainly limited by the energy bandgap of the semiconductor. On the other hand, hot electron devices can overcome this limitation via the "internal photoemission" mechanism. Absorbed photons give their energy to free electrons of the metal and these high energy ("hot") electrons can be used to generate photocurrent in proper device configurations. High optical reflection from metals has remained as the main drawback of this photocurrent generation scheme but this problem has recently been addressed by the use of surface plasmons. Optical energy can be tightly confined to a metal layer or metal nanostructures in the form of surface plasmons, and the decay of surface plasmons in metals generates hot electrons.

In this work, we study mechanisms of surface plasmon excitation, surface plasmon decay, hot electron generation and hot electron photoemission for photocurrent generation. We demonstrate novel device architectures and plasmon excitation structures. We demonstrate the use of such layers for plasmon enhanced hot electron based photodetectors and photovoltaic devices. A metal-semiconductor Schottky junction diode structure is used as hot electron photodetector. A double metal-insulator-metal (MIM) architecture is proposed as a hot electron photovoltaic device. Full wave electromagnetic simulations of these device structures are conducted to provide insight into the surface plasmon assisted hot electron generation process and give future directions in this field.

Keywords: Hot electron, surface plasmon, optoelectronics, internal photoemission, photodetectors, photovoltaics.

ÖZET

PLAZMON DESTEKLİ SICAK ELEKTRON TABANLI OPTOELEKTRONİK AYGITLAR

Fatih Bilge Atar
Elektrik ve Elektronik Mühendisliği, Doktora
Tez Danışmanı: Assist. Prof. Dr. Ali Kemal Okyay
Haziran, 2015

Sıcak elektron tabanlı optoelektronik aygıtlar geleneksel aygıtların düşük maliyetli alternatifleri olarak ilgi görmüşlerdir. Bilinen optoelektronik aygıtların verimi çoğunlukla ışık soğurucu olarak kullanılan yarı-iletkenin enerji bant aralığıyla limitlidir. Öte yandan sıcak elektron aygıtları iç fotoemisyon mekanizması ile bu limiti aşabilmektedirler. Bir metal içerisinde emilen fotonlar sahip oldukları enerjiyi metalin serbest elektronlarına vererek elektronları daha yüksek enerji seviyelerine çıkartırlar. Yüksek enerjiye sahip bu sıcak elektronlar uygun aygıt yapılarında fotoakım üretmek için kullanılabilirler. Bu yöntemin önündeki en büyük engel, metal yüzeylerin yansıtıcı özelliğe sahip olmalarıdır. Yüzey plazmonlarının kullanılması bu engelin önemli ölçüde aşılmasını sağlamıştır. Işık enerjisi, yüzey plazmonları halinde metal katmanlara veya metal nanoparçacıklara hapsedilerek metal içerisindeki ışık emiliminin artması sağlanır. Bu sayede metal içerisindeki sıcak elektron oluşma hızı da artırılır.

Bu çalışmada yüzey plazmonlarının tetiklenme ve sönümlenme mekanizmaları, yüzey plazmonlarının sönümlenmesi ile sıcak elektron oluşumu ve sıcak elektronların fotoemisyonuyla fotoakım oluşumu incelenmiştir. Özgün aygıt mimarileri ve plazmon tetikleme yapıları üzerine çalışılmış ve bu yapılarla plazmon destekli sıcak elektron tabanlı fotodedektörler ve fotovoltaik aygıtlar gösterilmiştir. Metal-yarıiletken Schottky eklem diyot yapısı sıcak elektron tabanlı fotodedektör olarak kullanılmıştır. Çift katlı metal-yalıtkan-metal (MYM) mimarisi sıcak elektron tabanlı fotovoltaik aygıt olarak önerilmiştir. Bu aygıtların tam dalga elektromanyetik simulasyonları yapılarak plazmon destekli sıcak elektron oluşma mekanizması açıklanmış ve bu alanda yapılacak çalışmalar için yol gösterici bulgular sunulmuştur.

Anahtar sözcükler: Sıcak elektron, yüzey plazmonları, optoelektronik, iç fotoemisyon, fotodedektör, fotovoltaik.

Acknowledgement

I would like to start by expressing my deepest gratitude to Prof. Ali Kemal Okyay for his guidance and patience. He was an excellent supervisor and I am happy to be a member of his research team. I have learned a lot from him and I will always be grateful for everything he has done for me. Along with Prof. Okyay, I thank all Okyay Team members for the great time we have shared.

I would like to thank Prof. Mehmet Bayındır, Prof. Hilmi Volkan Demir, Prof. Mustafa Alevli and Prof. İbrahim Yılmaz for being members of my thesis committee and making this dissertation better with their valuable opinion.

I would like to acknowledge TÜBİTAK (The Scientific and Technological Research Council of Turkey) for providing me a Ph.D. scholarship and funding our research. I appreciate their generous support that enabled these studies. I have to thank The Department of Electrical and Electronics Engineering of Bilkent University and UNAM (National Nanotechnology Research Center) for providing the facilities and equipment for our research.

My 10-year-long stay in Bilkent has been an invaluable experience. I would like to thank Prof. İhsan Doğramacı, the founder of Bilkent University, and all Bilkent community for every joyful moment I spent in Bilkent. I also would like to thank all faculty members for the great education and inspiration they provided.

Finally, I would like to express my gratitude to my family. Any success I may have achieved would not have been possible without their love and support. Along with them, I have to thank many great friends who have been another family to me and contributed to this dissertation in many different ways. Undoubtedly, this dissertation is dedicated to *my family*.

Contents

List of Figures

List of Tables

Chapter 1

Introduction

Hot electron based optoelectronic devices have recently appeared as intriguing candidates for photodetection, photovoltaics and photocatalytic applications. The extremely low cost that the hot electron based devices offer compared to their conventional counterparts seem to be their most prominent advantage. The recent advances in the field of plasmonics have successfully addressed some key problems related to the hot electron based device technology and enabled a myriad of new approaches for highly efficient hot electron based devices. This study focuses on near infrared (NIR) photodetection with hot electron based devices and photovoltaic applications of hot electron based devices with a strong emphasis on plasmonic effects in these device architectures.

Direct conversion of the energy of surface plasmons to electrical energy by the generation of hot carriers in metals has been explored as an alternative approach for a new type of solar cell. This new solar energy conversion scheme is considered to have the potential to exceed the efficiencies of conventional devices and the fabrication costs are expected to be lower than single crystalline Si solar cells or amorphous thin film solar cells [1]. Hot electron based photovoltaic device architecture as proposed by Zhao *et al.* is illustrated in (Fig. 1.1) as an example [2]. Localized surface plasmon resonances (LSPR) are excited on Au or Ag nanoparticles upon solar illumination. The decay of surface plasmons results

in the generation of hot carriers in the metal, which are generally collected to a wide bandgap semiconductor such as TiO_2 or ZnO. The lost electrons of the metal nanoparticles must be regenerated for the hot electron generation process to continue. The basic principles and main limitations of this solar energy conversion scheme and the recent efforts to overcome these limitations are explained in the following chapters.

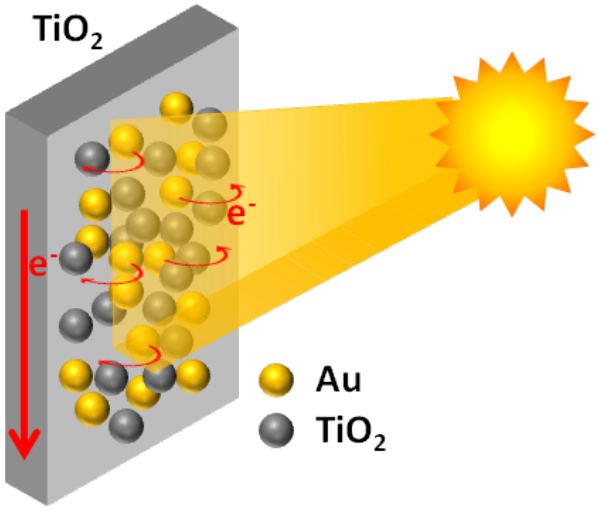

Figure 1.1: Schematic view of a hot electron based photovoltaic device architecture. Au nanoparticles are used to excite LSPR and TiO_2 is used to collect the generated hot electrons.

Surface plasmon assisted hot electron generation has also been employed in low-cost NIR photodetectors by making use of the sub-bandgap photodetection process. Despite their high cost, conventional NIR photodetectors have found extensive use in spectroscopy and imaging for biotechnology and pharmaceutical applications [3, 4]. Use of NIR photodetectors for surveillance applications has also gathered interest due to the outstanding performance of short-wave infrared (SWIR) cameras [5]. SWIR cameras can give a better view compared to visible cameras and thermal imagers, and have the capability to operate full day-night. Fig. 1.2 shows two images taken with SWIR and visible cameras for comparison [6]. The image taken with SWIR camera is not obscured by the fog since the light at longer wavelengths encounters much less scattering in the atmosphere (Rayleigh scattering $\propto 1/\lambda^4$). SWIR image has a clearer view and shows more detail compared to visible image. Despite the various applications and advantages

of NIR photodetectors, reducing the fabrication cost and expanding their use have been a challenge.

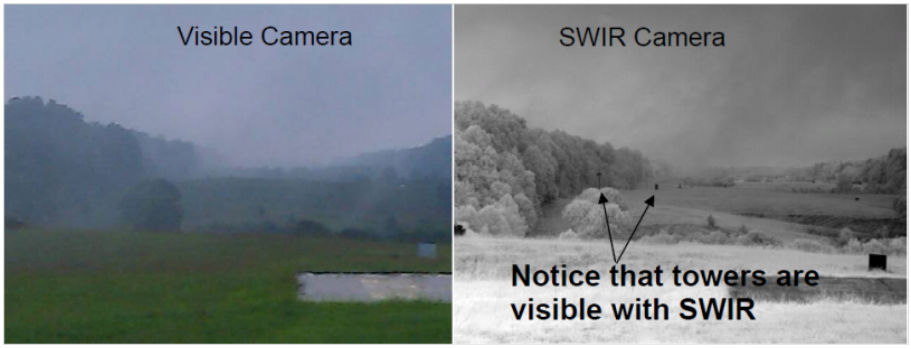

Figure 1.2: Comparison of two photographs taken with visible and SWIR cameras. The effect of fog is significantly smaller in the image taken with the SWIR camera due to the reduced scattering of light at longer wavelengths. Copyright 2011 Society of Photo Optical Instrumentation Engineers.

For any commercial photodetector configuration, the integration of the sensor with Si CMOS read-out circuitry is essential and this integration brings extra cost for most NIR photodetectors since Si itself does not detect NIR light. Heteroepitaxy of narrow-gap semiconductors such as Ge [7, 8] or the hybrid use of compound semiconductors become necessary [5]. These semiconductors have smaller bandgap energy compared to Si and they can absorb the near infrared light via band-to-band absorption process (Fig. 1.3(a)). Hot electron based photodetection, on the other hand, is a simple and efficient way to obtain NIR photodetectors monolithically fabricated on Si substrates along with the read-out circuitry. A metal in contact with a semiconductor forms a potential barrier (Schottky barrier) and this metal-semiconductor junction (Schottky junction) operates as a diode. Schottky barrier diodes can detect photons with energies lower than the energy bandgap of the semiconductor by absorbing the light in the metal layer (Fig. 1.3(b)). Photons absorbed in the metal layer give their energy to the electrons of the metal, exciting them to higher energy levels and these high energy electrons are then injected to the semiconductor. This process is the fundamental mechanism of hot electron based photodetection and is called the "internal photoemission process". Near infrared photodetection with the internal photoemission mechanism have been extensively studied since its first demonstration in

the 1960s.

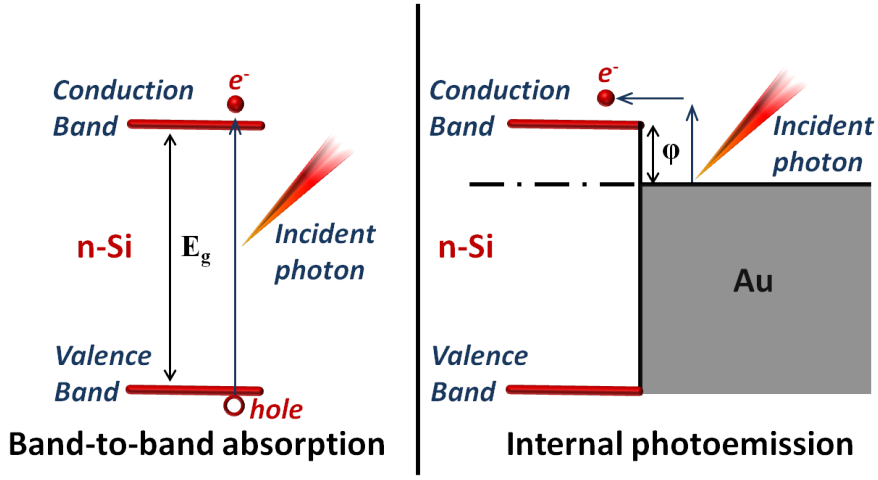

Figure 1.3: (a) Energy band diagram of n-type Si showing the conduction and valence bands. Absorption of an incident photon excites an electron from the valence band to the conduction band, leaving a hole in the valence band (band-to-band absorption). Only photons with energies ($h\nu$) greater than the energy bandgap (E_g) of Si are absorbed ($h\nu > E_g$) and can create electron-hole pairs. (b) Energy band diagram of ideal Au/n-Si Schottky junction where the work function of the metal is aligned with the Fermi level of the semiconductor. Absorption of an incident photon excites an electron of the metal to higher energy levels and this highly energetic electron can be collected to the semiconductor over the Schottky barrier. Ideally the energy of the photon ($h\nu$) must be greater than the Schottky barrier height (φ), which is usually much smaller than the energy bandgap (E_g) of Si. In practice, even the photons with energies smaller than the Schottky barrier height can contribute to the photocurrent.

In the internal photoemission process, the photons incident on a metal are absorbed by the metal and the absorbed photons transfer their energy to the electrons of the metal. The electrons of the metal are excited to the higher energy levels in the metal with the energy they received from the absorbed photons and these highly energetic electrons are called "hot electrons". Hot electrons travel with randomly oriented momenta in the metal and can be collected into a semiconductor to produce photocurrent in a metal-semiconductor Schottky junction. The electrons are emitted over the Schottky barrier with the energy they have received from the absorbed photon, completing the internal photoemission process. Exploiting the hot electron generation mechanism in metals for detection of sub-bandgap photons was demonstrated by Peters *et al.* in 1967 [9]. They

used an Au/n-Si Schottky barrier diode where the sub-bandgap photons were absorbed in the Au layer, generating hot electrons. The generated hot electrons are injected into the n-Si substrate and collected as photocurrent. Incident photon to current conversion efficiency of this mechanism strongly depends on three factors: the absorption probability in the metal layer, the collection efficiency of the photogenerated hot carriers from the metal and the rate of regeneration of the lost electrons back to the metal. The collection efficiency of the hot electrons is mainly governed by the Schottky junction. The main mechanisms of the internal photoemission process, the electrical properties of Schottky junctions and several factors that affect the charge collection mechanism at Schottky junctions are explained in Chapter 2.

Photodetection via the internal photoemission process has attracted great attention due to its simplicity, repeatability, low-cost and fabrication uniformity. However, the high reflection of metal surfaces has become the main drawback of this photodetection scheme. Electromagnetic waves at optical frequencies cannot properly penetrate into the metals used in Schottky barrier photodetectors. Hence, when photons are directly incident on a metal surface, a large portion of the incident photons are reflected back and only a small amount can propagate into the metal to be absorbed therein. Use of surface plasmons has emerged as a promising solution to this problem. In properly designed structures or optical configurations, surface plasmons can be excited on metal surfaces and the incident optical energy can be tightly confined to the metal layer. Surface plasmons can then decay by giving their energy to the electrons of the metal, and excite the electrons to higher energy levels. This process is called surface plasmon assisted hot electron generation. Chapter 3 describes the use of surface plasmons for hot electron generation in Schottky barrier devices. The theory and applications of surface plasmon assisted hot electron generation process are discussed together with a brief review of surface plasmon literature.

Many researchers have worked on different approaches in order to make use of surface plasmon assisted hot electron generation and enhance the coupling of the incident light to the metal layer of the Schottky barrier devices. Akbari *et al.* used a metal stripe plasmonic waveguide on Silicon surface. A surface plasmon

polariton (SPP) mode, strongly confined to the metal semiconductor interface, is supported on this plasmonic waveguide [10, 11]. Knight *et al.* demonstrated optical nanoantennas on Silicon to collect the incident near infrared light and excite surface plasmons to enhance the hot electron generation rate through surface plasmon decay [12]. Sobhani *et al.* achieved strongly resonant and narrowband photodetection in the infrared region of the spectrum with metallic gratings on Silicon [13]. The fabrication of the plasmonic structures used in such studies generally requires high resolution photolithography techniques, which greatly limits the integration of this approach to commercial photodetectors. We form randomly distributed and randomly sized Au nanoislands on Si substrate by rapid thermal annealing of a thin Au layer [14]. These nanoislands give broad-band plasmonic enhancement at the near infrared wavelengths and we demonstrate hot electron based photodetectors with photoresponsivity values on the same order as the narrow-band plasmonically tuned hot electron based photodetectors in the literature [12, 13]. Chapter 4 explains the device architecture of our hot electron based NIR photodetector and describes the experimental details including the device fabrication, nanoisland formation, dark current–voltage measurements and photoresponsivity measurements. A theoretical analysis based on finite-difference time-domain (FDTD) simulations is also presented.

Use of Si substrates for hot electron based photodetection is preferred to achieve CMOS compatible fabrication of Schottky barrier photodetectors operating at infrared wavelengths since the monolithic integration with the read-out circuitry is expected to substantially reduce the cost compared to the other infrared detector devices based on InGaAs, HgCdTe or SiGe compounds. On the other hand, for photovoltaic and photocatalytic applications the use of single crystalline Si substrates is still costly and limits large-area scalability. For hot electron based photovoltaic and photocatalytic applications, TiO_2 appears to be the most commonly used semiconductor material due to its large bandgap and high density of states (DOS) in its conduction band, allowing fast electron injection [1]. Many studies have been conducted using Au or Ag nanoparticles combined with TiO_2 semiconductors [15, 16, 17], and following these studies a variety of different materials and architectures have been proposed such as Ag-decorated TiO_2

nanotube arrays [18, 19], ZnO nanorods decorated with Au nanoparticles [20, 21], and coreshell SiO_2–TiO_2 nanoparticles decorated with Au nanoparticles [22]. On the other hand, another approach utilizes metal-insulator-metal (MIM) junctions without incorporating any conventional absorber or semiconductor [23, 24]. In our hot electron based photovoltaic studies, we follow the second approach and focus on metal-insulator-metal (MIM) device architectures [25]. An MIM device can be fabricated on any substrate with a sufficiently flat surface such as glass; hence low-cost and wide-area fabrication is possible. Surface plasmon excitation on an MIM photovoltaic device was demonstrated in a study by Wang *et al.*, where they used the Kretschmann configuration to excite surface plasmons at the MIM device fabricated on a prism and observed photovoltaic activity by increasing the absorption in one of the metal layers due to the highly localized surface plasmon mode [23]. The use of a prism for surface plasmon excitation is typically impractical for wide-area implementation of photovoltaic devices, hence different plasmon excitation schemes are necessary. In Chapter 5, we propose a double MIM structure for the excitation of plasmonic resonances under direct illumination. The device architecture is explained and the working principle of the device is supported with FDTD simulations and experimental results.

In addition to the use of surface plasmon excitation for hot electron based photodetection and photovoltaics, several groups have demonstrated the use of surface plasmon excitation on MIM structures for broad-band optical absorbers [26, 27, 28]. Nielsen *et al.* has shown that around 94% average optical absorption can be achieved in the visible wavelength range (400-750 nm) with an Au-SiO_2-Au stack [27]. Wadell *et al.* made an optical absorption engineering study with a nanodisc of Au-SiO_2-Pd stack. They show that MIM plasmonic nanoantennas incorporating Au as the metal layers can show strong resonance but this strong resonance alone is not enough for the efficient absorption of incident light. Hence they use an Au nanodisc to act as a plasmonic nanoantenna, which transfers the power to Pd nanodisc to be efficiently absorbed and dissipated [28]. An absorption engineering study is also possible for the double MIM device discussed in Chapter 5. We conduct FDTD simulations of this device architecture by using different metals and plasmonic structures, and investigate the optical absorption spectrum.

We show that careful design and material choice can allow the engineering of the absorption in such a structure. Narrow-band or broad-band resonances can be obtained and the optical absorption can be forced to occur mostly in the desired layer of the double MIM structure. The absorption spectrum can also be precisely tuned with the nanoantenna dimensions. The results of this absorption engineering study in double MIM structures are presented in Chapter 6.

Chapter 7 concludes this dissertation by briefly summarizing the results we have achieved with this study and gives future directions related to these topics.

Chapter 2

Hot Electron Based Photodetection

2.1 Internal Photoemission

When a metal is in contact with a semiconductor surface, a potential barrier develops between the two materials and a Schottky junction is formed. The energy band diagram of a Schottky junction is shown in Fig. 2.1. The energy barrier formed at this junction is known as the Schottky barrier. In a hot electron based photodetection scheme, photoexcited electrons in the metal that can overcome this Schottky barrier are collected at the semiconductor. The collection of the photoexcited hot electrons at the semiconductor is the "internal photoemission process".

The height of the Schottky barrier, φ, can be calculated as $\varphi = \Phi_M - \chi$ where Φ_M is the work function of the metal and χ is the electron affinity of the semiconductor [9]. Hot electrons with energies greater than the Schottky barrier height, φ, can be emitted to the semiconductor if the required momentum condition is satisfied. Hot electrons with energies lower than the Schottky barrier height can still tunnel to the semiconductor but the probability of photoemission

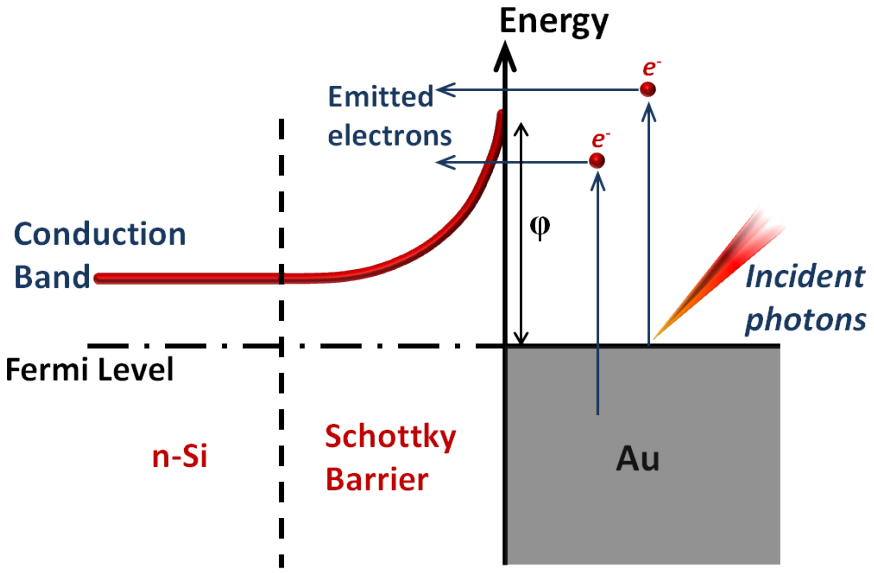

Figure 2.1: Energy band diagram of an Au/n-Si Schottky junction. Photons incident on the metal can excite the electrons of the metal to higher energy levels (hot electron generation) and these hot electrons can be emitted into the semiconductor to generate photocurrent (internal photoemission).

is significantly reduced in such a case.

The photoemission current at a junction with Schottky barrier height φ can be expressed as [9]:

$$I_S = A(h\upsilon)^2, \quad h\upsilon > \varphi + 3kT \tag{2.1}$$

where h is the Plancks constant, υ is the frequency of the incident light and A is a constant that does not depend on υ. The Schottky barrier height can be deduced by plotting the square root of the photoemission current (I_S) as a function of photon energy ($h\upsilon$) and extrapolating the linear region of the plot to the $I_S = 0$ point. A fundamental study related to photoemission process was conducted by Fowler [29]. The analysis in Fowlers study suggests that the change in different photoresponse spectra can be completely accounted for by the change of distribution of the electrons with the temperature. Namely, an electron with an initial energy E_x could be modeled as a "hot" electron with higher energy, $E_x + h\upsilon$, after the photoexcitation of the electron by a photon with energy $h\upsilon$. This excess energy lets the electron travel in the metal with increased momentum and gives the electron the necessary energy to overcome the Schottky barrier if

the electron can reach the metal-semiconductor junction. If the electron cannot be injected to the semiconductor, the excess energy received from the absorbed photon is eventually lost to the lattice vibrations and dissipated as heat [23]. The maximum length that an electron can travel without losing its excess energy is named as "mean free path" and depends on factors like the metal type and the total energy of the hot electron [30, 31].

The efficiency of photodetection via the internal photoemission process is typically low. Main limitations are the optical properties of metals (light penetration is low), the relatively short mean free path of hot electrons in metals (typically 10s of nms), the Schottky barrier height and the other electrical properties of the Schottky junction. These limitations bring an important design challenge that involves the thickness and optical properties of the metal, and requires careful optimization of the electrical properties of the Schottky junction.

2.2 Metal-Semiconductor (MS) Schottky Junction

The electrical properties of the Schottky junction are mainly governed by the electron affinity and Fermi level of the semiconductor and the work function of the metal. As shown in Fig. 2.1, at thermal equilibrium the work function of the metal and the Fermi level of the semiconductor are aligned at the same energy level. The energy difference between the electron affinity of the semiconductor and the work function of the metal has to be preserved at the metal-semiconductor junction and this difference sets the height of the potential energy barrier from the metal to the semiconductor ($\varphi = \Phi_M - \chi$). Since the Fermi energy of the semiconductor is smaller than the work function of the metal ($E_F < \Phi_M$), alignment of the Fermi level and the metal work function forces the energy bands of the semiconductor to be bent upwards at the junction, creating a built-in electric field from the bulk of the semiconductor to the metal. This electric field can be utilized to separate the electron-hole pairs that are generated in the semiconductor. Use of Schottky

diodes as photodetectors and solar cells rely on this mechanism to collect the photogenerated charge carriers in the semiconductor.

The choice of the direction of the built-in electric field has a crucial effect on the dark current performance of the Schottky diode. The majority carriers, in this case the electrons, of the n-type Si in Fig. 2.1 can not flow to the metal hence their contribution to the current is significantly reduced. This potential barrier is the main reason a voltage develops between the metal and the semiconductor upon optical illumination. When a metal with much smaller work function is in contact with the same semiconductor, the energy bands will bend downwards, resulting in a very small or no potential barrier, hence an ohmic contact. The dark current will substantially increase, making such a junction impractical for photodetection. Since there will be no potential barrier to stop the backflow of electrons, no voltage will build up upon optical illumination.

Ideally, one can engineer such electrical properties of a Schottky junction by choosing different types of metals and semiconductors. This simple approach, however, does not always give sufficiently correct results in practice. When a metal and a semiconductor are in contact with each other, the work function of the metal might be "pinned" to an energy level at the semiconductor junction (Fig. 2.2). The pinning level of the metal work function severely affects the Schottky barrier height and cannot be predicted by theoretical calculations [32]. Work function pinning can be avoided by using a very thin interlayer dielectric between the metal and the semiconductor [33]. The presence of such an interlayer dielectric layer has a significant effect on the electrical properties of the Schottky junction.

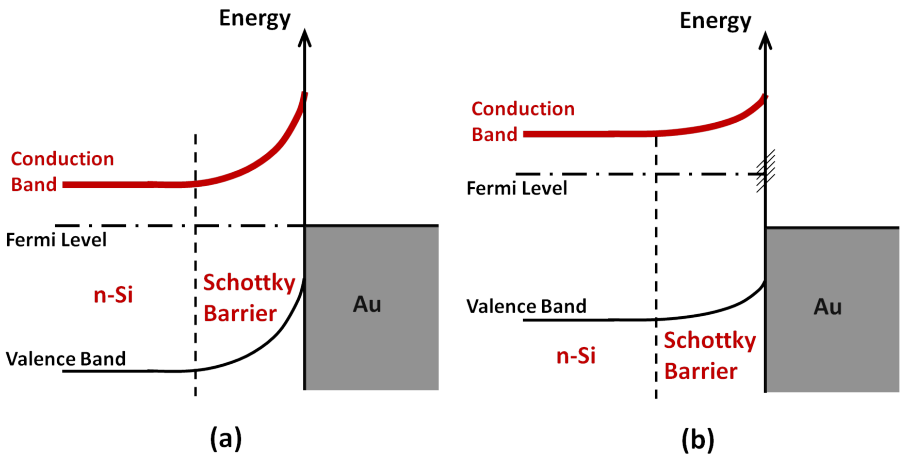

Figure 2.2: Energy band diagrams of Au/n-Si Schottky junctions without the work function pinning (a) and with work function pinning (b). The height of the Schottky barrier is directly affected by the pinning of the work function to another level. The shape of the Schottky barrier and other electrical properties are also affected by this change in the work function.

2.3 Metal-Insulator-Semiconductor (MIS) Junction

As well as changing the pinning of the work function, use of an interlayer dielectric will also directly affect the tunneling probability at the Schottky junction. The direct tunneling probability depends on the thickness of the interlayer dielectric and the height of the potential barrier introduced by the dielectric material [34]. At high bias voltages, the energy bands will be bent at the Schottky junction and the potential barrier introduced by the dielectric layer will get a triangular shape at sufficiently high electron energies. This triangular shape of the potential barrier actually implies a thinner potential barrier for the electrons with higher energies and the tunneling process through such a potential barrier is called Fowler-Nordheim tunneling. The electron reaches the conduction band of the insulator by tunneling part of the potential barrier. The direct tunneling and Fowler-Nordheim tunneling mechanisms are depicted in Fig. 2.3 [35].

Doping of the semiconductor does not affect the Schottky barrier height but

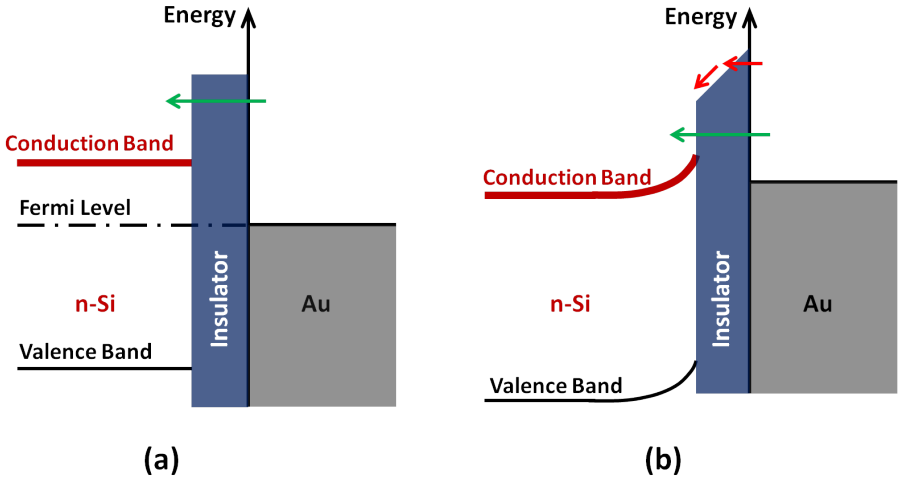

Figure 2.3: The energy band diagram of a metal-insulator-semiconductor (MIS) junction (a) at flat-band condition and (b) under reverse bias. In the direct tunneling process (green arrows) the tunneling probability depends on the thickness and the height of the potential barrier, and it is relatively independent of the bias voltage. For the electrons with sufficiently high energies, Fowler-Nordheim tunneling is observed (red arrow). The effective insulator thickness is reduced due to the bending of the energy bands with the high electric field. The tunneling probability depends on the electron energy and the bias voltage.

can greatly change the shape of the Schottky barrier. Effective thickness of the Schottky barrier changes due to the bending of the conduction and valence bands (Fig. 2.4). Tunneling probability of the hot electrons with energies smaller than the Schottky barrier is also affected by the change of the Schottky barrier shape. However, one must note that the tunneling current is almost negligible compared to the current generated by the internal photoemission over the Schottky barrier.

2.4 MIS Solar Cells

Schottky barrier diodes are also used in photovoltaic applications by making use of the built-in electric field to collect the photogenerated electron-hole pairs in the semiconductor. Usually an interlayer dielectric layer is used in order to avoid the work function pinning and to suppress the dark current. This section investigates the voltage development and dark current generation mechanisms at MIS solar

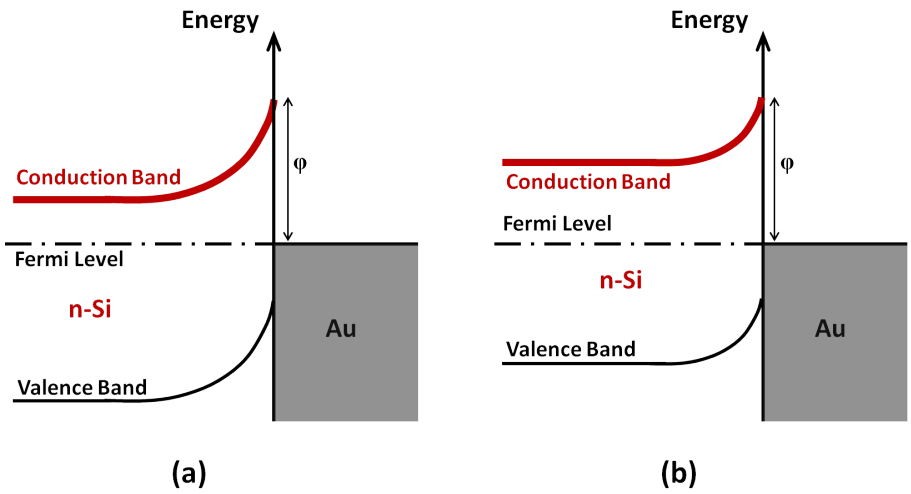

Figure 2.4: Energy band diagrams of two Schottky junctions with (a) highly doped and (b) lowly doped semiconductors. Band bending is greater for the highly doped semiconductor (a) compared to the lowly doped semiconductor (b) due to the position of the Fermi level. The triangular shape of the barrier gets thinner as the band bending increases, resulting in an increase in the tunneling probability of the hot electrons at these energy levels (Fowler-Nordheim tunneling).

cells to provide more insight into the electrical properties of Schottky junctions.

In general, the power conversion efficiency of a solar cell can be expressed as:

$$\eta = \frac{I_{sc} V_{oc} FF}{P_{in} a} \tag{2.2}$$

where I_{sc} is the short circuit current, V_{oc} is the open circuit voltage, FF is the fill factor, P_{in} is the incident solar power density and a is the surface area of the solar cell.

The open circuit voltage, V_{oc}, of metal-semiconductor junction solar cells suffers severe degradation due to high dark current and this seems to be the main bottleneck for the Schottky barrier solar cells. The total dark current density in a Schottky junction can be expressed as [36]:

$$J_D = J_{th} + J_{rg} + J_d + J_s \tag{2.3}$$

where the dark current components are [36]:

1. The thermionic emission dark current density, J_{th} caused by the thermionic

emission of charge carriers into the metal.

2. The recombination-generation current density, J_{rg} current due to the generation of electron-hole pairs in the depletion layer of the semiconductor. It should be noted that a depletion layer may not be present depending on the doping concentration of the semiconductor and the work function of the metal.

3. The injection-diffusion current density, J_d injection/diffusion of minority carriers into the semiconductor bulk.

4. The surface states current density, J_s current due to charge exchange via surface states between the metal and the semiconductor.

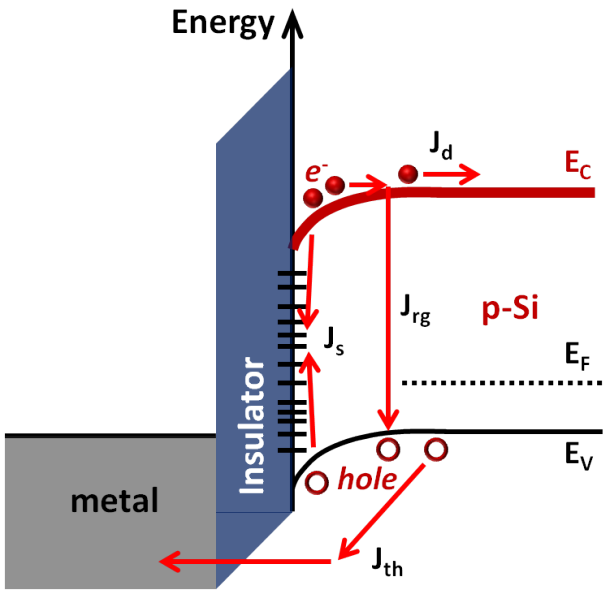

Figure 2.5: Dark current mechanisms in a Schottky junction are shown on the energy band diagram of a forward biased metal-insulator-semiconductor (MIS) solar cell. The thermionic emission dark current, J_{th}, recombination-generation current, J_{rg}, injection-diffusion current, J_d, and surface state current, J_s, are depicted on the energy band diagram. The thermionic emission dark current has been reported as the dominating dark current component for most practical cases.

Fig. 2.5 demonstrates these dark current components on the energy band diagram of an MIS junction with p-Si semiconductor, where the holes are the majority carriers [36]. Among these dark current components, the thermionic emission dark current is the dominant component for most cases. An expression for J_{th} can be written as [34]:

$$J_{th} = \Theta A^{**} T^2 \exp(-q\phi_b/kT) \exp(qV_j/nkT) \tag{2.4}$$

where Θ is the majority carrier tunneling coefficient, A^{**} is the Richardson's constant, q is the electron charge, ϕ_b is the barrier height at zero bias voltage, k is the Boltzmann constant, T is the temperature and n is the ideality factor. In traditional intimate contact metal-semiconductor Schottky barrier diodes ϕ_b is relatively small due to the pinning by the surface states at the interface and this results in very high J_{th} values that are not suitable for photovoltaic applications. By introducing a thin insulator layer at the interface, the semiconductor surface states can be passivated and ϕ_b will be dictated by the work function of the metal. This allows considerable reduction of the thermionic emission dark current by proper choice of metal type. Reducing the thermionic emission dark current by increasing the insulator thickness and reducing the majority carrier tunneling coefficient, Θ, is also possible. However, such an approach is likely to degrade the solar cell efficiency since the tunneling probability of photogenerated charge carriers will decrease as well [36].

Inevitably, there is a trade-off between the open circuit voltage and the short circuit current of the Schottky junction as the interlayer thickness changes, and this presents another parameter to optimize the Schottky junction [37].

In addition to an interlayer dielectric, several different metal layers can be used to obtain the desired optoelectronic properties at the Schottky junctions. Au is commonly preferred as the absorber layer for its optical properties and long mean free path of hot electrons in Au [10, 12, 30]. Commonly a thin adhesion layer such as Ti is deposited prior to Au evaporation. This layer improves the adhesion of Au to the underlying layer and helps the formation of a continuous Au layer [12]. The work function of the metal layer in contact with the semiconductor is mainly governed by this adhesion layer, resulting in Ti/Si Schottky barrier properties in

the electrical characterization instead of Au/Si Schottky barrier characteristics [12, 36]. Similarly, a barrier metal layer is used when there is need to control the Schottky barrier height by choosing a metal with desired work function. An additional metal layer (contact metal) with high conductivity can also be used on the barrier layer to get low resistance electrical contact to the metal layer of the Schottky junction.

2.5 Conclusion

Despite the challenges in optimizing the Schottky junction for specific optoelectronic applications, Schottky junctions have been successfully used in photodetection due to their simple fabrication, ease-of-integration to Si CMOS technology, repeatability and large area uniformity [38, 39]. The response times of Schottky barrier diodes are also typically much shorter than p-n junction diodes due to the lack of minority carrier storage effects. Response times as low as 10^{-10} seconds were reported in the earliest demonstrations of Schottky barrier infrared photodetectors [9]. Schottky diodes have also been used for photovoltaic applications to simply introduce a built-in electric field to Si and collect the photogenerated electron-hole pairs in Si. Up to $8\% - 10\%$ power conversion efficiencies have been reported with this approach [36, 40]. The main challenge, which has been investigated for over a decade, is the low optical absorption of metals for hot electron based photodetection and photovoltaic schemes. Use of surface plasmons to address this issue is explained in Chapter 3.

Chapter 3

Surface Plasmon Assisted Hot Electron Generation

3.1 Introduction

When a light wave is directed at the interface between a metal and a dielectric, the oscillations of the electrons at the surface of the metal may match the oscillations of the electromagnetic field if certain conditions are satisfied. The light wave resonantly interacts with the mobile electrons at the surface of the metal and this resonant interaction induces density waves of electrons which are called surface plasmons. The frequency of the surface plasmon wave is the same as the frequency of the incident light wave, but the wavelength of the surface plasmon is much shorter. Possible applications that could be enabled by this property of light, such as using nanoscale plasmonic interconnects to carry information in a processing unit, resulted in a continuously increasing interest in this field [41]. Use of surface plasmons to improve the efficiency of photodetectors, solar cells and light emitting diodes (LEDs) [42, 43, 44], or the medical applications that use the enhanced local electromagnetic field created by the surface plasmon resonances [45] were quickly demonstrated. With the advances in computational power and novel numerical methods scientist can now accurately simulate the complex electromagnetic fields

generated by plasmonic effects. Invention of novel methods for nanofabrication, imaging and characterization also greatly accelerated the development of this field of research.

In properly sized metallic nanoparticles, the free electrons of the metal can oscillate with the same frequency as the incident light and resonate with the optical wave. This resonance, which is called localized surface plasmon resonance (LSPR), may give rise to strong, highly localized electromagnetic fields. Propagating modes of surface plasmon polaritons (SPP) can also be triggered on metal dielectric interfaces with properly designed phase matching techniques (Fig. 3.1) [46]. SPPs are dispersive electromagnetic waves coupled to the electron plasma of the metal. LSPRs on the other hand are non-propagating and arise due the coupling of the electromagnetic wave to the conduction electrons of metal nanostructures [47].

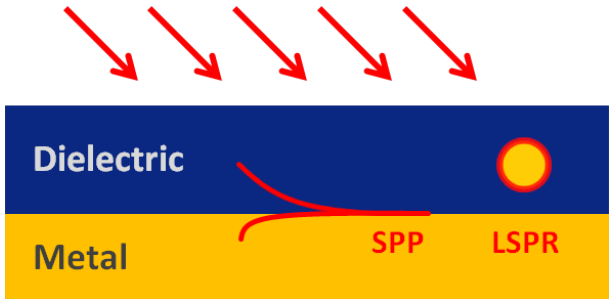

Figure 3.1: Propagating surface plasmon polaritons (SPP) and localized surface plasmon resonances (LSPR) at metal dielectric interfaces. SPPs can be excited by using a prism or with corrugations on the surface, and they propagate along the metal-dielectric interface. LSPRs are non-propagating and can be excited on metallic nanoparticles or metallic gratings even under direct illumination.

Integration of plasmonic resonance schemes with conventional photodetectors and photovoltaic devices by making use of the optical trapping and field concentrating properties of surface plasmons has been studied extensively [43]. Typically, such nanostructures are used as optical nanoantennas by placing them on or very close to the active region of an optical device. Even more interestingly, recent studies have also showed that such metallic nanoparticles and nanostructures can be used to directly convert the energy of electromagnetic waves to electrical energy by generating hot electrons in the metal by the decay of surface plasmons

[1, 23].

3.2 Localized Surface Plasmon Resonances

The interaction of an electromagnetic field with a sub-wavelength nanoparticle of size d, can be solved with quasi-static approximation provided that the size of the nanoparticle is much smaller than the wavelength of the electromagnetic field ($d \ll \lambda$). In quasi-static approximation the phase of the electromagnetic field is assumed to be constant over the particle volume. The problem is simplified to a particle in static electric field, and the harmonic time dependence can be added once the field distributions are solved for the static case. This approach has been used to model the optical properties of metals accurately for nanoparticle dimensions less than 100 nm [47].

Solving the Laplace equation for the potential, $\nabla^2\Phi = 0$, for a nanoparticle in static electric field, $\mathbf{E_0} = E_0\hat{z}$, we can calculate the resulting electric field distribution $\mathbf{E} = -\nabla\Phi$. For the simple case of a spherical nanoparticle with the dielectric function $\varepsilon(\omega)$ and radius a, and a non-absorbing and isotropic surrounding medium with the dielectric constant ε_m, the potential distribution can be solved as:

$$\Phi_{in}(r,\theta) = \sum_{l=0}^{\infty} A_l r^l P_l \cos(\theta) \tag{3.1}$$

$$\Phi_{out}(r,\theta) = \sum_{l=0}^{\infty} [B_l r^l + C_l r^{-(l+1)}] P_l \cos(\theta) \tag{3.2}$$

where $\Phi_{in}(r,\theta)$ and $\Phi_{out}(r,\theta)$ are the electric potential distribution inside and outside the spherical nanoparticle, respectively. $P_l(\cos\theta)$ are the Legendre Polynomials of order l, and θ is the angle between the position vector $\mathbf{r}$ and the z-axis. The coefficients A_l, B_l and C_l can be found by imposing the boundary conditions at $r = a$ and $r \to \infty$. The potentials can then be written as [47]:

$$\Phi_{in} = -\frac{3\varepsilon_m}{\varepsilon(\omega) + 2\varepsilon_m} E_0 r \cos\theta \tag{3.3}$$

$$\Phi_{out} = -E_0 r\cos\theta + \frac{\varepsilon(\omega) - \varepsilon_m}{\varepsilon(\omega) + 2\varepsilon_m} E_0 a^3 \frac{\cos\theta}{r^2} \tag{3.4}$$

A very fundamental result of Eq. 3.4 is the interpretation of this potential as the superposition of the applied field and the field of a dipole located at the center of the nanoparticle. Basically, in addition to the potential due to the applied electric field, another potential arises since the applied field creates a dipole at the nano-sphere. Rewriting the potential Φ_{out} we can get an expression for the dipole moment $\mathbf{p}$.

$$\Phi_{out} = -E_0 r\cos\theta + \frac{\mathbf{p}\cdot\mathbf{r}}{4\pi\varepsilon_0\varepsilon_m r^3} \tag{3.5}$$

$$\mathbf{p} = 4\pi\varepsilon_0\varepsilon_m a^3 \frac{\varepsilon(\omega)-\varepsilon_m}{\varepsilon(\omega)+2\varepsilon_m}\mathbf{E_0} \tag{3.6}$$

We can then define polarizability function, α, by using the equation $\mathbf{p} = \varepsilon_m\varepsilon_0\alpha\mathbf{E_0}$.

$$\alpha = 4\pi a^3 \frac{\varepsilon(\omega)-\varepsilon_m}{\varepsilon(\omega)+2\varepsilon_m} \tag{3.7}$$

polarizability function α has a complex value and is a measure of how strongly a dipole can be created at the nano-sphere under quasi-static approximation. The denominator of the polarizability function α gives the Fröhlich condition $\mathrm{Re}[\varepsilon(\omega)] = -2\varepsilon_m$, which gives a resonant enhancement. This condition holds when the imaginary part of the dielectric function of the nano-sphere, $\mathrm{Im}[\varepsilon(\omega)]$, is small or a slowly varying function of frequency. This resonance condition also implies that the maximum value of the polarizability function α is mainly limited by the imaginary part of the dielectric function of the nano-sphere, $\mathrm{Im}[\varepsilon(\omega)]$, which corresponds to the optical losses in metals [47].

Calculating the electric field distribution inside and outside the nano-sphere, we observe that resonant enhancement occurs for both fields. Electric fields both inside the nanoparticle and in close vicinity of the nanoparticle are enhanced by the localized surface plasmon resonances. More commonly, resonant enhancement of $\mathbf{E_{out}}$ is exploited in photodetectors, biological and chemical sensors [48], and surface enhanced Raman scattering (SERS) [49] to obtain highly confined electric fields in the near field of a nano-sphere. On the other hand, if the nanoparticles were to be used as hot electron generation spots in a surface plasmon assisted hot electron device, the field inside the nanoparticle would gain more importance.

$$\mathbf{E_{in}} = \frac{3\varepsilon_m}{\varepsilon(\omega)+2\varepsilon_m}\mathbf{E_0} \tag{3.8}$$

$$\mathbf{E_{out}} = \mathbf{E_0} + \frac{3\mathbf{n}(\mathbf{n}\cdot\mathbf{p}) - \mathbf{p}}{4\pi\varepsilon_0\varepsilon_m}\frac{1}{r^3} \tag{3.9}$$

Having obtained the field distribution for the electrostatic case, we can calculate the electromagnetic field radiated by the nano-sphere upon illumination with a plane wave, $\mathbf{E}(\mathbf{r},t) = \mathbf{E_0}e^{-i\omega t}$, by introducing a harmonic time dependence to the dipole moment calculated by the quasi-static approach.

$$\mathbf{p} = \varepsilon_m\varepsilon_0\alpha\mathbf{E_0}e^{-i\omega t} \tag{3.10}$$

where α is the same polarizability function that is calculated for the electrostatic case. The radiation of this dipole represents the scattering of the plane wave by the nano-sphere and can be investigated as the radiation of a point dipole. The scattering cross section, C_{sca}, and the absorption cross section, C_{abs}, can be written as follows [50]:

$$C_{sca} = \frac{k^4}{6\pi}|\alpha|^2 = \frac{8\pi}{3}k^4a^6|\frac{\varepsilon(\omega)-\varepsilon_m}{\varepsilon(\omega)+2\varepsilon_m}|^2 \tag{3.11}$$

$$C_{abs} = k\mathrm{Im}[\alpha] = 4\pi ka^3 Im[\frac{\varepsilon(\omega)-\varepsilon_m}{\varepsilon(\omega)+2\varepsilon_m}] \tag{3.12}$$

These cross sections correspond to the efficiency of the metal particle for scattering and absorption of light. It is also important to note that for nanoparticles much smaller than the wavelength, the efficiency of absorption scales with a^3 and dominates over the efficiency of scattering which scales with a^6 [47].

This approach to calculate the polarizability of a nano-sphere under quasi-static assumption can be extended to ellipsoid nanoparticles and the effect of their extended shape on the polarizability can be investigated. It has been shown that the resonance on the longer axis of such structures exhibit a significant red-shift compared to a nano-sphere of the same volume [47]. For particles with larger dimensions, an electrodynamic approach is required since the phase of the incident field changes considerably over the volume of the particle. This approach is now known as the Mie theory and can completely describe the scattering and absorption of electromagnetic radiation by a sphere [47, 51].

The formulation of the polarizability of nanoparticles with spherical or ellipsoid shapes also leads us to decay mechanisms of surface plasmons. Two main decay

mechanisms are non-radiative decay and radiative decay. There is a direct path for the coherent electron oscillations of metal to decay by radiating photons. The radiative damping results in a broadening of the plasmon resonance as the particle size increases. This effect is more pronounced for larger nanoparticles, and increases with the particle size [47].

Non-radiative decay, namely absorption, occurs by the excitation of the conduction band electrons or the d-band electrons of the metal to higher energy levels. The probability of the non-radiative decay of surface plasmons increases with decreasing particle size [1, 47]. The non-radiative decay constitutes the fundamental mechanism for plasmon assisted hot electron generation.

3.3 Plasmon Assisted Hot Electron Generation

When an optical beam excites surface plasmons on a nanostructure, the decay of the electromagnetic wave takes place in timescale of several femtoseconds either radiatively or non-radiatively. Radiative process results in the emission of photons with the same frequency as the incident light [52], and the non-radiative process results in the transfer of the surface plasmon energy to the electrons of the metal [53, 54, 55]. Electrons are generally excited from the conduction band to higher energy states in the same band (intraband excitation process). The excitation can also take place between the conduction band and other bands (d bands) in an interband excitation process, but the energy levels of d bands are substantially (2.4 eV - 4 eV) lower than the conduction band energy level for metals such as Au and Ag, making the interband excitation far less likely than intraband excitation [56, 57]. The distribution of the hot electrons can be basically described by a Fermi function with a higher effective temperature [1]. Excited hot electrons can travel over the Schottky barrier to the semiconductor if they have enough energy. The hot electrons without sufficient energy lose their excess energy with electron-electron or electron-phonon collisions, and the excess energy is eventually converted into heat [58]. White and Catchpole make a theoretical

analysis on photovoltaic action through plasmon enhanced internal photoemission mechanism. Assuming perfect absorption in the metal layer, the upper limit of efficiency of such a photovoltaic device is calculated to be 8% due to the fundamental electronic properties of metallic absorbers [56]. This limit arises from the broad distribution of possible hot electron energies and could be theoretically increased to above 20% if the electron density of states of the metallic absorber could be modified [56]. This analysis, however, neglects the momentum requirement imposed on the hot electrons. Normal component of the momentum of an electron should be higher than $\rho_{crit} = [2m^*(E_F + \varphi)]^{1/2}$ to overcome the potential barrier, where m* is the effective mass of electron, E_F is the Fermi energy and φ is the Schottky barrier height. This condition defines an acceptance cone of angles for the electrons approaching the interface that can be allowed to cross the potential barrier (Fig. 3.2) [56, 59]. With this condition, Leenheer *et al.* calculates the maximum efficiency of solar energy conversion via hot electron internal photoemission to be less than a mere 1% [59]. The hot electrons that do not have sufficient momentum normal to the interface will be reflected back from the junction to the metal absorber. If the metallic absorber is sufficiently thin and the hot electron attenuation length in the metal is sufficiently long, then the electrons traveling at various angles can eventually reach the metal-semiconductor interface with suitable momentum after multiple reflections in the metal. In this case, the electron emission probability will approach unity and almost all hot electrons with energies greater than the Schottky barrier height will be emitted to the semiconductor [56].

Injection of hot electrons to a semiconductor leaves the plasmonic nanostructure positively charged because of the lost electrons. These lost electrons need to be replenished back to the plasmonic nanostructure in order for the plasmon assisted hot electron emission to the semiconductor to continue. A donor solution or a hole transporting material (HTM) is required to compensate the lost electrons and complete the electrical circuit. In order to investigate the timescales of hot electron generation, injection and regeneration processes, Furube and Du [60, 61] have used ultrafast visible-pump/infrared-probe femtosecond transient

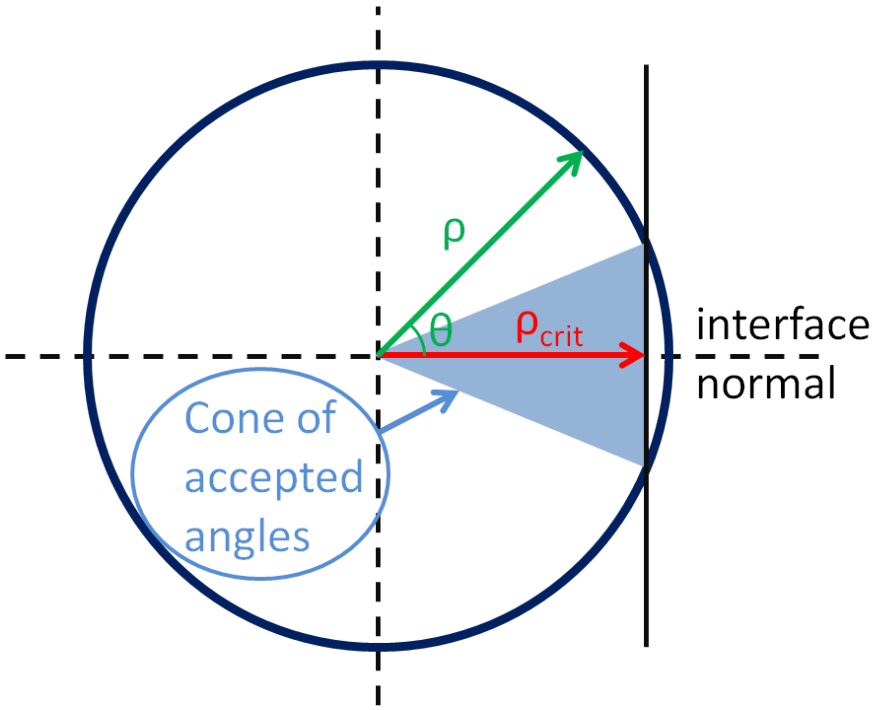

Figure 3.2: Possible momentum values of hot electrons form a sphere in the momentum space. The momentum of a hot electron should be such that its component normal to the metal-semiconductor interface should be larger than a critical value, ρ_{crit}, which is defined by the Schottky barrier height. This condition defines a cone of angles in the momentum space for which the hot electrons will be allowed to be emitted from the metal to the semiconductor.

absorption spectroscopy. This technique relies on the increased visible absorption of TiO_2 when there are free carriers at its conduction band. The visible pump laser excites localized surface plasmon resonances on the Au nanoparticles deposited on TiO_2 semiconductor layer and generates hot electrons through surface plasmon decay. These hot electrons are then injected to the conduction band of TiO_2 and increase its infrared absorption. The infrared-probe laser monitors the increased transient absorption of the TiO_2 semiconductor. Researchers have found that hot electron generation via the decay of surface plasmons and injection of the hot electrons from the metal are completed within 50 fs. When a hot electron is injected from the Au nanoparticle, it decays back to the nanoparticle in a few nanoseconds unless the lost charge of the nanoparticle is replenished by another source. Typically, a donor solution is required to replenish the lost electrons to the Au nanoparticle. Donors such as $[Fe(CN)_6]^{4-}$, Fe^{2+}, $C_{10}H_{10}Fe$,

and $C_{10}H_9FeCOOH$ give sub-millisecond regeneration times [62]. A study that uses a polyethylene oxide donor solution filled with TiO_2 nanoparticles containing optimized redox couples of I^-/I^{3-} achieves less than 20 ns regeneration times [62]. Even with these improvements in the electron regeneration time, it is still much slower than the hot electron generation and injection processes and presents a significant bottleneck for the hot electron based photovoltaic devices.

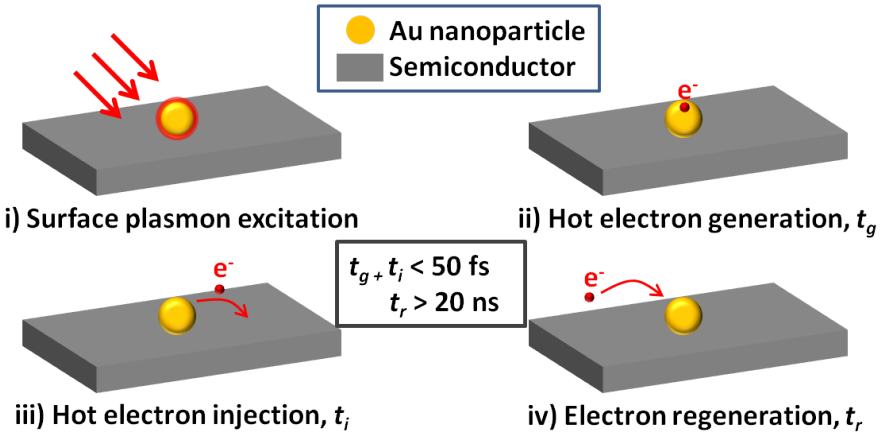

Figure 3.3: (i) Incident light excites surface plasmons on Au nanoparticles. (ii) Surface plasmons decay by giving their energy to the electrons of the metal, generating hot electrons. (iii) Hot electrons are injected from the metal to the semiconductor. Hot electron generation and injection processes are completed within 50 fs. (iv) An electron must be replenished to the metal instead of the injected one so that the hot electron generation and injection from the metal nanoparticle can continue. The fastest reported timescales of charge regeneration process are in the order of 20 ns.

Undoubtedly, a distinguishing property of surface plasmons is the dependency of the resonance to the polarization of the incident light. This effect is more pronounced for the excitation of SPPs since only the transverse magnetic (TM) polarized light can excite such resonances on metal dielectric interfaces and metallic gratings. The excitation of LSPR on spherical nanoparticles does not show such polarization dependency due to the spherical symmetry but similar wavelength dependency will occur when elliptical nanoparticles or nanorods are used to excite LSPR [12]. This polarization dependency serves as a simple way to obtain polarization selective photodetectors but it is generally avoided for photovoltaic applications. Tuning the wavelength of the plasmonic resonances is also

possible and used as a powerful tool for photodetectors. Wavelength of the SPP resonances can easily be tuned by changing the geometry of the metallic gratings, and similarly wavelength of the LSPR can be tuned by changing the size or the geometry of metallic nanoparticles. With the ability to obtain easily tunable, strong and narrow-band plasmonic resonances the fabrication of wavelength selective photodetectors become possible [12, 13].

In our experiments, we have mostly exploited LSPR to generate hot electrons. Chemically synthesized Au nanoparticles or randomly formed Au nanoislands with thermal annealing were used to excite LSPR. Random distribution and random size of these nanostructures give broad-band resonances. Such resonances are especially preferred for photovoltaic applications and broad-band photodetection applications. Our work on the application of surface plasmon assisted hot electron generation process to photodetectors and photovoltaic devices is presented in the subsequent chapters.

Chapter 4

Plasmonic nanoantennas for sub-bandgap photodetection

This chapter is based in part on the publication "Random sized plasmonic nanoantennas on Silicon for low-cost broad-band near-infrared photodetection," M.A. Nazirzadeh, F.B. Atar, B.B. Turgut and A.K. Okyay, *Scientific reports*, vol. 4, 2014. Reproduced (or "Reproduced in part") with permission from Nature Publishing Group. Copyright 2014 Nature Publishing Group

4.1 Introduction

Near infrared (NIR) photodetectors monolithically integrated on Si substrates stand as an attractive alternative to conventional NIR photodetection schemes. Well established Si nanofabrication technology seems to be a good candidate for low-cost manufacturing of NIR photodetectors with good repeatability and high quality [38, 39]. First demonstrations of NIR photodetection on Si substrates dates back to 1960s where a metal in contact with Si was used to absorb low energy photons and generate photocurrent by the internal photoemission mechanism [9]. In a recent study, Knight *et al.* used Au nanorod structures on Si surface to

act as optical antennas by exciting surface plasmon resonances and generate hot electrons by the decay of surface plasmons [12]. The nanorods were patterned with electron beam lithography technique, which allowed precise control of the size, shape and distribution of the nanorods. In this work, we use randomly distributed Au nanoparticles forming Schottky junctions with the semiconductor substrate for the excitation of LSPR and generation of hot electrons [14, 63].

4.2 Device Architecture

The device structure of the NIR photodetectors investigated in this study is shown in Fig. 4.1 together with the configuration for optoelectronic characterization. Si substrates with n-type doping are used for the fabrication of our devices. Au nanoparticles on Si surface are used to excite localized surface plasmon resonances (LSPR) upon illumination with NIR light [14, 63]. Non-radiative decay of LSPRs on the Au nanoparticles results in the generation of hot electrons. These highly energetic electrons are collected over the Schottky barrier to the semiconductor by the internal photoemission process. This process results in the generation of photocurrent and the detection of sub-bandgap NIR photons.

In this device architecture, the Si substrate is used as the bottom contact, and a transparent conductive oxide (TCO) layer coated on the metal nanoparticles form the top contact. Au nanoislands on Silicon substrate form an Au-Si Schottky junction, whereas the Aluminum-doped Zinc Oxide (AZO) layer forms a heterojunction with Si substrate [64]. AZO layer also creates electrical contact between the Au nanoislands. We investigate two different methods to obtain Au nanoparticles on Si surface. In the first method Au nanoparticles are chemically synthesized and spin coated on samples. The second method uses rapid thermal annealing of a thin Au film deposited on Si surface to create random nanoparticles.

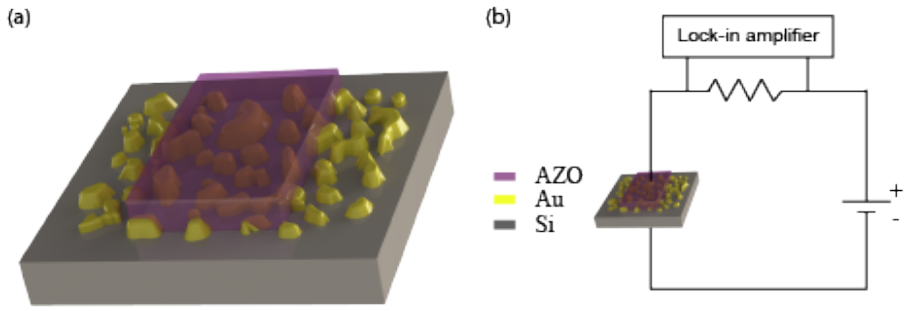

Figure 4.1: (a) The schematic view of the hot electron based near infrared photodetector structure. n-type Si is used as substrate. Au nanoparticles on Si surface excite LSPR and generate hot electrons. An Aluminum-doped Zinc Oxide (AZO) layer forms the top contact. (b) Configuration for the optoelectronic characterization. Voltage across a resistor in series with the photodetector is used to measure the photocurrent. Biasing polarity of the device is shown on the figure.

4.3 Chemical Synthesis of Au Nanoparticles

Au nanoparticles are synthesized by a slightly modified Turkevich method [65]. Sodium tris-citrate at desired Au/citrate ratio was used as the reducing agent. Under vigorous stirring pre-heated citrate was added to the boiling gold solution [25, 65]. This process allows us to obtain Au nanoparticles with approximately 50 nm diameter (the synthesis was carried out by a co-worker). We measured the visible absorption spectrum of the Au nanoparticles in de-ionized water solution (Fig. 4.2). Nanoparticles in water solution show resonant absorption centered at 530 nm wavelength. Finally the nanoparticles are spin-coated on the substrates at 1000 rpm rotational speed.

Spin-coating of chemically synthesized Au nanoparticles on SiO_2 and Al_2O_3 surfaces yields relatively good results with insignificant agglomeration of nanoparticles and quite good homogeneity, however spin-coating on Si substrates give poor homogeneity and the nanoparticles agglomerate into clusters. Residual chemicals left from the synthesis process are also thought to contaminate the Schottky junction, which is very critical for Schottky barrier diodes.

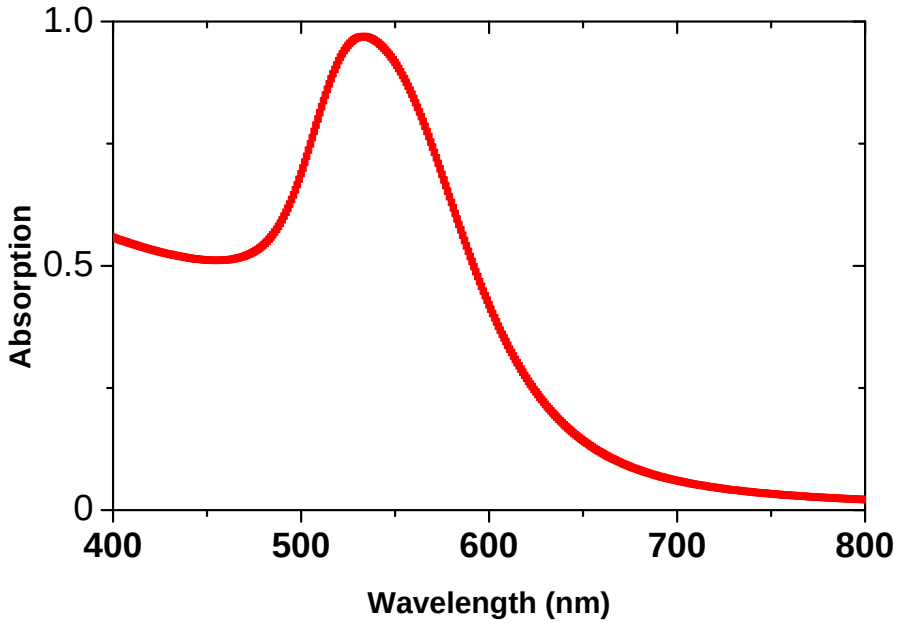

Figure 4.2: Absorption spectrum of the Au nanoparticles synthesized by the modified Turkevich method. The absorption spectrum is measured with the Au nanoparticles in de-ionized water solution. Au nanoparticles exhibit absorption resonance at around 530 nm wavelength. Copyright 2013 Optical Society of America

4.4 Random Au Nanoparticles with Thermal Annealing Method

As an alternative way to obtain nanoparticles, we use a method similar to [66]. We perform a rapid thermal annealing (RTA) process to turn a thin Au layer into nanoislands or nanoparticles by the agglomeration of the Au layer. Gatan Inc. Precision Etching Coating System (PECS) is used to deposit 10 nm Au layer on Si substrates. The samples are annealed under nitrogen gas flow for 1 minute in a rapid thermal annealing (RTA) system. This process results in randomly distributed and randomly sized Au nanoislands on Si surface. Scanning electron microscope (SEM) images of chemically synthesized Au nanoparticles spin coated on quartz substrate and Au nanoislands formed with rapid thermal annealing process are shown in Fig. 4.3 for comparison [14].

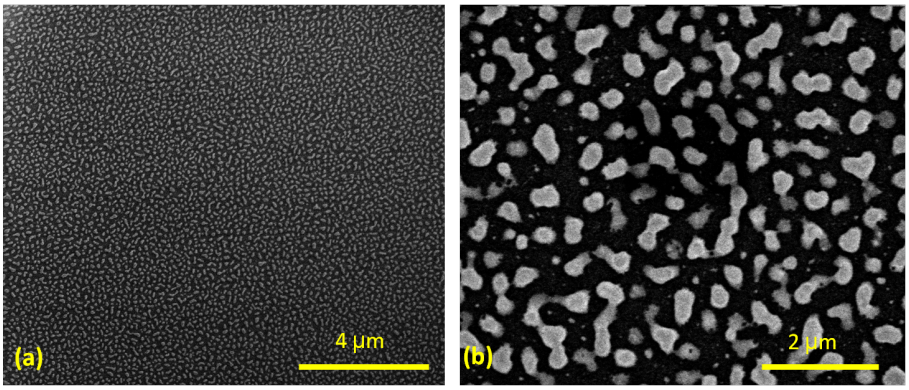

Figure 4.3: (a) SEM image of chemically synthesized Au nanoparticles coated on quartz substrate. Dense and uniform nanoparticle distribution could be achieved on quartz substrates. (b) SEM image of Au nanoislands formed with rapid thermal annealing of a thin Au layer on Si substrate. Instead of identical nanoparticles, elongated nanoislands with random shapes are obtained. The size distribution of the nanoislands is much broader than that obtained with chemical synthesis.

We experiment with different annealing temperatures to observe the effect of temperature on the size, shape and distribution of Au nanoislands. When annealed at 300°C, the Au layer forms into a semi-continuous film. When annealed at higher temperatures (450°C and 600°C), randomly sized and randomly distributed Au nanoislands are obtained. Annealing at 600°C results in smaller nanoislands compared to the ones obtained by annealing at 450°C (Fig. 4.4). ImageJ software is used to obtain the size distribution histograms of the nanoislands from the SEM images taken from the surfaces of samples. The histograms also verify the decrease in nanoparticle sizes as the annealing temperature increases (Fig. 4.5) [14].

4.5 Device Fabrication

For the fabrication of the photodetectors, (100) n-Si wafers with 2-5 Ω-cm resistivity are used as substrates. Samples are cleaned in H_2SO_4:H_2O_2 (4:1) solution (piranha solution) for 5 minutes to remove organic and metal contaminants from the samples. This cleaning results in a thin oxide layer on the Si surface. The

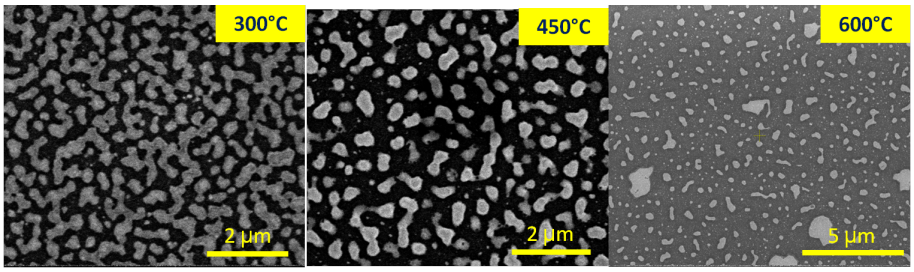

Figure 4.4: SEM images of the samples annealed at 300°C, 450°C, and 600°C. The Au layer forms into a semi-continuous Au film when the annealing temperature is 300°C. Increasing the annealing temperature results in the separation of connected Au nanoislands to form smaller nanoislands or nanoparticles.

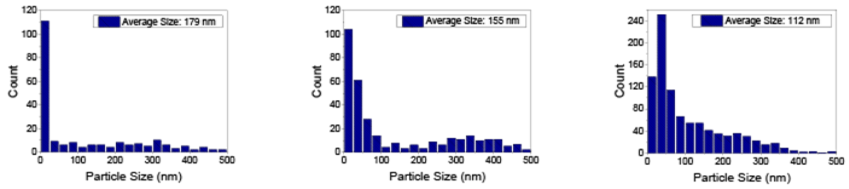

Figure 4.5: Particle size distribution histograms of SEM images in Fig. 4.4. The histograms belong to samples annealed at 300°C, 450°C and 600°C in order from left to right. The average nanoparticle sizes extracted from SEM images are 179 nm, 155 nm and 112 nm for samples annealed at 300°C, 450°C and 600°C, respectively. The number of smaller particles is greater for the samples annealed at higher temperatures.

samples are rinsed with de-ionized water after the piranha cleaning, dipped in buffered hydrofluoric acid (BHF) solution to clean the resulting surface oxide and finally rinsed again with de-ionized water solution. Au nanoparticles are formed on the Si surface by rapid thermal annealing of a thin Au layer. 50 nm-thick Aluminum-doped Zinc Oxide (AZO) is deposited on the samples using an atomic layer deposition (ALD) system (Cambridge Nanotech Inc., Savannah S100). The deposition is performed at 250°C with trimethylaluminum (TMA), diethylzinc (DEZn) and milli-Q water (H_2O) precursors. The AZO is obtained by the deposition of ZnO and Al_2O_3 layers with 28:1 ratio. Alternating cycles of DEZn:H_2O and TMA:H_2O are used for the deposition of ZnO and Al_2O_3 layers, respectively. Active device regions with 300 μm×600 μm dimensions are patterned with photolithography and etched by dipping in HNO_3 solution for 8 seconds. Solvent cleaning with acetone, isopropyl alcohol and de-ionized water

was performed prior to optical and electrical measurements.

We investigate samples annealed at different temperatures, which have different Au nanoisland sizes and shapes. Two types of additional devices are considered as references (Fig. 4.6). The first reference, "AZO reference," only has the AZO capping layer on Si, and does not have any Au layer or Au nanoparticles. Since the Si substrate and the AZO layer do not absorb NIR light, this reference would not show photoresponsivity at NIR wavelengths. The second reference, "Au reference," only has a thin continuous Au layer on Si. Since there are no nanoparticles on Si substrate, the surface plasmons are not excited on the continuous metal film under direct illumination (neglecting surface roughness of the Au film). Without the excitation of surface plasmons, the incident NIR light can couple very weakly to the metal layer. As a result, the NIR photoresponsivity of "Au reference" would be significantly lower than the devices with Au nanoislands [14].

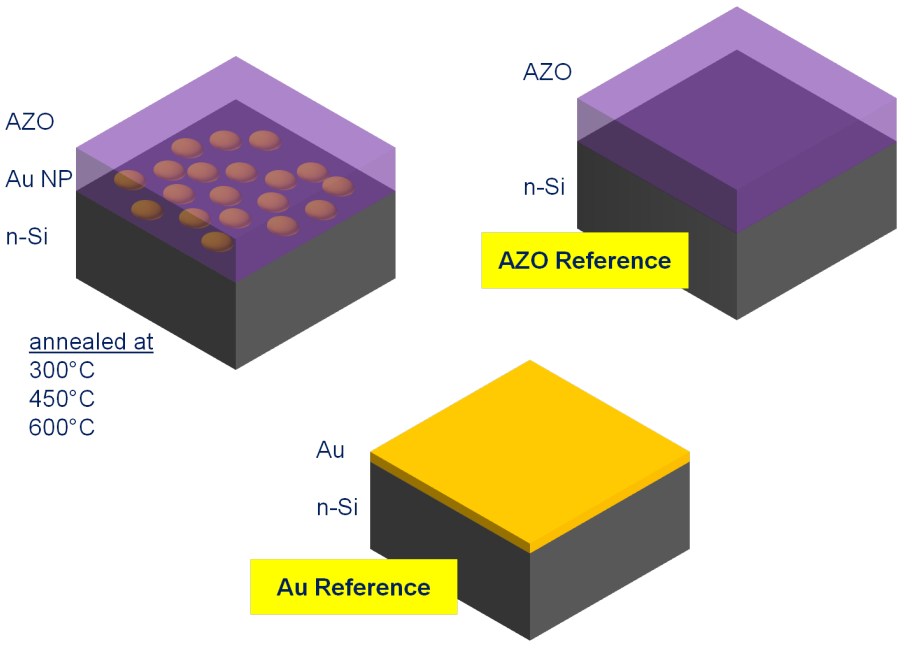

Figure 4.6: Devices with different Au nanoparticle size and distribution are obtained by rapid thermal annealing of the samples at different temperatures: 300°C, 450°C and 600°C. "AZO Reference" only has an AZO layer coated on Si substrate without Au nanoislands and "Au Reference" only has a flat Au layer on Si substrate without the AZO layer.

4.6 Optoelectronic Characterization

The dark current-voltage (I-V) characteristics of the devices are measured using Keithley 2401 Sourcemeter. A custom made LabView program is used for automated voltage sweep measurements. For photoresponsivity measurements, we use a laser light from a super continuum laser source (Fianium) and filter the laser light by an acousto-optic transmission filter (AOTF - Crystal Tech.) to get monochromatic laser beam. We use a custom designed optical setup to align the laser beam and focus the beam on the devices with normal incidence (Fig. 4.7 and Fig. 4.8). Laser light is mechanically chopped at 970 Hz (arbitrarily chosen) and the chopper frequency is fed as the reference signal to a lock-in amplifier (SRS830, Stanford Research Systems). We used a resistor in series with the photodetector and applied a DC voltage with Keithley 2401 sourcemeter to reverse bias the photodetectors. We determine the resulting photocurrent by measuring the voltage on the resistor with the lock-in amplifier.

The dark current vs. voltage (I-V) measurement results are plotted in Fig. 4.9. The AZO reference device exhibits decent rectification and low dark current density (0.5 pA/μm^2). The other devices which have Au nanoislands at the Silicon-AZO interface have significantly higher dark current and poor rectification property. We believe this increase in the dark current and reduced rectification contrast are mainly due to the increased number of generation/recombination centers near the Silicon-AZO interface [14, 67]. Presence of Au nanoislands and the diffusion of Au into Silicon and AZO layers during the atomic layer deposition process introduce deep-level traps, which act as generation-recombination centers around the interface. Under reverse bias condition the generated charge carriers are quickly swept away from this region to the contacts before recombination can occur. This results in high reverse bias current and degrades the rectification property of the diode.

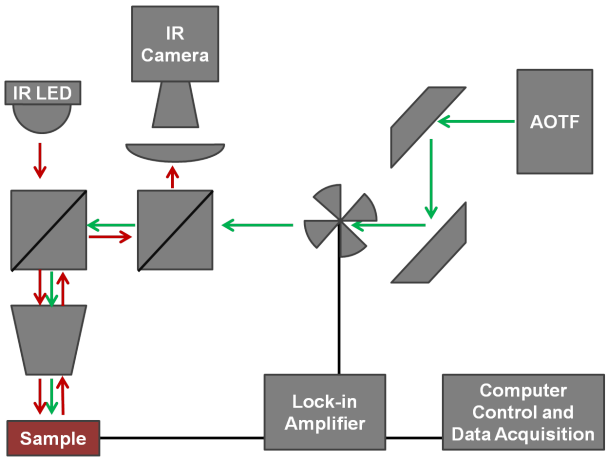

Figure 4.7: Schematic drawing of the photoresponsivity measurement setup. A super continuum laser light is monochromated with an acousto-optic transmission filter (AOTF) and used as a monochromated light source. Laser beam is aligned with mirrors and focused on the device with an objective lens. Two beam splitters in the beam path are used to simultaneously illuminate the device with laser light and infrared LED light, and also to image the device surface with an IR camera for probing. The green arrows in the image show the path of the laser beam and the red arrows show the path of the IR illuminating beam that is imaged by the IR camera.

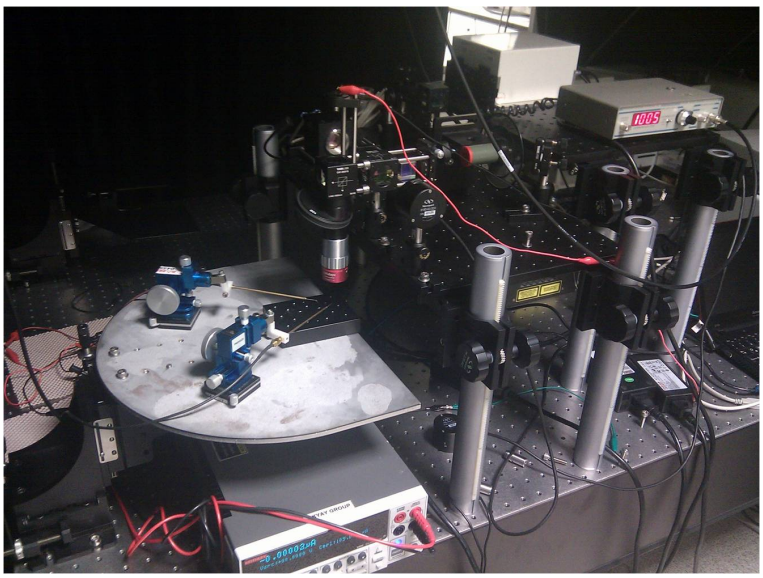

Figure 4.8: A photograph of the photoresponsivity measurement setup. The acousto-optic transmission filter (AOTF), the custom designed optic setup and the probing system are shown in the image.

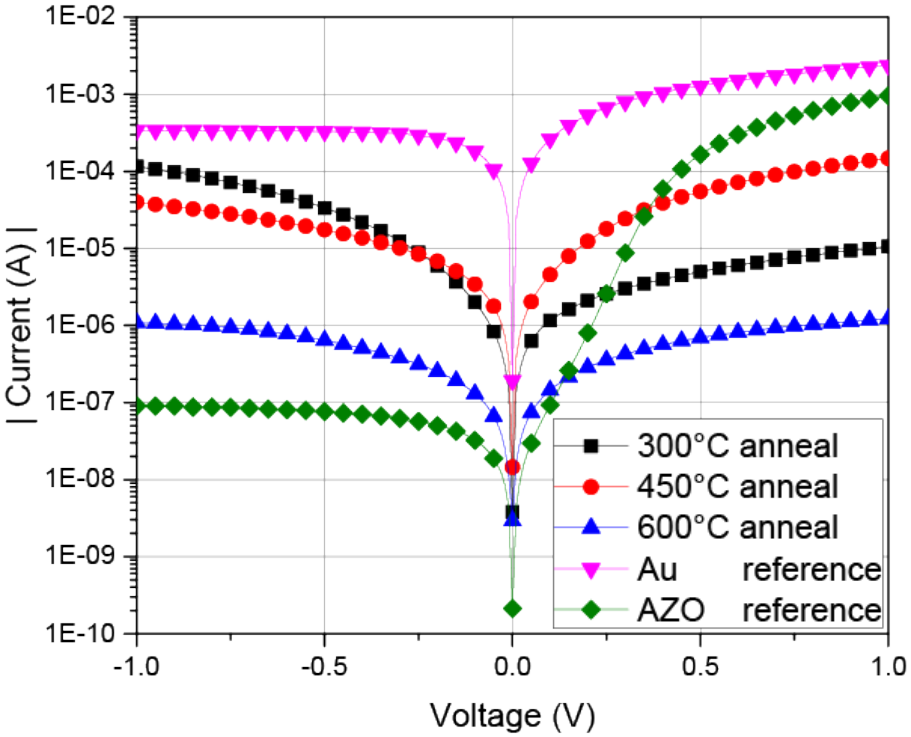

Figure 4.9: Dark current-bias voltage (I-V) measurement results of the fabricated photodetectors. AZO Reference exhibits low dark current and good rectification. The other samples which have Au nanoislands and Au Reference have higher dark current due to the generation-recombination centers at the interface.

Measured photoresponsivity spectra of the devices with Au nanoislands and the reference devices are plotted in Fig. 4.10. The AZO reference can detect photons with energies larger than the bandgap energy of Si ($\lambda < 1200$ nm). When Au nanoislands or flat Au layer are present at the junction, sub-bandgap photons can generate photocurrent by the internal photoemission process. Compared to the Au Reference, which has flat Au layer, the devices with Au nanoislands can show significantly higher photoresponsivity. The enhanced photoresponsivity can be explained by the excitation of localized surface plasmons and plasmon assisted generation of hot carriers at the randomly shaped Au nanoislands [68]. The device annealed at 450°C has 2 mA/W photoresponse at 1300 nm, and exhibits the highest photoresponsivity for the wavelengths shorter than 1500 nm. At longer wavelengths ($\lambda > 1500$ nm), the device annealed at 300°C has the highest photoresponse. This could be explained by the red-shift in plasmon resonances due to the elongation of the Au nanoislands with decreased annealing temperature [14].

In a hot electron based photodetection scheme, there are mainly three consecutive mechanisms:

1. Generation of hot electrons by the absorption of incident light or the decay of surface plasmons into hot electrons.
2. Collection of the generated hot electrons to the semiconductor.
3. Regeneration of the lost electrons back to the metal nanoparticles.

The nanoparticles are directly in contact with the conducting AZO layer so there is a path for the regeneration of the lost electrons. However, time scale of this regeneration process is not investigated in this study and stands as a degrading factor for the photoresponsivity (as explained in Chapter 3). The photoresponsivity spectra of the hot electron based photodetectors are then estimated by the product of the two remaining mechanisms (product of hot electron generation rate and hot electron collection efficiency). The hot electron collection efficiency can be represented by the Fowler function [12, 29], and the absorption spectra of

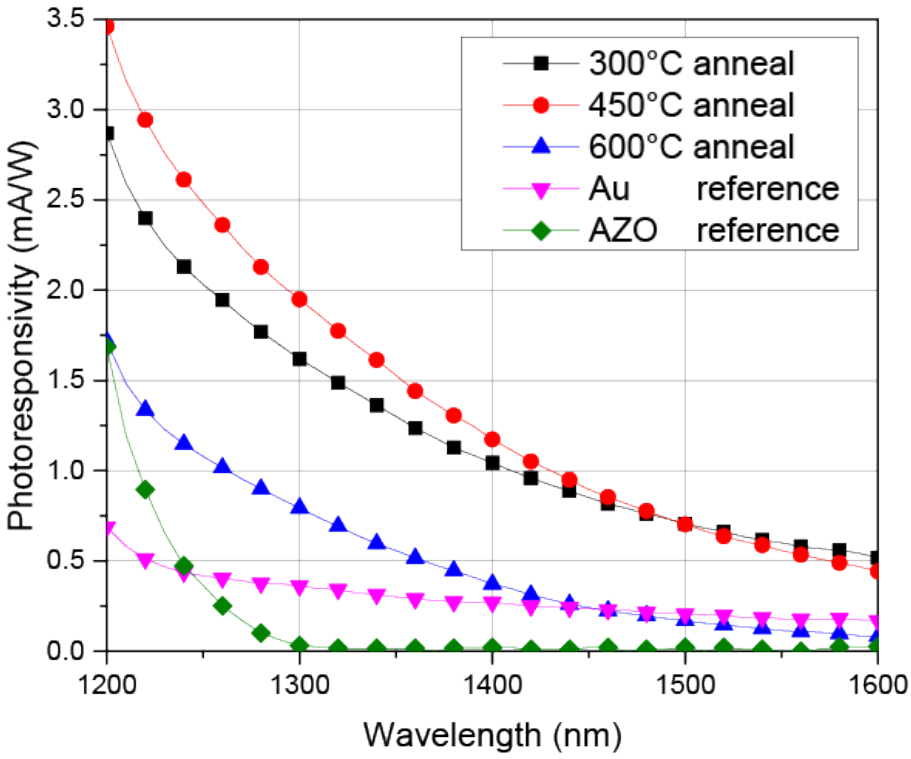

Figure 4.10: Measured photoresponsivity spectra of the fabricated photodetectors. The photoresponse of the AZO Reference drops sharply for $\lambda > 1200$ nm. The Au Reference can exhibit photoresponse at these wavelengths with the internal photoemission process. Due to the excitation of surface plasmons, the devices with Au nanoislands have significantly higher photoresponse compared to the Au Reference. The device annealed at 450°C shows the highest photoresponsivity for $\lambda < 1500$ nm, and the device annealed at 300°C shows the highest photoresponsivity for $\lambda > 1500$ nm.

Au nanoislands should essentially represent the wavelength dependent generation rate of hot electrons. We use finite-difference time-domain (FDTD) simulations to calculate the absorption spectra of the Au nanostructures on Silicon in order to investigate the plasmonic effects on Au nanoislands and compare the theoretically expected hot electron generation rate with the experimental results.

4.7 FDTD Simulations

Finite-difference time-domain (FDTD) simulations were carried out by using Lumerical FDTD Solutions. We used ellipsometry measurements (J.A. Woollam Co. Inc. VASE ellipsometer) to extract the complex refractive index (n, k) of the AZO layer. We used the data from literature for the optical constants of Au and Si [69, 70]. We conducted two sets of simulations. In the first set of simulations, we simulated mono-sized Au nanoparticles on Silicon substrate and monitored the absorption spectra of Au nanoparticles. Nanoparticles are periodically distributed (period = 1000 nm) on the substrate and covered by an AZO layer. In order to observe the effect of nanoparticle size on the absorption spectrum, nanoparticles with sizes 80 nm, 90 nm, 100 nm and 110 nm are simulated [14].

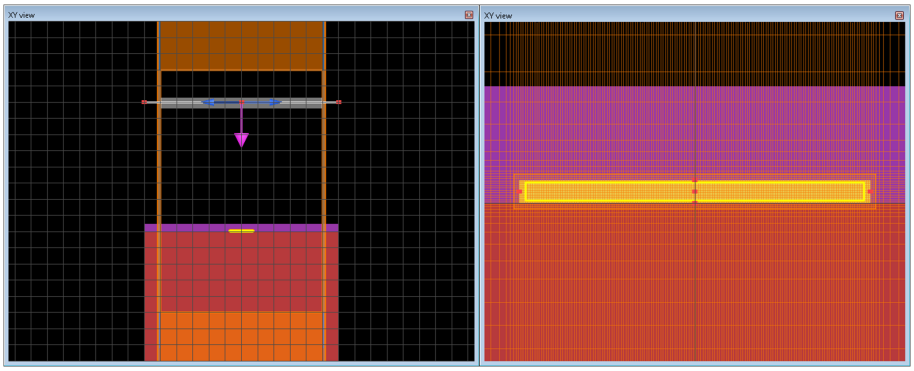

Figure 4.11: Cross-sectional view of the 3-D simulation environment used in the first set of simulations. The structure consists of a Si substrate, Au nanoparticle and AZO top contact. Periodic boundary conditions are used for the x-axis (the horizontal axis in the images) and z-axis (perpendicular to the image plane). Perfectly matched layer (PML) boundary conditions are used for the y-axis (vertical axis in the images).

The simulated absorption spectra of the identical Au nanoparticles show the effect of LSPR excitation. We achieve resonant absorption enhancement at the NIR wavelengths by the excitation of LSPR on Au nanoparticles. The resonance wavelength makes a red-shift as the size of the identical nanoparticles increases (Fig. 4.12).

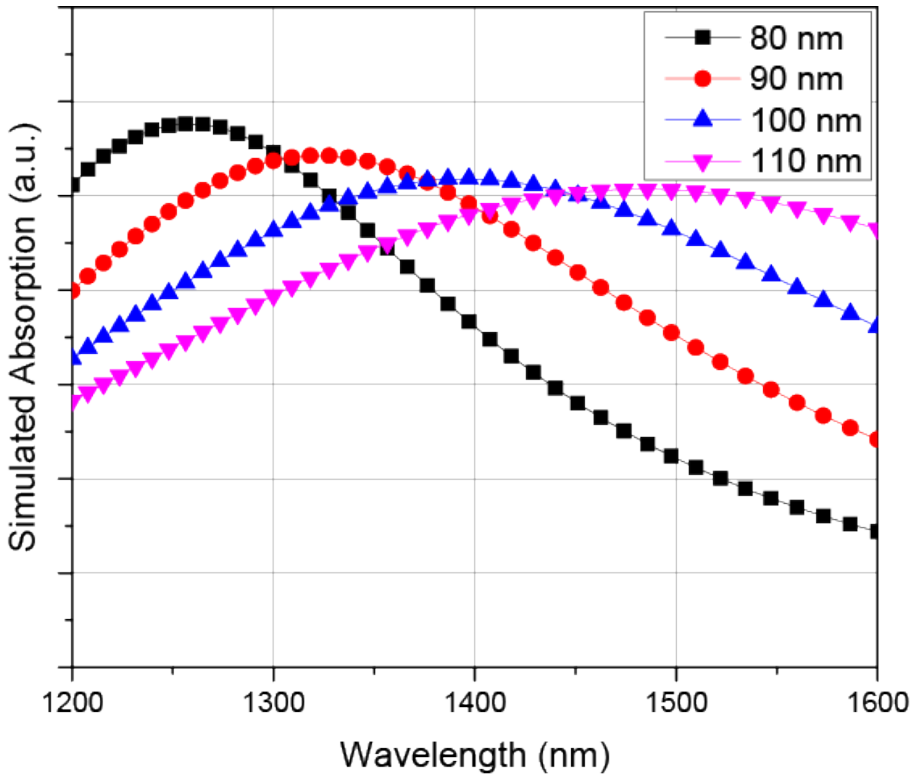

Figure 4.12: Simulated absorption spectra of the identical Au nanoparticles on Si substrate covered by AZO layer. Surface plasmon resonance results in an absorption peak at the NIR wavelengths and the wavelength of the resonance red-shifts as the nanoparticle size increases.

In the second set of simulations, we import the corresponding SEM images of the fabricated samples annealed at 300°C, 450°C and 600°C to the FDTD software and calculate the absorption spectra of the randomly shaped Au nanoislands. A small portion of the SEM image is used as the unit cell and assumed to be periodic in both x and y directions. Perfectly matched layer (PML) boundary conditions are used for the z-axis (Fig. 4.13).

Combined response of individual plasmonic resonators with various sizes results in a broad-band absorption enhancement. As the annealing temperature decreases, the average particle size increases and the absorptivity of the structure increases at the NIR wavelengths (Fig. 4.14).

Simulated absorptivity spectra give the wavelength dependent hot electron

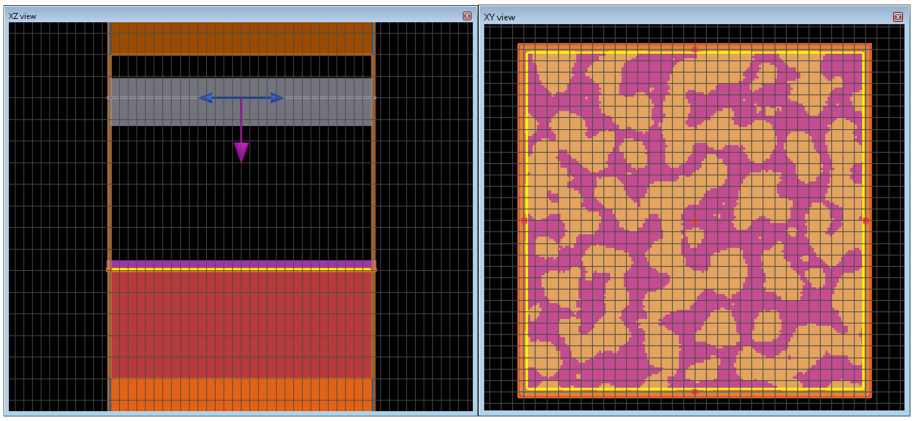

Figure 4.13: Cross-sectional view of the 3-D simulation environment used in the second set of simulations. The structure consists of a Si substrate, randomly shaped Au nanoislands and AZO top contact. Perfectly matched layer (PML) boundary conditions are used for the z-axis (a). Periodic boundary conditions are used for the x-axis and y-axis (b).

generation rate for each case and these spectra need to be multiplied by the corresponding hot electron collection efficiency in order to calculate the photoresponsivity spectra [14]. The efficiency of the hot electron collection process, namely the internal photoemission process, is given by the Fowler function [29, 67]:

$$\eta = C_F \frac{h\nu - q\varphi_B}{h\nu} \tag{4.1}$$

where C_F is the Fowler emission coefficient, $h\nu$ is the energy of the incident photons and φ_B is the Schottky barrier height. If we assume unity quantum efficiency and neglect any other wavelength dependent factors (such as the mean free path of electrons in the metal), multiplying the Fowler function by the calculated absorption spectra gives the photoresponsivity spectra [12]. We fit these results to the experimental photoresponsivity results for each annealing condition and with this fitting the Schottky barrier height is calculated to be approximately 0.7 eV, which is an expected value for such junctions [67]. The calculated photoresponsivity profiles of the samples are in good agreement with the experimental photoresponsivity results (Fig. 4.15). This agreement indicates we can model the hot electron generation rate and hot electron collection efficiency with the decay rate of surface plasmons and the efficiency of the internal photoemission process. We also note that the electromagnetic field in the bulk of the metal is considered in order to calculate the hot electron generation rate, which is also

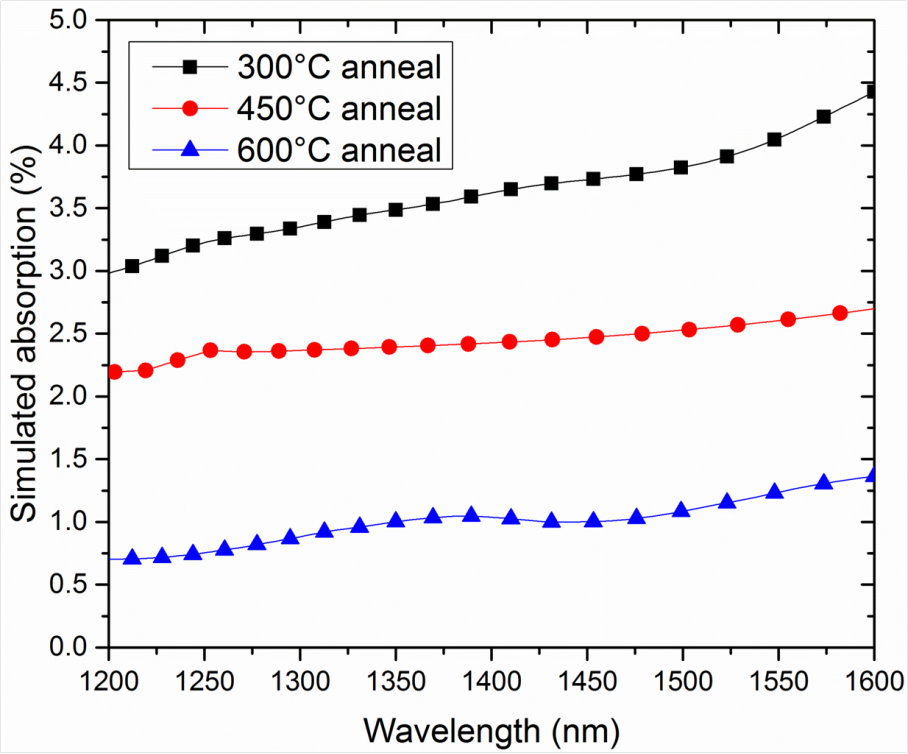

Figure 4.14: Simulated absorption spectra of the randomly shaped Au nanoislands on Si substrate covered by AZO layer. The random shape of the Au nanoislands was obtained by importing a unit cell from the SEM images and assuming the unit cell to be periodic in x and y directions. Overall response of randomly shaped plasmonic resonators results in a broad-band absorptivity spectrum. The device annealed at the lowest temperature (300°C) has the largest average nanoisland size hence shows the highest absorptivity at the NIR wavelengths and the absorption increases as the wavelength increases.

called *the volume photoelectric effect* [71]. Another approach could be to consider the emission of an electron as a result of the electric field at the surface of the metal, which is called *the surface photoelectric effect*. In that case the square of the component of the electric field normal to the metal surface would determine the photoemission process instead of the square of the complete electric field in the bulk [71]. The surface photoelectric effect is not investigated in this study and the volume photoelectric effect is used to model the hot electron generation rate with sufficiently good accuracy.

As shown in the SEM images (Fig. 4.4) and the particle size histograms

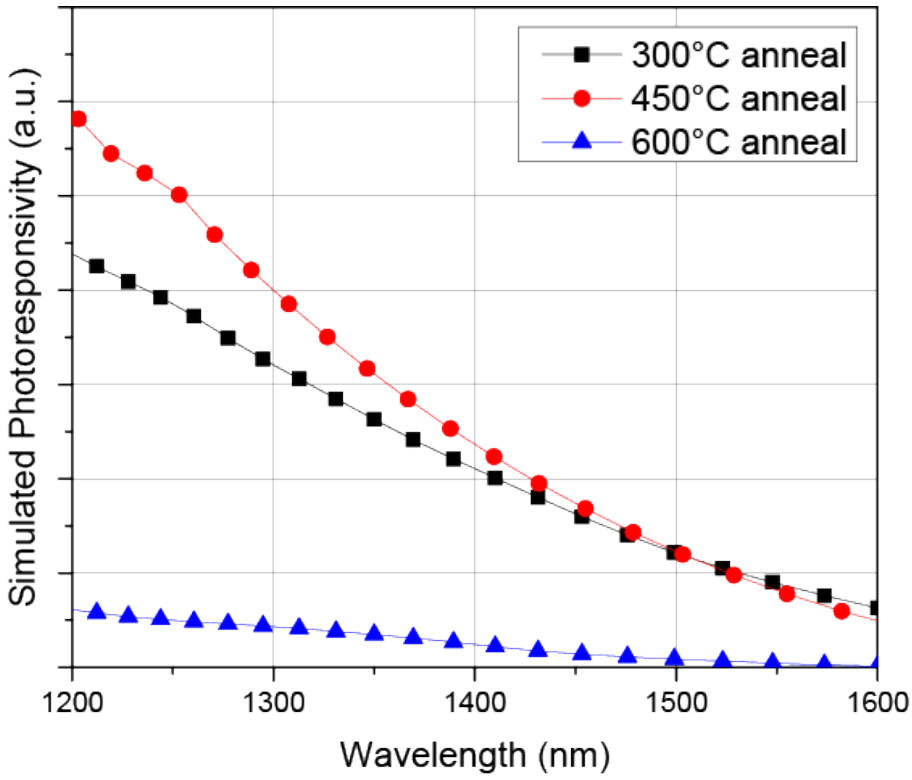

Figure 4.15: Calculated photoresponsivity spectra for the samples annealed at 300°C, 450°C and 600°C. Photoresponsivity spectra are calculated as the product of the absorption spectra shown in Fig. 4.14 and the Fowler function. Fowler emission coefficient and the Schottky barrier height are used to fit the calculated absorption spectra to the experimental results.

(Fig. 4.5), the sample annealed at 300°C has larger and elongated nanoislands compared to the sample annealed at 450°C. These larger nanoislands are expected to red-shift the wavelength of the surface plasmon resonance. Hence, the LSPR of the sample annealed at 300°C is expected to be stronger in longer wavelengths and weaker in shorter wavelengths, resulting in higher photoresponsivity values at longer wavelengths. The crossover point of the photoresponsivity spectra of the samples annealed at 300°C and 450°C is predicted to be at $\lambda = 1500$ nm by the simulations, which agrees very well with the measured crossover point.

4.8 Conclusion

We have achieved hot electron based NIR photodetection on Si substrates. No additional doping or epitaxial growth processes are involved to obtain NIR absorption. Metal nanoislands obtained with an easy and fast method are used to excite LSPRs and generate hot carriers. Broad-band NIR photodetection on Si is achieved by utilizing the hot electron collection mechanism. We characterized photoresponse from our devices up to 2000 nm wavelength. Responsivity at 1.3 μm and 1.55 μm are 2 mA/W and 600 μA/W, respectively. These results are on the same order as the responsivity values of the recently published narrow-band plasmonically tuned photodetectors in the literature [13]. Besides comparable responsivity and wideband operation, another important advantage of our approach is to avoid the use of slow and costly nanofabrication techniques such as electron beam lithography or focused ion beam. By improving the nanoisland formation process and optimizing the Schottky junction and the TCO layer highly efficient NIR photodetection at ultra low-cost can be possible. We also showed that the photoresponse of these devices can be modeled as the product of the hot electron generation rate and hot electron collection efficiency. Absorption spectrum of the device which was calculated by FDTD simulations was used as an approximation to the hot electron generation rate, whereas the Fowler function was used to model the hot electron collection efficiency. A model that can fit quite accurately to the experimental results was obtained.

Chapter 5

Double MIM Photovoltaic Device

This chapter is based in part on the publication "Plasmonically enhanced hot electron based photovoltaic device," F.B. Atar, E. Battal, L.E. Aygun, B. Daglar, M. Bayindir and A.K. Okyay, *Optics express*, vol. 21, no. 6, pp. 7196-7201, 2013.

5.1 Introduction

The concept of hot electron based photovoltaic devices is emerging as a candidate for low cost and ultra thin solar cells. One of the simplest architectures for hot electron based photovoltaics is a metal-insulator-metal (MIM) structure that acts as a tunneling diode. Simple device architecture and very fast operation frequency are the main advantages of MIM diodes. Due to this fast operation capability, use of MIM diodes as optical rectennas (rectifying antenna) has been proposed for the direct conversion of the optical power to DC electrical current [72]. This approach has been demonstrated at microwave frequencies and more than 90% conversion efficiency has been achieved [73]. The requirements for a rectenna to operate at optical frequencies are very strict and the most important challenges are related to

the diode resistance, capacitance, and reverse bias-leakage [72]. As an alternative approach which avoids these problems, instead of modulating the entire sea of electrons in an MIM rectenna, one can design to achieve absorption mostly in one of the metal layers and excite hot electrons to generate photocurrent.

When there is normally incident light on an MIM structure, a portion of the incident light is absorbed in the top metal layer, most of the light is reflected back, and if the top metal is sufficiently thin, a very small amount of light propagates to the bottom metal layer to be absorbed therein. As the amount of light absorbed in the metal layers are different from each other, so are the rates of generation of hot electrons in these layers. The generated hot electrons from each metal can travel to the other metal, resulting in competing current flows between the top and bottom metal layers of the MIM structure. Since the absorption in one of the metal layers is significantly larger than the other metal layer, there is a photogenerated net current flow in the illuminated MIM structure which results in photovoltaic action [23].

A major limitation of the MIM photovoltaic devices is the high optical reflection from the metal surface. In order to overcome this problem, plasmonic means can be utilized to confine the light on the metal surface and enhance the optical absorption in the metal layer (Fig. 5.1) [23]. Wang *et al.* demonstrated an MIM device fabricated on a prism and excited surface plasmons on the MIM device in Kretschmann configuration. Surface plasmons are tightly localized to the metal-dielectric interface and encounter a higher absorption compared to the bulk absorption in the metal. As a result, surface plasmon assisted hot electron generation in such a device configuration yields several times better efficiency compared to hot electron generation through bulk absorption. Researchers have also proposed to pattern one of the metal layers so that surface plasmons would be excited under normal incidence without using a prism or index matching [74]. Still, obtaining the desired plasmon excitation structure without distorting the electrical properties of the MIM diode remains challenging. We study a novel double MIM (metal-insulator-metal-insulator-metal, MIMIM) hot electron based device architecture with separate MIM junctions for hot electron collection and

plasmon excitation. This approach allows independent optimization of the plasmon excitation structure and the MIM diode. We experimentally demonstrate more than an order of magnitude short circuit current enhancement of the MIM hot electron photovoltaic device by surface plasmon excitation [25].

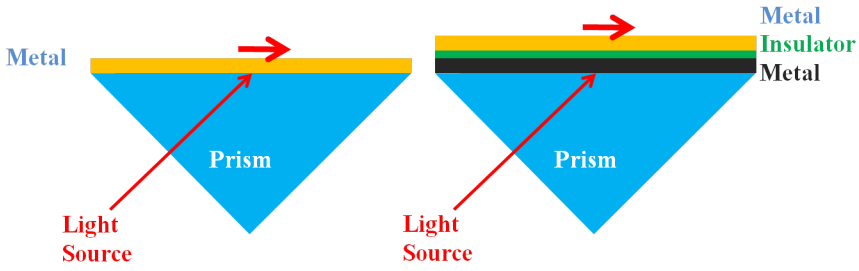

Figure 5.1: (a) Surface plasmon excitation on the metal-air interface by using a prism in Kretschmann arrangement. (b) Use of Kretschmann arrangement to excite surface plasmons on the metal-air interface of an MIM photovoltaic device

5.2 Device Design

The bottom MIM junction in our device configuration is formed by Au-HfO_2-Al layers. The top MIM is formed by depositing an insulating spacer layer (Al_2O_3) on the bottom MIM and randomly coating Au nanoparticles on the insulator layer. The device structure is shown in Fig. 5.2(a). Au nanoparticle (Au NP)-Al_2O_3-Au layers constitute the top MIM structure and Au-HfO_2-Al layers constitute the bottom MIM junction [25]. The top view scanning electron microscope (SEM) image of the device in Fig. 5.2(b) shows the randomly distributed Au nanoparticles as white dots on the surface.

Energy band diagram of the MIM diode is shown in Fig. 5.3. The energy levels of the metals would be aligned in equilibrium but is shown to be separated by the difference of their work functions, which would be the case when the device is in short circuit configuration ($V_{bias} = 0$ Volt). When a photon is absorbed in the metal layer it generates a hot electron which can be collected at the junction to generate photocurrent by the internal photoemission process. The generated hot

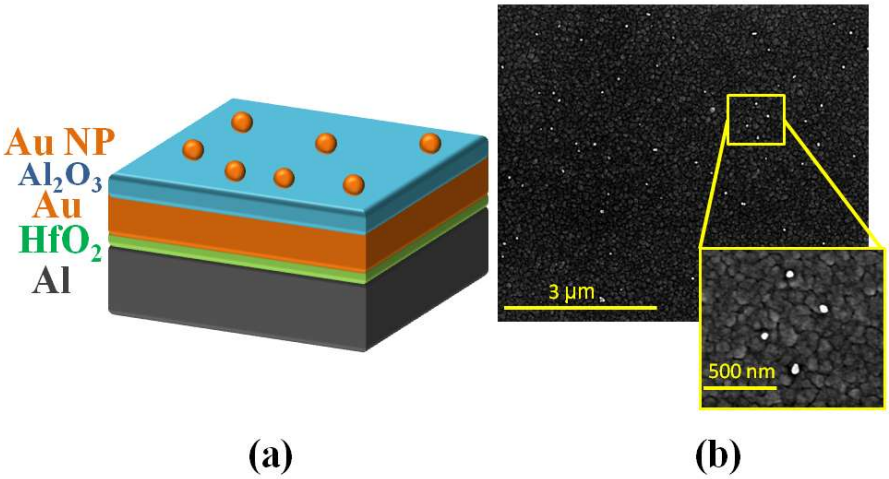

Figure 5.2: (a) The schematic view of the proposed hot electron based photovoltaic device architecture. Au-HfO_2-Al layers (bottom MIM) acts as a diode. Au NP-Al_2O_3-Au layers excite surface plasmons under direct illumination and localize the electromagnetic field in the Au layer. (b) SEM image of the Au nanoparticles randomly distributed on the device surface.

electron diffuses in a random direction in the metal [75] and only approximately 2% of such hot electrons can travel sufficiently normal to the insulator interface and has momentum to traverse the potential barrier [72]. As the hot electrons travel in the metal they quickly lose their excess energy and the distance that a hot electron can travel is limited by the hot electron attenuation length, which is 74 nm for the hot electrons in Au [30]. This limit also indicates that the hot electrons generated in close proximity of the metal-insulator interface would have higher probability to reach the junction without losing their excess energy and cross the potential barrier to reach the other metal layer.

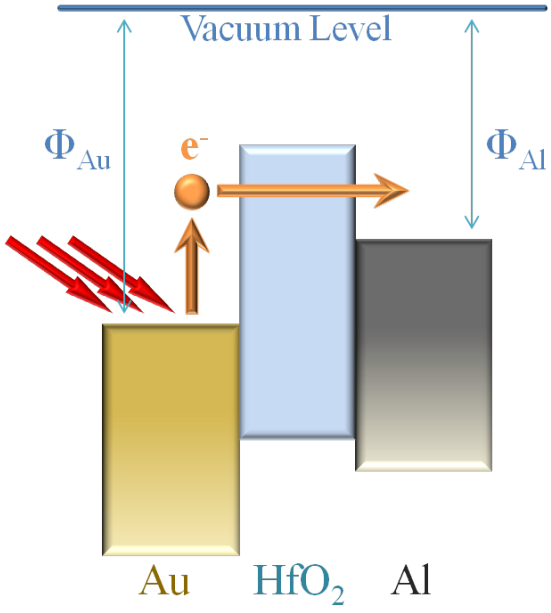

Figure 5.3: The energy band diagram of the MIM diode with Au-HfO_2-Al layers. The photoexcited hot electrons diffuse in random directions in the Au layer. The hot electrons that reach the junction with sufficient momentum normal to the Au-HfO_2 interface can travel over the potential barrier or tunnel through it and generate photocurrent (internal photoemission).

5.3 Tunneling Through the Insulator

The hot electrons that do not have sufficient energy to go over the potential barrier can tunnel through the potential barrier and generate photocurrent. The probability of hot electron tunneling through an insulator barrier is strongly dependent on the insulator thickness [76]. The direct tunneling and Fowler-Nordheim tunneling mechanisms are discussed in Chapter 2 for MIS diodes and the main principles are similar for MIM diodes. The tunneling probability decreases with increasing insulator thickness, which in turn decreases the photocurrent in an MIM device. Wang *et al.* report that the probability of tunneling through a barrier would be too small compared to the photoemission probability over the barrier. Hence the power generated from the electrons with energies smaller than the barrier height would be negligible compared to the power generated from the higher energy electrons [23].

We used 4-nm-thick insulator in our design in order to obtain sufficiently high photocurrent. Lower insulator layer thickness may seem to increase the tunneling probability (and improve hot electron collection efficiency), however a sufficiently thick potential barrier must be present to block the thermionic current from the other metal layer. For this purpose the optimal barrier height was also reported to be approximately 0.37 eV for room temperature applications under illumination by solar AM1.5 spectrum [23]. Using a too thin insulator thickness would increase the dark current of the MIM diode and decrease the open-circuit voltage of the photovoltaic device. We are also constrained technologically in minimum thickness to form a continuous layer to avoid electrical shorting [25].

5.4 FDTD Simulations

A planar MIM structure acts as a plasmonic waveguide and supports propagating surface plasmon polariton (SPP) modes at metal-insulator interfaces. The surface plasmon modes of this waveguide cannot be excited by normally incident light in a planar MIM configuration. However, scattering from a nanostructure could excite SPPs at these waveguide modes [25, 47]. In order to investigate surface plasmon excitation in our double MIM structures, we performed finite-difference time-domain simulations of the proposed structure using FDTD Solutions by Lumerical Inc. We use data from the literature for the dielectric constants of Au, Al, Al_2O_3 and HfO_2 [70, 77]. A single nanoparticle on top of an MIM structure with an Al_2O_3 spacer layer is assumed in a unit cell of the simulation environment and this unit cell is repeated with 500 nm period along the plane of the metal layers (x and y directions). Perfectly matched layer (PML) boundary conditions are used for the axis perpendicular to the metal layers (z-axis), and a plane wave source is placed to illuminate the sample with normal incidence, directed down the z-axis. In order to calculate the enhancement provided by the Au nanoparticles, simulations are also carried out without the Au nanoparticles.

Fig. 5.4 depicts the electric field intensity profiles of the bare MIM structure (Fig. 5.4(a)) and the MIM structure with Au nanoparticles (Fig. 5.4(b)) [25]. The

MIM device with Au nanoparticles shows plasmonic resonance peak at 590 nm wavelength, hence the electric field intensity profiles of Fig. 5.4 are drawn at this wavelength.

When the nanoparticles are not present on the MIM device, there is no nanostructure to excite localized surface plasmon resonances on the MIM device and the surface plasmon polariton modes of the planar MIM structure can not be excited. Only a very small fraction of the incident light penetrates into the Au layer and could be absorbed therein (Fig. 5.4(a)).

When there are Au nanoparticles on the MIM device, localized surface plasmons (LSP) are excited at the nanoparticles, confining the light into very small volumes and achieving several times higher electric field inside the metal layer. LSP modes interact with the underlying Au layer and trigger the dark modes on the Au-Al_2O_3 interface of the top MIM [78], significantly increasing the optical absorption. These LSP modes on the surface of the top MIM also couple to the bottom MIM, excite propagating SPP modes along the Au-HfO_2 interface and increase the optical absorption in the vicinity of this interface. Since this interface is the hot electron collection junction, hot electrons photogenerated close to this junction have higher probability of contributing to the photocurrent compared to the ones generated at the top of the Au layer. The hot electrons generated far away from the junction will lose their excess energy as they travel in the Au layer and the distance they can travel is governed by the hot electron attenuation length, which depends on the metal type [31].

FDTD simulation results are used to plot the ratio of the total optical absorption inside the Au layer for the two cases (MIM with Au nanoparticles and bare MIM). This ratio shows the absorption enhancement inside the Au layer due to the excitation of surface plasmons on Au nanoparticles (Fig. 5.5) [25]. Enhanced absorption in the Au layer would correspond to increased generation rate of hot electrons. The photocurrent will also increase proportional to the hot electron generation rate as explained in the previous chapters.

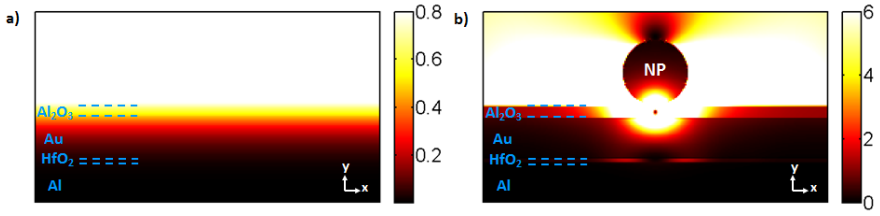

Figure 5.4: Electric field intensity profiles at $\lambda = 590$ nm obtained by FDTD simulations (a) Planar MIM structure without Au nanoparticles. Incident light is mostly reflected back and only a very small portion of the electromagnetic field can penetrate into the metal layer to be absorbed by the metal (b) MIM structure with Au nanoparticles on top. Au nanoparticles excite LSPRs and trigger SPP modes at metal-insulator interfaces, which significantly enhance the electromagnetic field in the Au layer. Scattering of light by these nanoparticles also excite the dark modes in the underlying MIM structure.

5.5 Fabrication of Double MIM Structures

Silicon wafer with approximately 300 nm SiO_2 layer is used as substrate. The fabrication can be done on any substrate with sufficiently flat surface and we preferred to use Si wafer due to its very small surface roughness. The thick SiO_2 layer ensures electrical isolation of Si wafer from the devices that will be fabricated on it. 150-nm-thick Al is deposited with thermal evaporation and patterned by photolithography and lift-off. Approximately 4-nm-thick HfO_2 is deposited in atomic layer deposition (ALD) system with 40 ALD cycles (Cambridge Nanotech Inc., Savannah S100). 30 nm Au is deposited with thermal evaporation as the top metal, and a thin (< 5 nm) Cr layer is evaporated prior to Au evaporation as adhesion promoter. After patterning the Au layer, 150 nm Al was deposited with thermal evaporation as the contact metal. Approximately 10-nm-thick Al_2O_3 was deposited as the top insulating layer in atomic layer deposition system with 100 ALD cycles [25].

Au nanoparticles are synthesized by slightly modifying the Turkevich method as explained in Chapter 4 [25, 65]. Synthesized nanoparticles were spin-coated on the Al_2O_3 layer at 1000 rpm. Measured absorption spectrum of the synthesized

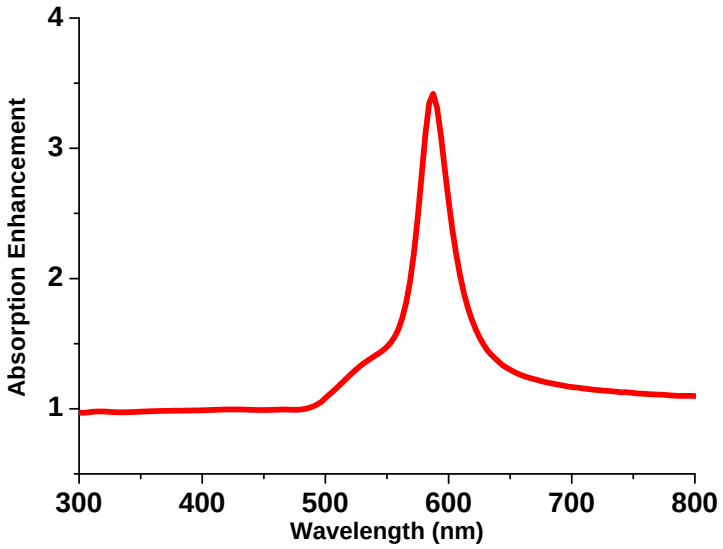

Figure 5.5: Enhancement of the absorption in the Au layer due to the excitation of LSPRs on Au nanoparticles and excitation of SPPs on metal-insulator interfaces. Total absorption spectra in the metal layer are calculated with FDTD simulations for the two cases: (i) MIM device with Au nanoparticles (ii) bare MIM device (without Au nanoparticles). The absorption enhancement spectrum is calculated as the ratio of the simulated total absorption spectra of these two cases.

Au nanoparticles in de-ionized water solution is plotted in Fig. 4.2. Au nanoparticles show absorption resonance at around 530 nm wavelength in de-ionized water solution [25].

5.6 Optoelectronic Characterization

Photoresponsivity measurements are performed by illuminating the samples with a modulated light source and measuring the short circuit current with a lock-in amplifier (SR830). A Xenon-lamp illuminator is used as the light source and the light is monochromated with Oriel 74004 monochromator (1/8 meter, 1200 lines/mm grating) in the 300-800 nm wavelength range. The monochromated light is collimated with a lens, modulated by a mechanical chopper and focused

on the devices with another lens. A calibrated Si detector is used to measure the optical power of the monochromated light at each wavelength by placing Si detector at the position of the sample. This optical power spectrum is used to normalize the measured photocurrent and calculate the photoresponsivity of the device at each wavelength. The beam size of the focused light was larger than the active device area, thus the optical power incident on the device is slightly smaller than the one measured by the Si detector therefore the responsivity values reported here are slightly smaller than the actual values [25].

Fig. 5.6 plots the measured photoresponsivity of a bare MIM device and an MIM device with Au nanoparticles on top. Excitation of surface plasmons at the Au nanoparticles results in resonant photoresponsivity enhancement at around 700 nm wavelength. At the resonance wavelength, we record more than 7 times enhancement in the measured short circuit current compared to the reference MIM device. The wavelength of the experimentally measured resonance peak (inset of Fig. 5.6) is approximately 100 nm red-shifted compared to the simulation results (Fig. 5.5) [25]. This shift could be attributed to possible variation of the dielectric properties of the materials used in the simulations from the actual values. SEM images of the devices also show that the bottom Al layer is quite rough and has large grains. These non-idealities in the fabricated device also give a mismatch between the experimental results and the simulation results.

As seen in Fig. 5.2(b) the Au nanoparticles are quite sparsely distributed on the MIM surface but still more than 7 times photoresponsivity enhancement factor could be obtained. Such considerable enhancement despite the little amount of Au nanoparticles indicates a significant potential for the enhancement of hot electron based MIM devices with surface plasmon excitation on metal nanoparticles. It is also important to note that this enhancement is obtained without any modification to the MIM diode and different plasmonic designs could be implemented in the same way.

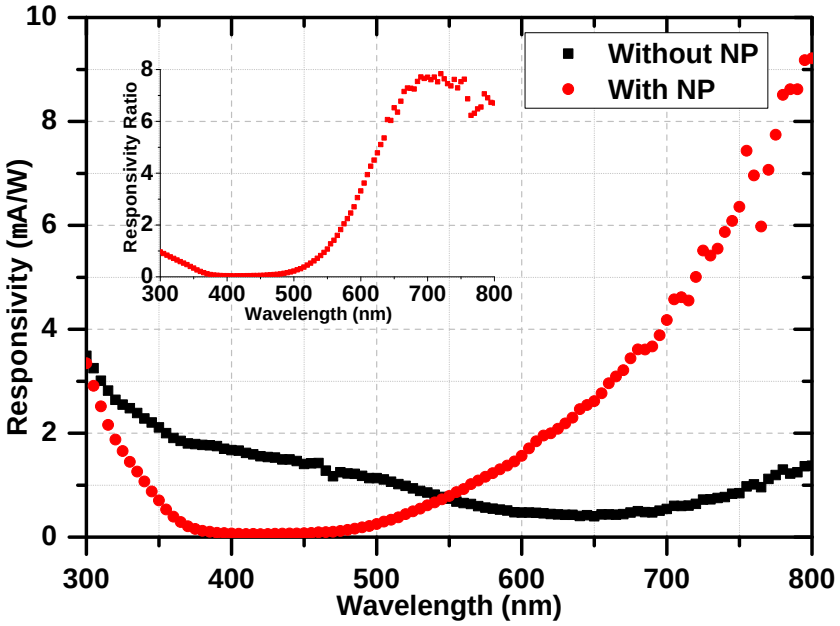

Figure 5.6: Measured photoresponsivity of the MIM device before and after the spin coating of Au nanoparticles. The inset plots the ratio of the photoresponsivity spectra of two measurements. The device with Au nanoparticles shows resonant enhancement at around 700 nm wavelength.

5.7 Modifications to the Double MIM Photovoltaic Device

5.7.1 Surface Roughness

Top view SEM images of the sample surface indicated very high surface roughness (Fig. 5.7(a)). We investigated the effect of thermal evaporation rate of the bottom metal layer on the roughness of the coated layer. Increasing the evaporation rate from 0.7 Å/s to 5 Å/s yielded significantly smoother metal surface (Fig. 5.7(b)). We suspect that the evaporated metal slowly oxidizes during the deposition process, which prevents the metal from forming a smooth layer, and the effect of this oxidation could be minimized by increasing the evaporation rate.

Short circuit photocurrent measurements of the MIM devices on smooth metal

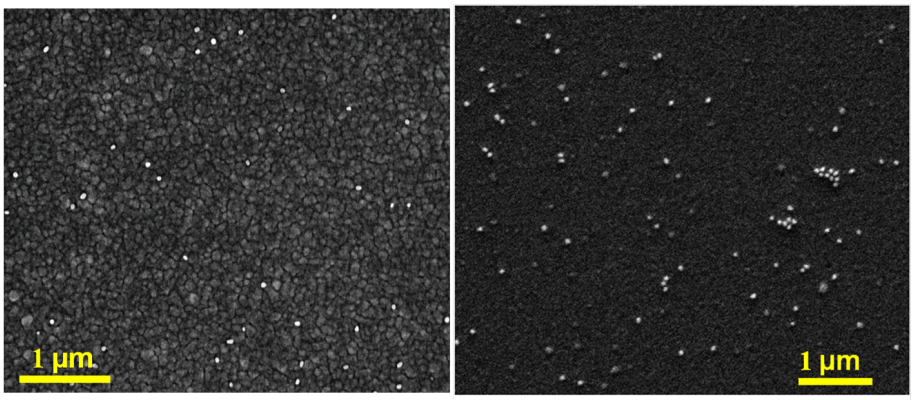

Figure 5.7: Top view SEM images of completed MIM devices with spin coated Au nanoparticles. Bottom metal (Al) was thermally evaporated on Si substrate at (a) 0.7 Å/s deposition rate (b) 5 Å/s deposition rate.

surface showed higher plasmonic enhancement than the ones obtained in initial experiments (Fig. 5.8). The center wavelength of the plasmonic resonances (Inset of Fig. 5.8) also matches better with the simulations and we observe plasmonic resonances centered around 600 nm wavelength (Fig. 5.5). This result also indicates that the surface roughness causes a red-shift in plasmonic resonances. Responsivity reduction at ultraviolet (UV) wavelengths after nanoparticle coating also does not occur when smooth metal surface is used as the bottom metal.

5.7.2 Au Core-SiO_2 Shell Nanoparticles

In the initial experiments, the bottom MIM junction was capped with an insulator layer and Au nanoparticles were spin coated on the top dielectric layer to form the top MIM structure. Instead of this approach, we spin coated Au core-SiO_2 shell nanoparticles on bottom MIM junction to form the top MIM structure. Use of a core-shell structure would give flexibility for the design of nanoparticles to obtain different plasmonic resonances. In this study, the measured absorption spectrum of Au core-SiO_2 shell nanoparticles in water solution was almost identical to that of Au nanoparticles, therefore very similar photoresponsivity results were expected when these nanoparticles were used on MIM devices. The responsivity measurements did not show plasmonic enhancement in the visible wavelengths

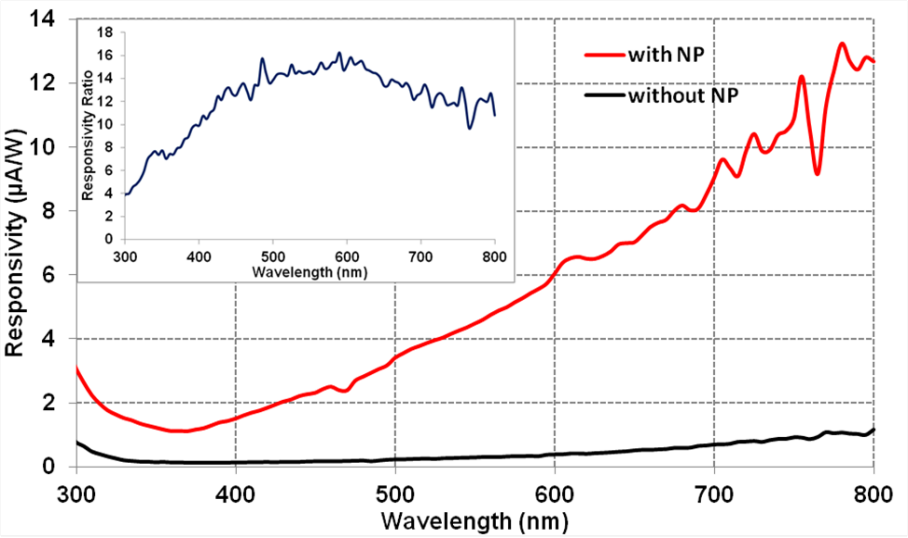

Figure 5.8: Measured photoresponsivity of the MIM device before and after the spin coating of Au nanoparticles. The inset plots the ratio of the photoresponsivity spectra of two measurements. When the surface roughness is reduced, the plasmonic resonances make a blue-shift and the center frequency of the plasmonic resonance moves to 600 nm wavelength.

but there was significant enhancement in the UV wavelengths ($\lambda < 400$ nm) (Fig. 5.9). We do not attribute this enhancement to plasmonic effects since it happens above the plasma frequency of gold, but such an enhancement of UV absorption in similar Au core-SiO_2 shell nanoparticles was also observed in previous reports [79, 80].

5.7.3 Au Nanorods

Another approach to control the center frequency, the width and the strength of the plasmonic resonances is to use elongated nanoparticles, namely nanorods, instead of spherical nanoparticles. The localized surface plasmon resonances on spherical and elliptical nanoparticles are discussed in Chapter 3. Similar to elliptical nanoparticles, we expect these nanorods to show red-shifted plasmonic resonances compared to spherical nanoparticles of the same volume. Transmission electron microscope (TEM) image of Au nanorods we have used in this study is shown in Fig. 5.10.

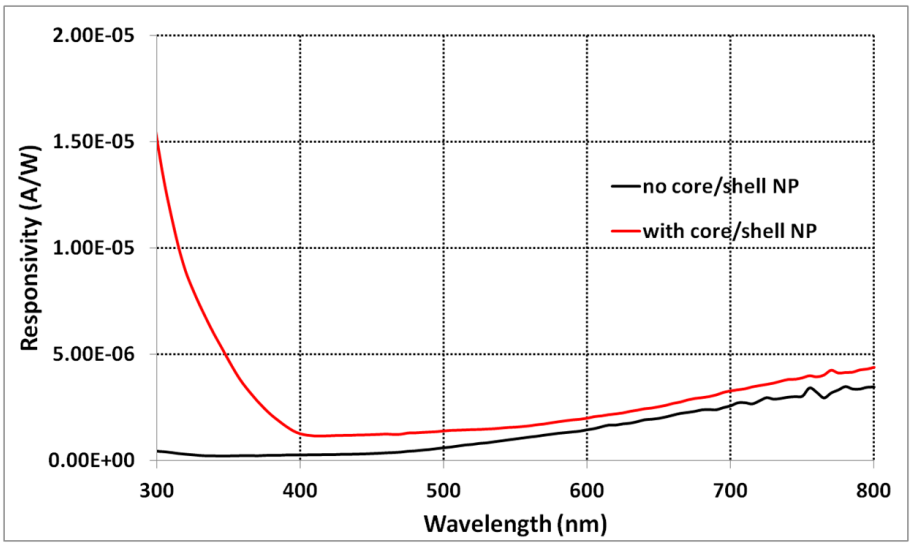

Figure 5.9: Measured photoresponsivity spectrum of the device before and after the spin coating of Au core-SiO_2 shell nanoparticles. No resonant photocurrent enhancement is observed. Absorption enhancement occurs below the resonance frequency of Au nanoparticles, at UV wavelengths.

Short circuit photocurrent values of the reference MIM devices and the MIM devices with nanorods were measured to determine the responsivity of the devices at different wavelengths (Fig. 5.11). Observed plasmonic enhancement with nanorods was red-shifted when compared to the plasmonic enhancement obtained with nanoparticles, as predicted by the analysis in Chapter 3. Absorption enhancement peak is wider when nanorods are used which is an expected result as the plasmonic resonances move to longer wavelengths.

The short circuit photocurrent measurement was also made in the 800 nm - 1300 nm range (Fig. 5.12) but responsivity calculation by dividing the measured photocurrent by the incident light power was not made. The emission peaks of the Xe lamp resulted in artificial photocurrent peaks in the measurements but still the photocurrent enhancement due to nanorods could be clearly observed.

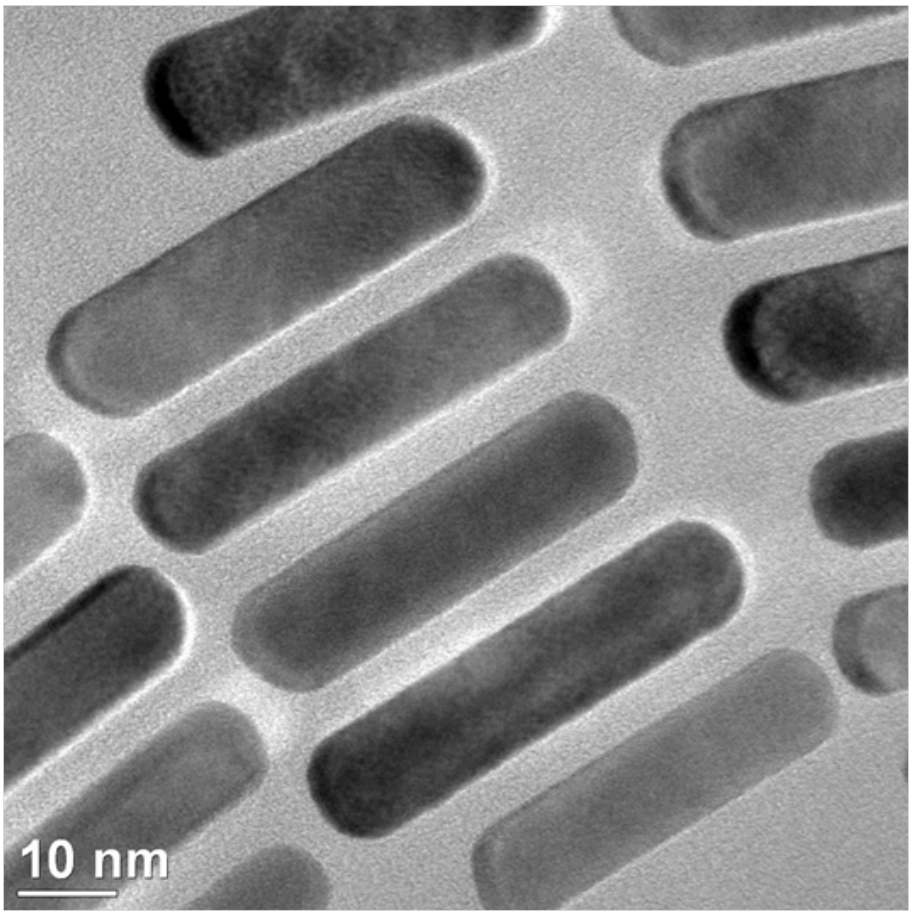

Figure 5.10: TEM image of Au nanorods we have used in this study. Due to their elongated shape, nanorods are expected to show red-shifted plasmonic resonances compared to spherical nanoparticles.

5.8 Conclusion & Future Directions

A novel plasmonically enhanced hot electron based photovoltaic device with separately formed hot electron collection and plasmon excitation MIM junctions is demonstrated. Excitation of localized surface plasmon resonances (LSPRs) on Au nanoparticles results in high field localization in the MIM photovoltaic device. LSPRs on Au nanoparticles also couple to the dark MIM modes and trigger propagating surface plasmon polariton (SPP) modes, resulting in more than an order of magnitude enhancement in the photoresponsivity at the resonance wavelength. The simple planar structure of the MIM device and spin coating of chemically synthesized Au nanoparticles for plasmon excitation allows large area fabrication

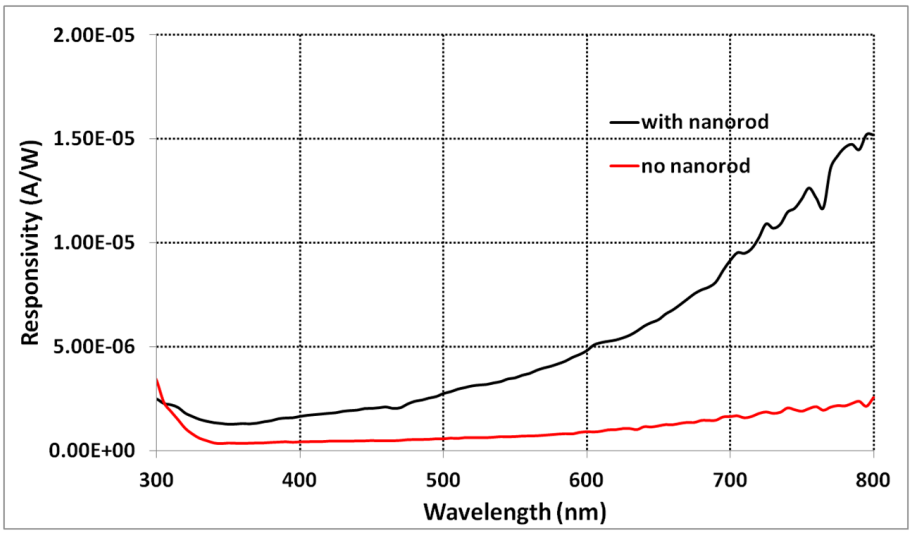

Figure 5.11: Measured photoresponsivity of the device before and after the spin coating of Au nanorods. The device with nanorods shows resonant enhancement at around 800 nm wavelength. The plasmonic resonances are red-shifted compared to the devices with spherical nanoparticles (Fig. 5.8).

of this device. Plasmon excitation structures are introduced without modifying the rectifying MIM junction, which gives flexibility to separately optimize the electrical and optical properties of the MIM hot electron photovoltaic device. Au nanoparticles, Au core-SiO_2 shell nanoparticles and Au nanorods were used on similar MIM junctions to observe different photonic and plasmonic effects. Detailed FDTD simulations of such structures are conducted to have a better understanding of the theory.

Overall efficiency of the MIM diodes are very low, hence a study to improve the electrical junction is necessary. Wang *et al.* attribute the low efficiency mostly to the surface recombination at the interface and report that only 0.01% of the hot electrons could be collected at the interface before they recombine at the trap states [23]. Improving the electrical properties of the metal insulator interfaces remains as the main challenge to increase the photovoltaic efficiency of MIM devices.

In order to improve the rectifying property of MIM diodes, different metals could be used to provide different asymmetry at the MIM junction. Thickness of

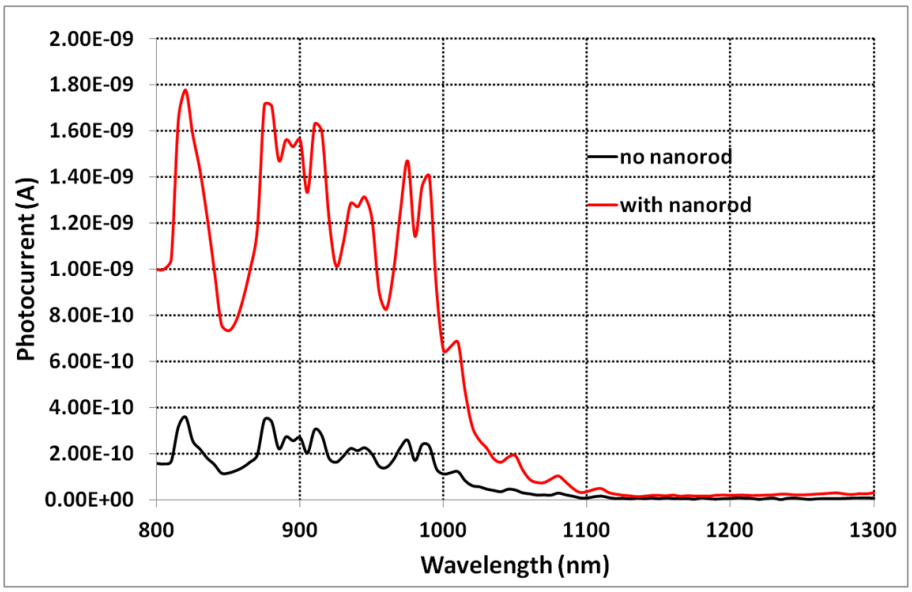

Figure 5.12: Measured photocurrent of the MIM device before and after the spin coating of Au nanorods. The device with nanorods shows resonant enhancement at around 800 nm wavelength. There are artificial photocurrent peaks due to the emission peaks of the Xe lamp that is used as the light source. Still the enhancement of the photocurrent by the excitation of localized surface plasmons on nanorods is clearly visible.

the metal layers, especially the thickness of the top metal, could also be optimized. Using a too thick top metal (> 100 nm) would result in hot electron generation far away from the surface. The hot electrons would then lose their energy to the lattice before reaching the junction. Using a very thin metal layer (< 15 nm), on the other hand, would allow optical field penetration to the bottom metal, resulting in a decrease in the net photocurrent. Although the excitation of surface plasmons helps confine the light to very thin metal films, attention must be paid to prevent electromagnetic field from coupling to the bottom metal [23]. Using too thin top metal would also increase the series resistance of the device and degrade photovoltaic efficiency.

The tunneling probability through the insulator layer should be high in order to collect more photocurrent and this probability is governed by the thickness and the bandgap of the interlayer dielectric. Experiments could be repeated with different interlayer dielectric materials and with different dielectric thicknesses.

Another approach to improve electrical junction is to carry the hot carriers on the conduction band of a semiconductor instead of tunneling them through the energy bandgap of an insulator [81]. Different semiconductors such as ZnO and TiO_2 could be used as interlayer material to carry the hot electrons generated in the top metal layer to the other metal layer.

Recent studies in the field of plasmonics have also shown that MIM structures could be used to obtain high absorption in gold or other metals. Engineering the plasmonic effects in an MIM structure and achieving high absorption with MIM structures have been investigated in the literature [26, 27, 28]. Our work on the engineering of the absorption in our double MIM device architecture is presented in the following chapter.

Chapter 6

Absorption Engineering in Double MIM Hot Electron Based Photovoltaic Device

6.1 Introduction

The previous chapter introduces a double metal-insulator-metal (MIMIM) structure as a hot electron based photovoltaic device that make use of surface plasmons to enhance the optical absorption and hot electron generation. Although more than an order of magnitude enhancement was shown at the resonance wavelength of the plasmonic structure, several studies suggest that even further enhancement is possible. Several groups have already studied the use of MIM structures as broad-band absorbers [26, 27, 28]. An MIM stack that has around 94% average absorption in the visible wavelength range (400-750 nm) was demonstrated with Au-SiO_2-Au layers by Nielsen *et al.* They have shown that in an MIM configuration the absorption in Au layers could be made so high that a "black gold" could be obtained [27]. Incorporation of such an approach to MIM hot electron based photovoltaic devices could result in tremendous increase in device efficiency. Still the problem would be quite different for MIM photovoltaic device compared to a

conventional broad-band absorber. Rather than maximizing the overall absorption in the whole MIM structure, a photovoltaic device would require maximizing the absorption in one of the metal layers compared to the other metal layer. This problem was partly addressed by Wadell *et al.* in their absorption engineering study with a nanodisc of Au-SiO_2-Pd stack [28]. Instead of achieving very strong plasmonic resonances in an MIM device with Au metal layers, they replace one of the metal layers with Pd, which has more optical loss than Au. This approach makes a trade-off between strength of the plasmonic resonance and loss of the resonator, which allows engineering of the absorption in the MIM stack. From another point of view, Au nanodisc acts as a plasmonic nanoantenna and transfers the optical power to Pd nanodisc. Surface plasmons decay into hot electrons that can be used for photovoltaic or photocatalytic activity [28]. Using a similar approach for MIM based hot electron photovoltaic devices is also possible. A metal layer with high loss and a metal nanostructure that can excite plasmonic resonances can be used together in a device structure similar to the one investigated in Chapter 5. Plasmon excitation structure and tunneling junction can be separately optimized in such a device configuration, which allows flexible device design.

6.2 Simulation Setup

We performed finite-difference time-domain (FDTD) simulations of this structure using FDTD Solutions by Lumerical Inc. We used the data reported in the literature for the dielectric properties of gold, silver, chromium, aluminum and alumina [70]. A 2-D simulation environment is used to study the optical absorption in the MIMIM structures when illuminated with normally incident light from the top. We investigated the absorption spectrum of the flat metal layer with and without nanoantennas. We use periodic boundary conditions for the x-axis and set the period as 500 nm. Perfect electric conductor (PEC) boundary conditions are used as the top and bottom boundaries (y-axis). We use flat Al layer as the bottom metal. The bottom metal extends 100 nm above the bottom boundary, which is enough to assume the bottom metal to be infinitely thick for the

wavelength range of interest. There is 4-nm-thick insulator (Al_2O_3) layer on the bottom metal. Thickness of this insulator layer is tightly limited by the tunneling probability considerations, and should approximately be in the 4-8 nm range [76]. A 40-nm-thick metal layer (top metal) is on this thin insulator layer, and the optical absorption in this flat metal layer will result in photovoltaic action. There is a relatively thick (40-80 nm) Al_2O_3 layer (top insulator) on this absorbing metal layer, and there are metal nanoantennas on the insulator layer. Both Au and Ag nanoantennas are considered in the simulations. Device structure can be summarized from bottom to top as follows:

1. Bottom metal layer: Al layer thicker than 100 nm
2. Bottom insulator layer: 4 nm Al_2O_3
3. Top metal layer: 40 nm Au, Cr, Al or Ag
4. Top insulator layer: 40 or 80 nm Al_2O_3
5. Metal nanoantenna: Periodically distributed Au or Ag nanoantennas

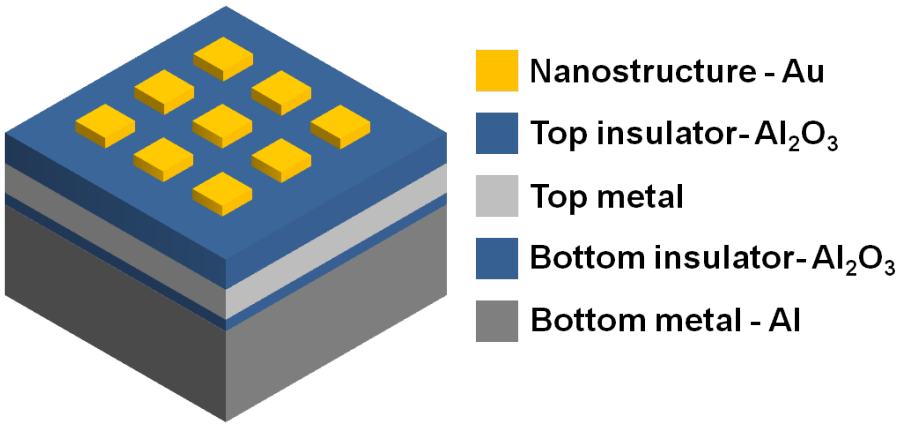

Figure 6.1: Schematic drawing of the double MIM structure. The bottom metal, the bottom insulator and the top metal layers form the bottom MIM, which will act as a diode in the actual device operation. The top metal, the top insulator and the nanostructure form the top MIM, which is used to excite surface plasmon modes.

Al is used as the bottom metal due to its high reflectivity at the visible wavelengths and its relatively high conductivity. High reflectivity and low optical loss

would be desired to minimize the optical absorption in this layer and to reflect any light reaching this layer back to the top metal. High conductivity is desired to provide good electrical contact to the MIM device. Choice of Al as the bottom metal for the simulations is also due to other practical limitations. Very thin dielectric layers can be deposited on Al, which is essential for obtaining a good tunneling junction. Au or Ag seem to have better electrical and optical properties compared to Al, but depositing a sufficiently thin dielectric layer with precise control of the thickness is very challenging on these metals. Another important problem with using Au or Ag is the electrical shorting of the top and bottom metals of the MIM structure since the insulator layer is very thin (less than 4 nm) and generally does not form a perfect continuous layer when deposited on these metals.

The insulator layer should be thin enough to allow electron tunneling at very low built-in voltages that will form between the two contacts of the MIM device under solar illumination. Our experiments showed that insulator layers up to 8-10 nm thickness can allow electron tunneling under voltage bias without any breakdown but the current levels are too low for practical photovoltaic applications. For this reason, we considered 4-nm-thick insulator layer in the simulations but thinner layers down to 1.5-2 nm would perform better in the experiments [37].

A fixed top metal thickness of 40 nm is used in the simulations. Important design considerations are the resistance of this layer, which should be low for good electrical contact to the MIM junction, and the optical absorption profile in this top metal layer. Most of the absorption occurs in about top 10 nm region of this layer so using a too thick metal layer would result in hot electron generation far away from the tunneling junction and the hot electrons would lose their excess energy until they reach the junction. A layer thinner than 10 nm, on the other hand, would allow optical field penetration to the bottom metal layer and hot electrons generated at the bottom metal layer would result in a reverse current flow in the MIM device that competes with the actual current flow. A layer with 40 nm thickness is chosen to avoid these problems as much as possible.

We choose to use 40 nm and 80 nm thick top insulator layers to investigate the effect of top insulator thickness on the surface plasmon modes. The thickness of this layer affects the strength of the interaction of the flat metal layer with the nanostructure. The coupling efficiency of the localized surface plasmon resonances (LSPRs) excited at the nanostructure to the surface plasmon polariton (SPP) modes at metal-dielectric interfaces can be controlled with the thickness of this insulating layer.

The simulated structure is shown in Fig.6.2. Different top insulator thicknesses and different nanoantenna dimensions are used and the optical absorption in the top metal is monitored. Au, Ag, Al and Cr are used as the top metal and the effect of using different metals is investigated. Nanoantenna thickness is chosen to be 30, 50, 80 and 100 nm. Simulated nanoantenna widths are 60, 80, 100 and 120 nm.

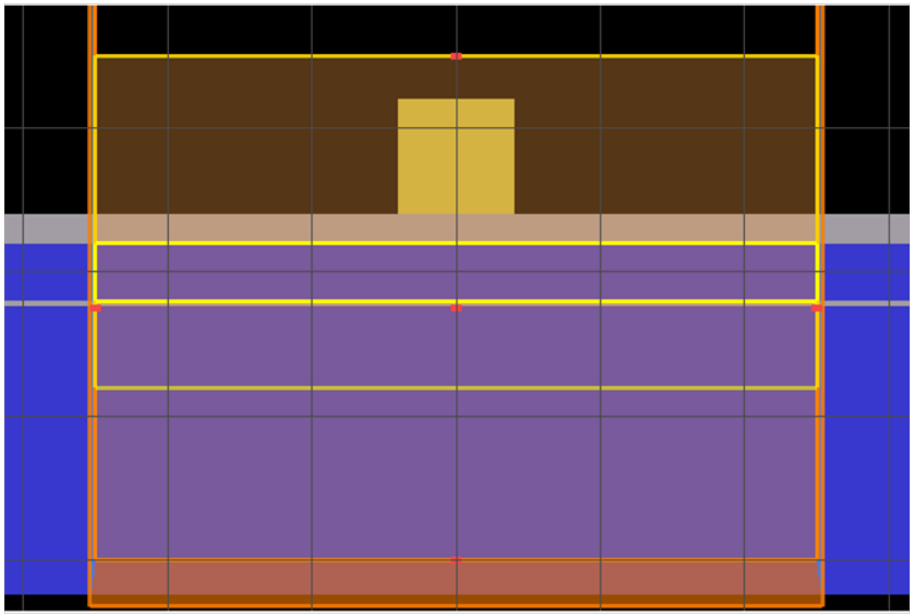

Figure 6.2: Simulation environment, depicting a unit cell of the double MIM stack. A light source illuminates the double MIM stack from the top with direct incidence. Perfectly matched layer (PML) boundary conditions are used for the top and bottom boundaries (z-axis) and periodic boundary conditions are used for x and y axis. An absorption monitor covering the whole volume of the top metal is used to calculate the absorption spectrum.

Name	Top Metal	Nanoantenna	Top Insulator
Fig. 6.3	Au	Ag	40 nm
Fig. 6.4	Au	Ag	80 nm
Fig. 6.5	Au	Au	40 nm
Fig. 6.6	Au	Au	80 nm
Fig. 6.8	Cr	Ag	40 nm
Fig. 6.9	Cr	Ag	80 nm
Fig. 6.10	Cr	Au	40 nm
Fig. 6.11	Cr	Au	80 nm
Fig. 6.12	Al	Ag	40 nm
Fig. 6.13	Al	Ag	80 nm
Fig. 6.14	Al	Au	40 nm
Fig. 6.15	Al	Au	80 nm
Fig. 6.16	Ag	Ag	40 nm
Fig. 6.17	Ag	Ag	80 nm
Fig. 6.18	Ag	Au	40 nm
Fig. 6.19	Ag	Au	80 nm

Table 6.1: The structural parameters of the simulated double MIM devices in each figure. The material of the top metal, the material of the nanoantenna and the thickness of the top insulator are given for each figure.

6.3 Simulation Results

Simulation results for different top metal types (Au, Cr, Al and Ag) are presented in the following subsections. For each type of top metal, the effect of the dimensions and the material of the nanoantenna and the thickness of the top insulator layer are investigated. Table 6.1 shows the parameters used for each figure. The discussion in the following subsections refers to the figures listed in Table 6.1.

6.3.1 Au Top Metal

Au has high absorption for the wavelengths shorter than 500 nm ($\lambda < 500$ nm) and when a 40-nm-thick top insulator layer is used, Au can absorb more than 90% of the incident light at these wavelengths (Fig 6.3 and Fig 6.5). For the dimensions simulated in this study, nanoantennas absorb and reflect the incoming

light, reducing the absorption in Au metal layer. Au nanoantennas can still be used to excite surface plasmons at longer wavelengths ($\lambda > 700$ nm). With sharp and strong plasmonic resonances, more than 50% of the incident light can be absorbed at the resonance wavelengths (Fig 6.4 and Fig 6.6). For all cases, using the smallest nanoantenna thickness (30 nm) seems to give stronger resonances but even with the thicker nanoantennas results are quite similar and no significant effect of changing the nanoantenna thickness is observed.

For the excitation of surface plasmons at NIR wavelengths, using Au and Ag nanoantennas on Au metal have similar effects. When the top insulator thickness is 80 nm, there is a sharp, strong plasmonic resonance peak centered at around 780 nm wavelength for an Ag nanoantenna with 60 nm width (Fig 6.4). This resonance gets broader and red-shifts as the width of the nanoantenna increases. When the insulator thickness is 40 nm and the nanoantenna width is 60 nm, the plasmonic resonance is centered at 700 nm and much weaker than the one observed with 80-nm-thick insulator. The resonance gets weaker and red-shifts as the nanoantenna width increases, and the amount of red-shift is larger than what is observed with 80-nm-thick insulator (Fig 6.3).

At the visible wavelengths, Au nanoantennas excite red-shifted and slightly weaker surface plasmons compared to Ag nanoantennas. The resonance wavelength is approximately 570 nm but the absorption of bare Au layer at shorter wavelengths seems to be higher than what can be achieved with surface plasmon decay.

Top insulator layer acts as an anti-reflective coating on the MIM device. Using 40-nm-thick top insulator layer gives enhanced absorption at wavelengths shorter than 500 nm. Using thicker top insulator can only slightly increase the absorption at NIR wavelengths since the absorption of Au at these wavelengths is very weak. Thickness of the top insulator layer also affects the ability of the MIM structure to support plasmonic resonances. The center frequency, the strength and the width of the resonances are strongly dependent on the top insulator thickness.

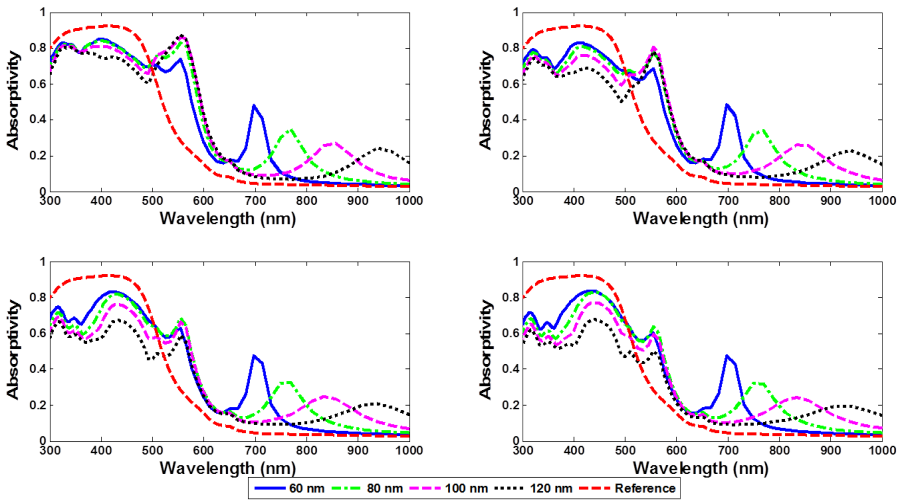

Figure 6.3: Absorptivity spectrum of the Au top metal layer of the MIMIM structure with 40-nm-thick top insulator and Ag nanoantenna. Simulated nanoantenna thicknesses are (a) 30 nm, (b) 50 nm, (c) 80 nm and (d) 100 nm. Different plots in each figure correspond to the reference structure and nanoantenna widths of 60 nm, 80 nm, 100 nm and 120 nm.

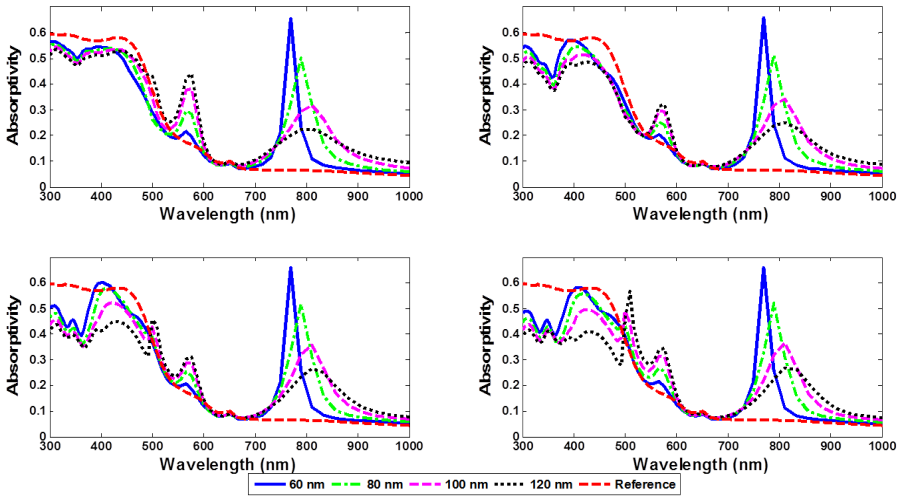

Figure 6.4: Absorptivity spectrum of the Au top metal layer of the MIMIM structure with 80-nm-thick top insulator and Ag nanoantenna. Simulated nanoantenna thicknesses are (a) 30 nm, (b) 50 nm, (c) 80 nm and (d) 100 nm. Different plots in each figure correspond to the reference structure and nanoantenna widths of 60 nm, 80 nm, 100 nm and 120 nm.

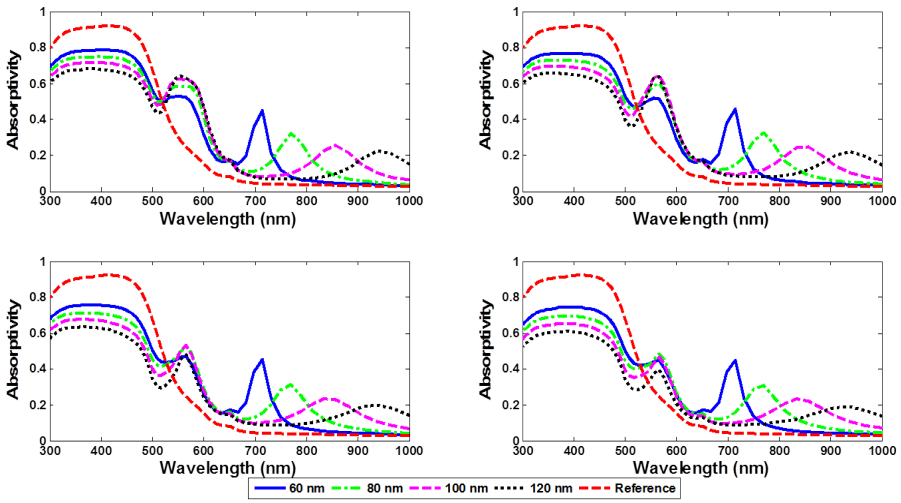

Figure 6.5: Absorptivity spectrum of the Au top metal layer of the MIMIM structure with 40-nm-thick top insulator and Au nanoantenna. Simulated nanoantenna thicknesses are (a) 30 nm, (b) 50 nm, (c) 80 nm and (d) 100 nm. Different plots in each figure correspond to the reference structure and nanoantenna widths of 60 nm, 80 nm, 100 nm and 120 nm.

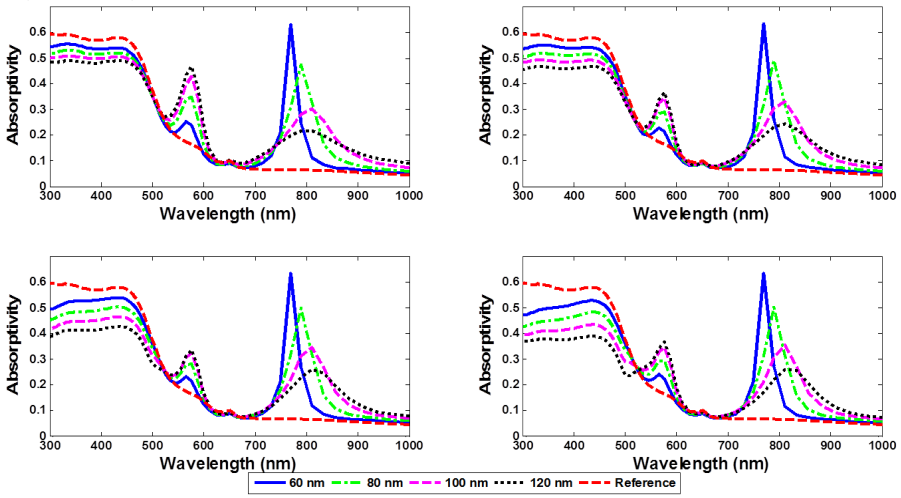

Figure 6.6: Absorptivity spectrum of the Au top metal layer of the MIMIM structure with 80-nm-thick top insulator and Au nanoantenna. Simulated nanoantenna thicknesses are (a) 30 nm, (b) 50 nm, (c) 80 nm and (d) 100 nm. Different plots in each figure correspond to the reference structure and nanoantenna widths of 60 nm, 80 nm, 100 nm and 120 nm.

6.3.2 Cr Top Metal

Among the simulated metal types, Cr has the best absorptive properties. Al-Al_2O_3-Cr structure cannot support very strong plasmonic resonances, but high absorption in Cr would make this structure one of the best candidates for MIM hot electron based photovoltaic device, if not for small conductivity and short hot electron attenuation length of Cr. Even without the nanoantennas Cr layer can exhibit more than 50% absorption in the wavelength range of interest and nanoantennas can further improve the absorption, especially at NIR wavelengths. Plasmonic resonances can have more than 100 nm full-width half maximum (FWHM), mostly due to the high optical loss of Cr, but such broad resonances are especially preferred for photovoltaic applications. More than 90% absorptivity at the resonance wavelength of the structure could be achieved in the simulations.

An important property of this double MIM structure, predominantly observed in the simulations with Cr top metal, is the anti-reflective behavior of the top insulator. Increasing the thickness of the top insulator red-shifts and broadens the absorption spectrum of Cr (Fig. 6.7).

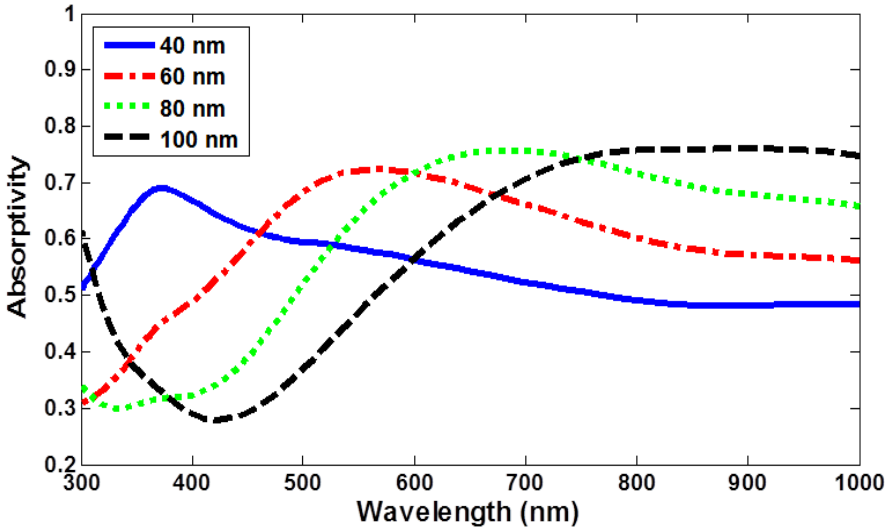

Figure 6.7: Absorptivity in the top metal (Cr) layer of Al-Al_2O_3-Cr-Al_2O_3 (MIM) device. Increasing the top insulator thickness red-shifts the absorptivity spectrum.

When the insulator thickness is 80 nm and the Ag nanoantenna thickness is small (t = 30 nm), the double MIM structure supports surface plasmons whose resonance is centered at a wavelength of 720 nm (Fig. 6.8). When thicker nanoantennas are used, the resonance frequency slightly red-shifts with increasing nanoantenna width. When the insulator thickness is 40 nm, the resonance frequency of the surface plasmons are more strongly dependent on the nanoantenna width and the center frequency can be shifted from 650 nm to 900 nm by changing the nanoantenna width from 60 nm to 120 nm. No significant change of this surface plasmon mode is observed when Ag nanoantennas are used instead of Au nanoantennas. The first plasmon mode, which is centered at around 540 nm wavelength for Ag nanoantennas and 40-nm-thick top insulator, red-shifts to 560 nm for Au nanoantennas, and disappears when 80-nm-thick top insulator is used. The strength of this plasmon mode also diminishes with increasing nanoantenna thickness.

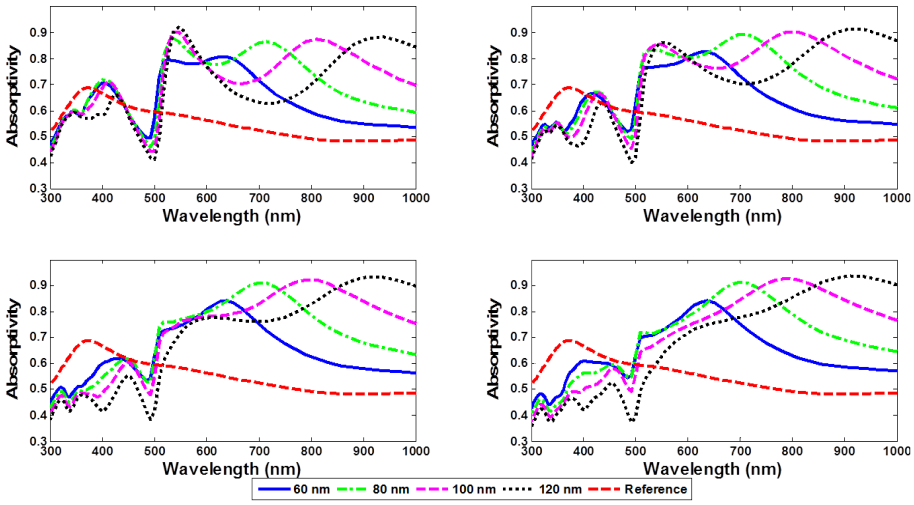

Figure 6.8: Absorptivity spectrum of the Cr top metal layer of the MIMIM structure with 40-nm-thick top insulator and Ag nanoantenna. Simulated nanoantenna thicknesses are (a) 30 nm, (b) 50 nm, (c) 80 nm and (d) 100 nm. Different plots in each figure correspond to the reference structure and nanoantenna widths of 60 nm, 80 nm, 100 nm and 120 nm.

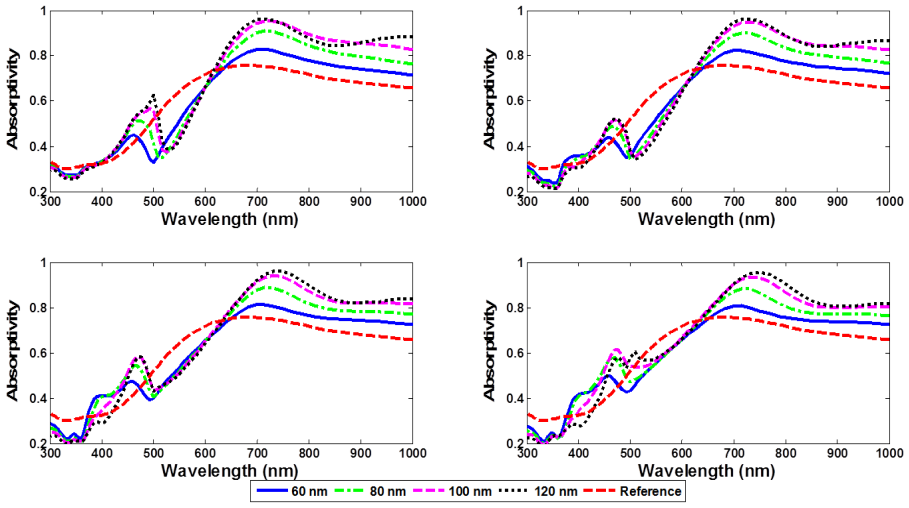

Figure 6.9: Absorptivity spectrum of the Cr top metal layer of the MIMIM structure with 80-nm-thick top insulator and Ag nanoantenna. Simulated nanoantenna thicknesses are (a) 30 nm, (b) 50 nm, (c) 80 nm and (d) 100 nm. Different plots in each figure correspond to the reference structure and nanoantenna widths of 60 nm, 80 nm, 100 nm and 120 nm.

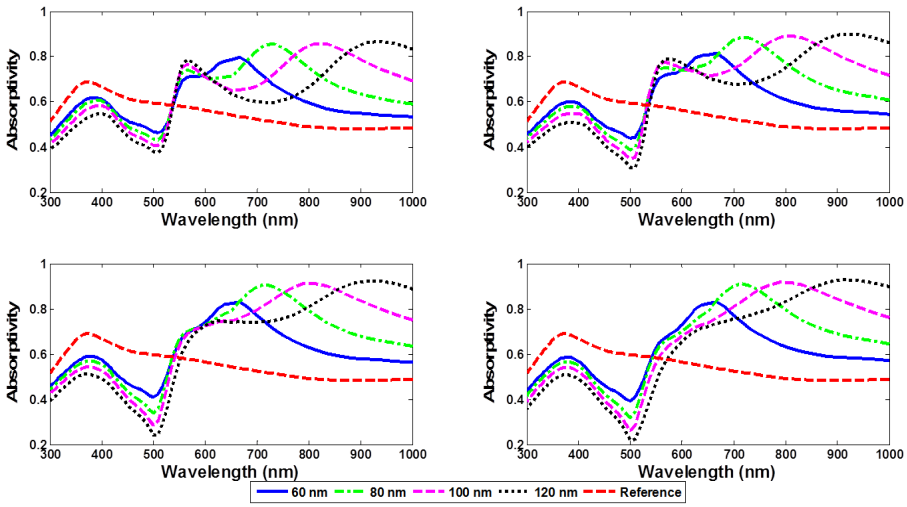

Figure 6.10: Absorptivity spectrum of the Cr top metal layer of the MIMIM structure with 40-nm-thick top insulator and Au nanoantenna. Simulated nanoantenna thicknesses are (a) 30 nm, (b) 50 nm, (c) 80 nm and (d) 100 nm. Different plots in each figure correspond to the reference structure and nanoantenna widths of 60 nm, 80 nm, 100 nm and 120 nm.

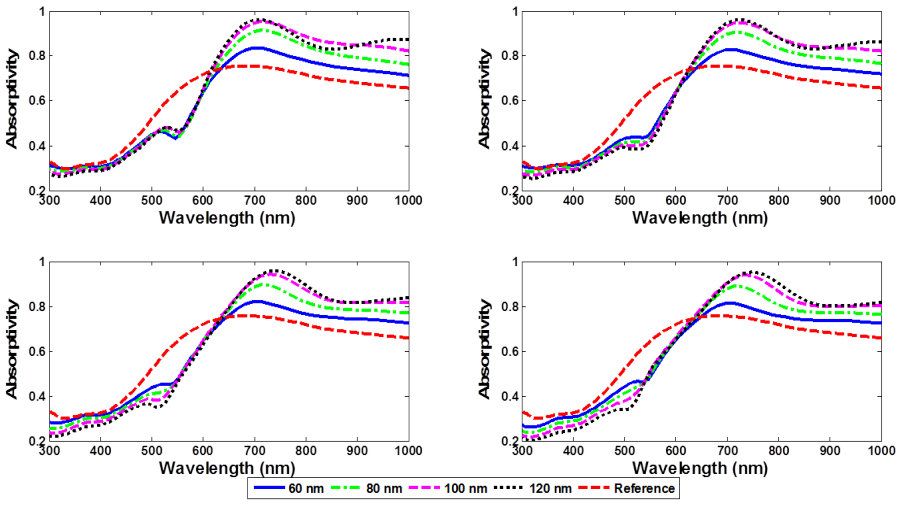

Figure 6.11: Absorptivity spectrum of the Cr top metal layer of the MIMIM structure with 80-nm-thick top insulator and Au nanoantenna. Simulated nanoantenna thicknesses are (a) 30 nm, (b) 50 nm, (c) 80 nm and (d) 100 nm. Different plots in each figure correspond to the reference structure and nanoantenna widths of 60 nm, 80 nm, 100 nm and 120 nm.

6.3.3 Al Top Metal

For the wavelength range of interest, Al is a good reflector and its refractive index makes it suitable for surface plasmon propagation. Plasmonic resonances are strong and broad (more than 100 nm FWHM). Up to 80% absorption can be achieved at the resonance wavelengths.

When the top insulator thickness is 40 nm, there are strong plasmonic resonances in the NIR wavelengths and the center frequency of the resonance strongly depends on the width of the nanoantenna. By changing the width of the nanoantennas from 60 nm to 120 nm the resonance peak can be moved from 640 nm to 880 nm. Very high absorptivity values could be obtained due to strong plasmonic resonances and the wavelength of the resonance can be adjusted in a wide wavelength range, which makes this choice of device structure very suitable for NIR photodetection or photovoltaic applications. Nanoantennas with different widths could possibly be used together on the same device to achieve broad-band absorption enhancement. The resonance peak of this structure also blue-shifts about 20 nm when Ag nanoantennas are used instead of Au nanoantennas.

When the top insulator thickness is 80 nm, there is a strong resonance peak at NIR wavelengths, at around 720 nm wavelength. There is also a small resonance peak at visible wavelengths, at around 480 nm wavelength, when Ag nanoantennas are used. The center frequency and the strength of the resonance can be very slightly tuned with nanoantenna dimensions. This peak at visible wavelengths does not appear in the simulations when Au nanoantennas are used.

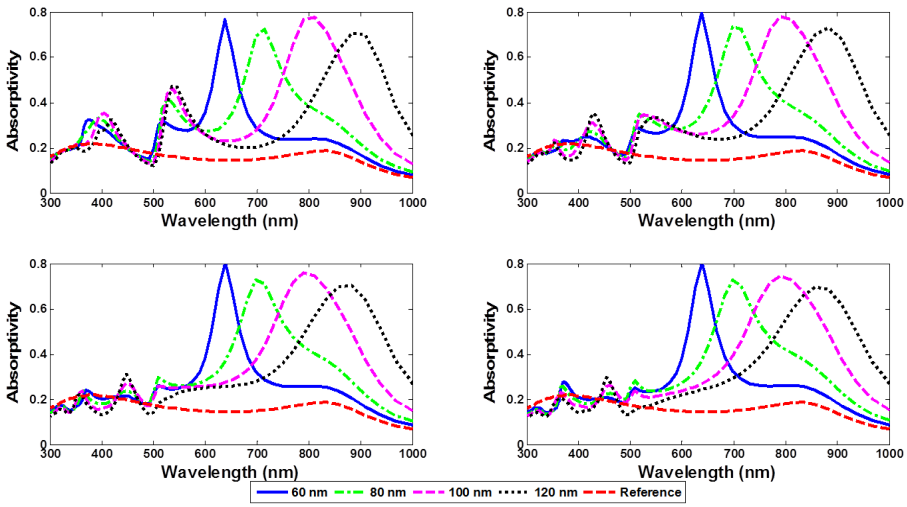

Figure 6.12: Absorptivity spectrum of the Al top metal layer of the MIMIM structure with 40-nm-thick top insulator and Ag nanoantenna. Simulated nanoantenna thicknesses are (a) 30 nm, (b) 50 nm, (c) 80 nm and (d) 100 nm. Different plots in each figure correspond to the reference structure and nanoantenna widths of 60 nm, 80 nm, 100 nm and 120 nm.

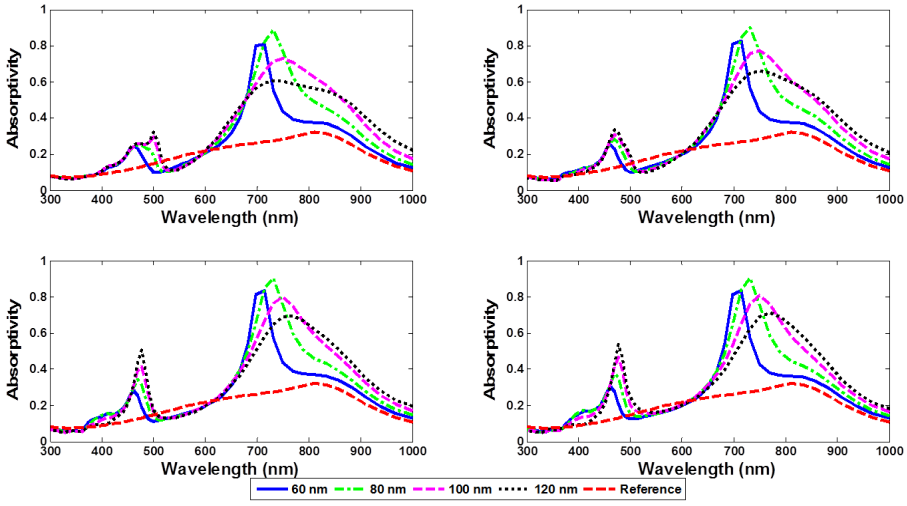

Figure 6.13: Absorptivity spectrum of the Al top metal layer of the MIMIM structure with 80-nm-thick top insulator and Ag nanoantenna. Simulated nanoantenna thicknesses are (a) 30 nm, (b) 50 nm, (c) 80 nm and (d) 100 nm. Different plots in each figure correspond to the reference structure and nanoantenna widths of 60 nm, 80 nm, 100 nm and 120 nm.

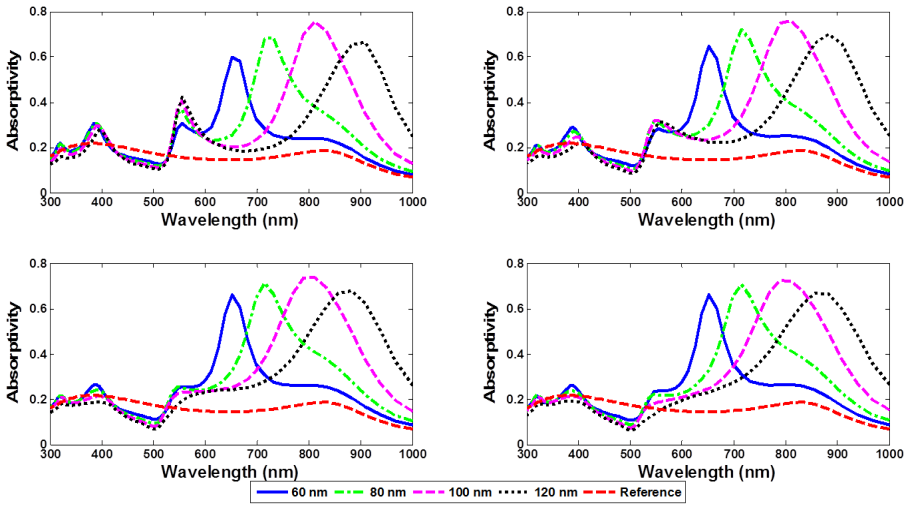

Figure 6.14: Absorptivity spectrum of the Al top metal layer of the MIMIM structure with 40-nm-thick top insulator and Au nanoantenna. Simulated nanoantenna thicknesses are (a) 30 nm, (b) 50 nm, (c) 80 nm and (d) 100 nm. Different plots in each figure correspond to the reference structure and nanoantenna widths of 60 nm, 80 nm, 100 nm and 120 nm.

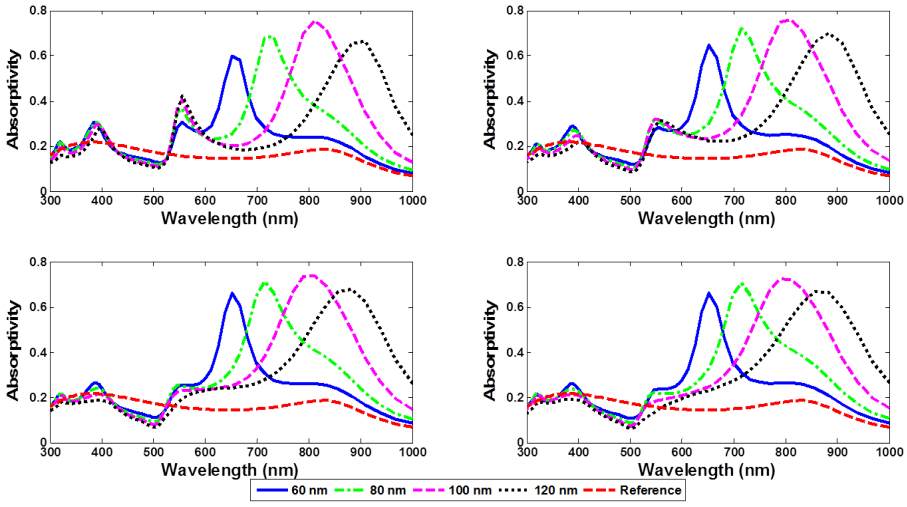

Figure 6.15: Absorptivity spectrum of the Al top metal layer of the MIMIM structure with 80-nm-thick top insulator and Au nanoantenna. Simulated nanoantenna thicknesses are (a) 30 nm, (b) 50 nm, (c) 80 nm and (d) 100 nm. Different plots in each figure correspond to the reference structure and nanoantenna widths of 60 nm, 80 nm, 100 nm and 120 nm.

6.3.4 Ag Top Metal

Ag reflects most of the light for these wavelengths, and the resonator formed between the Ag layer and the nanoantenna has very little loss. Despite the high reflection from the Ag layer, strong confinement of the field can give high absorption values for the resonance wavelengths. When Ag nanoantenna is used, symmetric nature of the top MIM resonator results in very strong and sharp resonances. Resonance peaks with less than 50 nm FWHM can be observed when the insulator thickness is 80 nm. At the visible wavelengths the resonances are sharper and stronger for Ag nanoantennas, and the strength of the resonance increases with nanoantenna width. At the NIR wavelengths, on the other hand, the strength of the resonance decreases as the nanoantenna width increases. Au nanoantennas give very similar results to Ag nanoantennas at the NIR wavelengths but the plasmonic resonances at the visible wavelengths are much weaker.

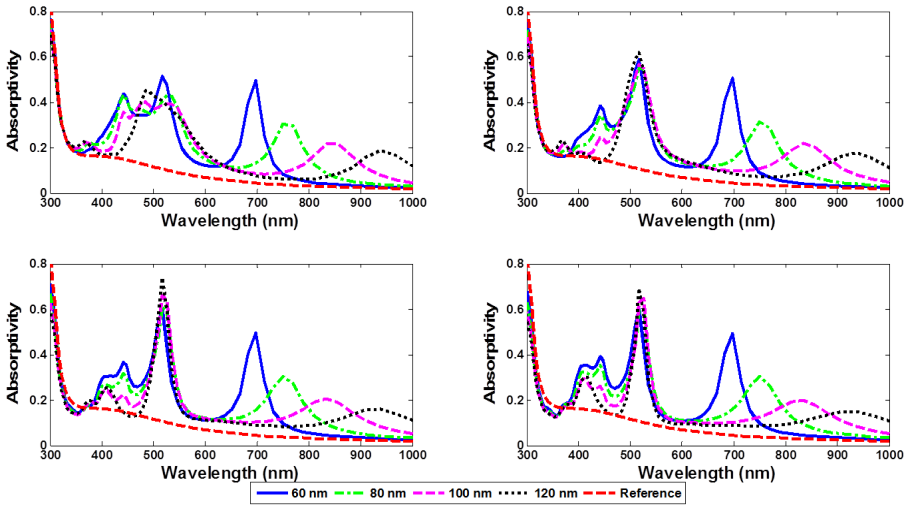

Figure 6.16: Absorptivity spectrum of the Ag top metal layer of the MIMIM structure with 40-nm-thick top insulator and Ag nanoantenna. Simulated nanoantenna thicknesses are (a) 30 nm, (b) 50 nm, (c) 80 nm and (d) 100 nm. Different plots in each figure correspond to the reference structure and nanoantenna widths of 60 nm, 80 nm, 100 nm and 120 nm.

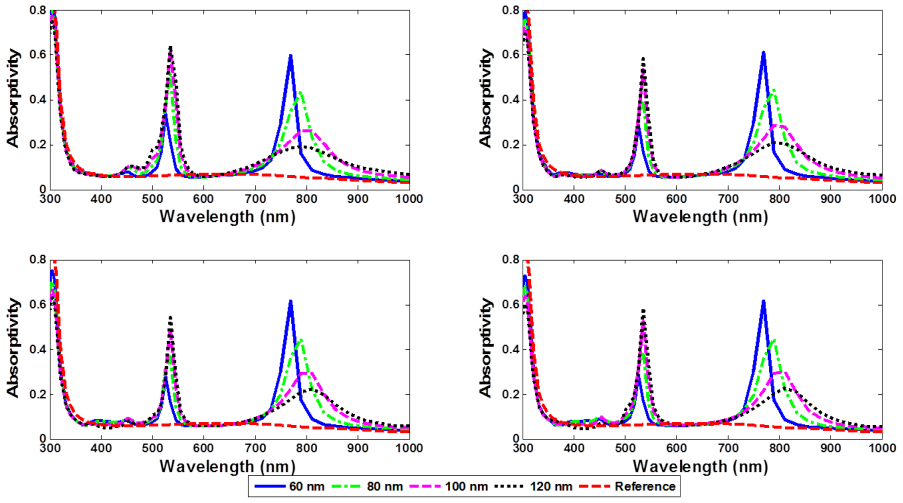

Figure 6.17: Absorptivity spectrum of the Ag top metal layer of the MIMIM structure with 80-nm-thick top insulator and Ag nanoantenna. Simulated nanoantenna thicknesses are (a) 30 nm, (b) 50 nm, (c) 80 nm and (d) 100 nm. Different plots in each figure correspond to the reference structure and nanoantenna widths of 60 nm, 80 nm, 100 nm and 120 nm.

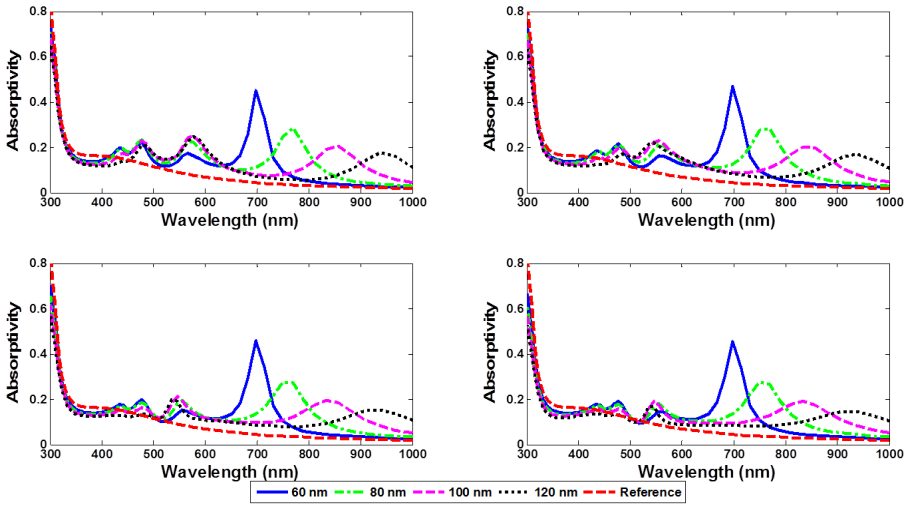

Figure 6.18: Absorptivity spectrum of the Ag top metal layer of the MIMIM structure with 40-nm-thick top insulator and Au nanoantenna. Simulated nanoantenna thicknesses are (a) 30 nm, (b) 50 nm, (c) 80 nm and (d) 100 nm. Different plots in each figure correspond to the reference structure and nanoantenna widths of 60 nm, 80 nm, 100 nm and 120 nm.

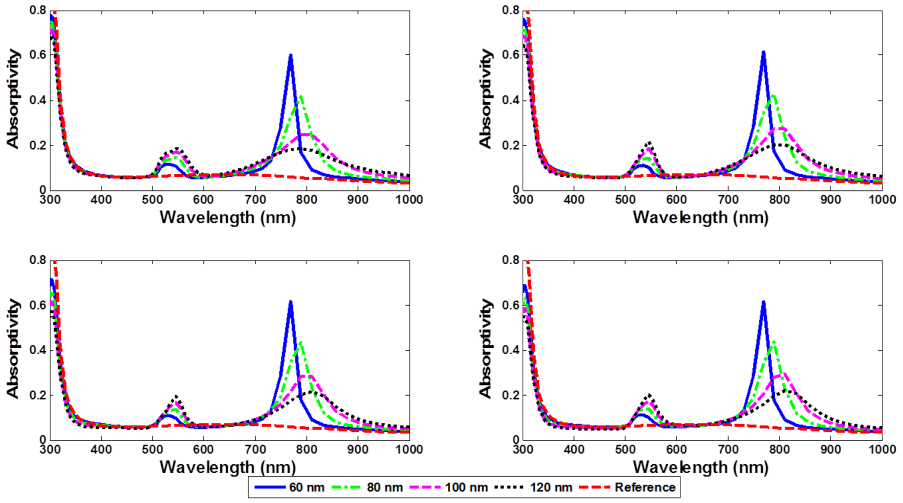

Figure 6.19: Absorptivity spectrum of the Ag top metal layer of the MIMIM structure with 80-nm-thick top insulator and Au nanoantenna. Simulated nanoantenna thicknesses are (a) 30 nm, (b) 50 nm, (c) 80 nm and (d) 100 nm. Different plots in each figure correspond to the reference structure and nanoantenna widths of 60 nm, 80 nm, 100 nm and 120 nm.

6.4 Surface Plasmon Modes in Double MIM Structure

Interaction of the metal nanoantenna with the underlying top metal layer results in the excitation of two distinct surface plasmon modes that could be observed in most of the absorption spectra of the previous subsection. One of these surface plasmon modes gives resonance between 500 nm - 600 nm wavelength range and the resonance wavelength does not very strongly depend on the nanoantenna dimensions. The other surface plasmon mode has resonance at longer wavelengths and the resonance wavelength can be tuned between 650 nm and 1000 nm by changing the dimensions of the nanoantenna.

The occurrence of two such surface plasmon modes was explained with the plasmon hybridization model [78, 82, 83]. Coupling between the localized surface plasmon resonances (LSPRs) of two metal nanostructures results in the splitting of the surface plasmon mode. For nanostructures standing next to each other on a substrate, the lower energy mode occurs due to the "bonding" interaction of LSPRs. This lower energy mode can be excited under normally incident light and is called the "bright" surface plasmon mode (Fig. 6.20(a)). The "antibonding" mode has higher energy but can not be excited in such a configuration, hence it is called the "dark" surface plasmon mode (Fig. 6.20(b)). On the other hand when a metal nanostructure is on top of the other one with an insulating spacer layer in between, similar to an MIM configuration, both the bright and the dark modes can be excited under normally incident light due to the phase delay introduced by the insulator layer (Fig. 6.20(c) and Fig. 6.20(d)). However, in this MIM configuration, the bonding mode corresponds to the lower energy, dark plasmon mode, and the antibonding mode corresponds to the higher energy, bright plasmon mode [78].

We calculate the electric field profiles (|E|) of the double MIM structure at the resonance wavelengths of the bright and dark plasmon modes by using FDTD simulations. For this analysis we use the MIM structure with Au top metal, 40-nm-thick top insulator and Au nanoantenna. The absorption spectra in the

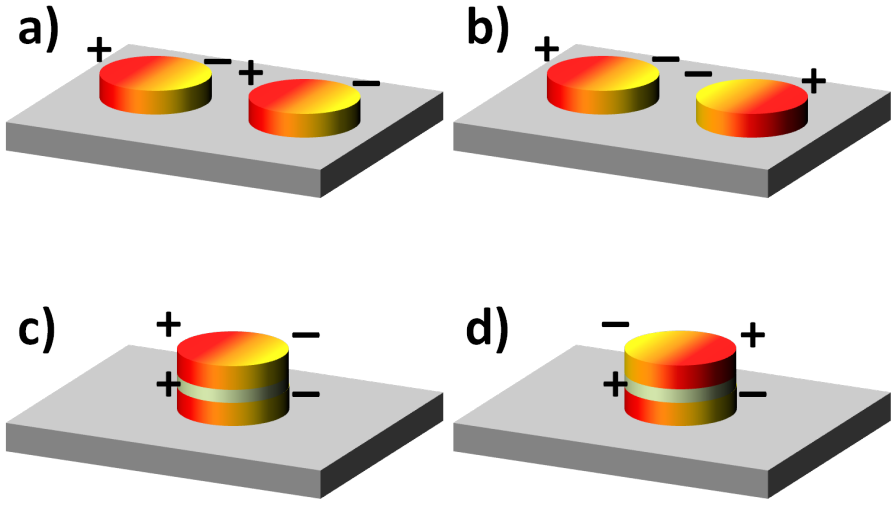

Figure 6.20: Bonding (a) and antibonding (b) interaction between two metal nanostructures standing next to each other on a substrate. The bonding mode can be excited with normal incidence and is called the bright mode. The antibonding mode can not be excited in this configuration and is called the dark mode. The MIM configuration allows the excitation of both the antibonding (c) and bonding (d) modes under normally incident light.

top metal layer of this structure were shown in Fig. 6.5. The thickness of the nanoantenna is 50 nm and the width of the nanoantenna is 100 nm. The bright plasmon resonance occurs at 550 nm wavelength (Fig. 6.21) and the dark plasmon resonance occurs at 840 nm wavelength (Fig. 6.22).

The electric field (|E|) distribution at 550 nm wavelength is mostly concentrated around the Au nanostructure as expected from the strong scattering nature of the bright plasmon mode (Fig. 6.21). The electric field magnitude (|E|) profile indicates that the surface plasmon mode at this frequency is the antibonding mode [78]. This antibonding behavior can also be confirmed by investigating the electric field vector profile or the charge distribution analysis. The same approach can also be applied to the electric field (|E|) profile at 840 nm wavelength (Fig. 6.22) to discover that the surface plasmon resonance arises from the bonding interaction. The electric field is mostly confined between the top metal layer and the metal nanoantenna. The surface plasmon energy decays quickly in this mode. The absorption is much more dominant compared to the scattering, hence the name dark plasmon [78].

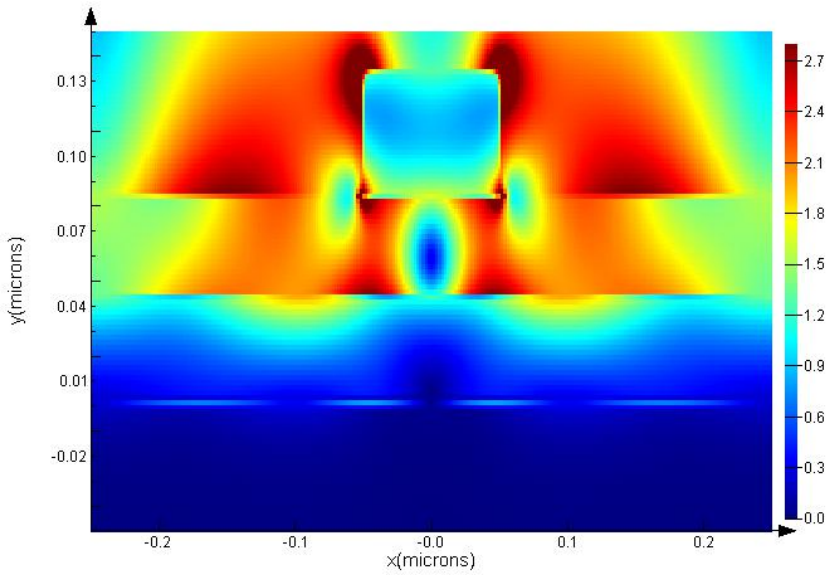

Figure 6.21: Simulated electric field profile of the double MIM structure at 550 nm wavelength for the same device configuration as Fig. 6.5. The thickness of the nanoantenna is 50 nm and the width of the nanoantenna is 100 nm. Electric field is mostly concentrated around the Au nanoantenna, outside the MIM structure, which indicates the strong scattering of the bright plasmon mode.

Originally, the absorptivity of the Au layer at 840 nm wavelength is very small and this behavior was also confirmed by the FDTD simulation results of the reference devices in the previous subsection (Fig. 6.3 - Fig. 6.6). However, the strong field confinement and high absorption of the dark plasmon mode yield more than 20% absorptivity at this wavelength. The resonance wavelength of the dark plasmon mode can be tuned in a broad range (650 nm - 1000 nm) by changing the thickness of the insulator layer or the width of the nanoantenna. The bright plasmon resonance, on the other hand, can be shifted very little (less than 30 nm) by changing the thickness of the insulator layer or the width of the nanoantenna. Unlike the dark mode, the higher energy bright mode is dominated by scattering rather than absorption. The absorptivity can be enhanced by about 3 times compared to the reference structure.

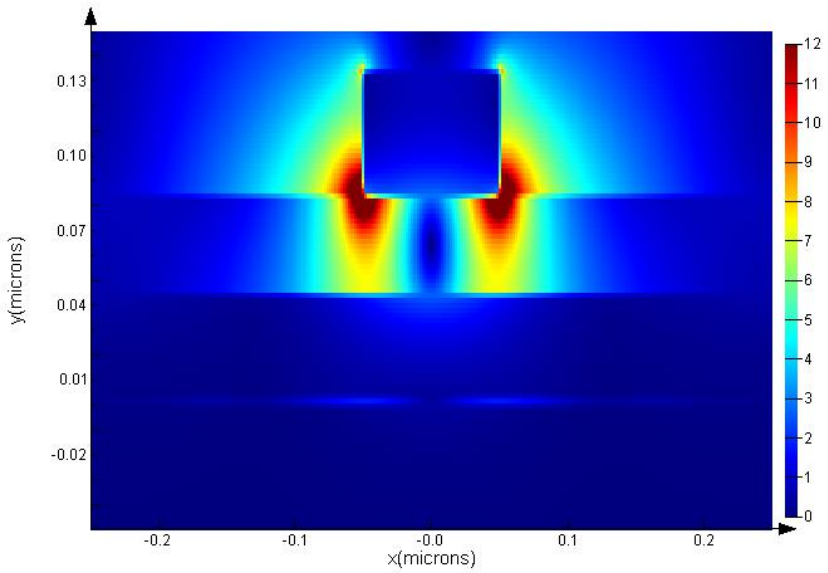

Figure 6.22: Simulated electric field profile of the double MIM structure at 840 nm wavelength for the same device configuration as Fig. 6.5. The thickness of the nanoantenna is 50 nm and the width of the nanoantenna is 100 nm. Electric field is strongly confined below the Au nanoantenna, within the MIM structure, which indicates the strongly absorptive behavior of the dark plasmon mode.

6.5 Conclusion

FDTD simulations of the double MIM structure are performed and surface plasmon excitation and decay mechanisms of this structure are investigated. Absorptivity of the top metal layer is monitored in the simulations, which essentially corresponds to the hot electron generation rate in the metallic absorber upon illumination. Using Au nanoantennas gives very similar results to Ag nanoantennas for most cases with only a slight red-shift. The effect of using different types of top metal layers is also investigated. Au and Ag layers can support strong and sharp plasmonic resonances but the achieved absorptivity values are not high for most of the spectrum due to the small optical loss in these materials. Cr can not support surface plasmon resonances and the LSPRs excited at the nanoantenna decay rapidly in the Cr layer due to the high optical loss of this material. This high loss results in broad-band enhancement of the already high absorptivity of the Cr layer and would make this device a good candidate for hot electron based

photovoltaic applications. However, the low conductivity of Cr and the small mean free path of hot electrons in Cr are likely to degrade the device efficiency significantly. Using Al as the top metal seems to be a viable option for most device applications at NIR wavelengths. Very strong and broad-band plasmonic resonances can be excited and more than 80% absorptivity values can be achieved.

Splitting of the surface plasmon mode is observed clearly in the investigated absorption spectra of almost all device configurations. Due to the bonding and antibonding interaction, the surface plasmon modes split into a high energy bright mode and a lower energy dark mode. The bright mode is dominated by scattering whereas the dark mode is mostly absorptive. This effective separation of the scattering and absorptive surface plasmon modes is a distinct property of the MIM configuration and can be utilized in novel device applications. The dark plasmon resonance can be tuned over a broad range of wavelengths and this ability allows designing the MIM structure for specific applications. Broadband resonances can also be obtained by using several nanoantennas in a unit cell each having a different diameter or by simply using a random distribution of randomly sized nanoislands similar to the one in Chapter 4.

Chapter 7

Conclusion

We studied surface plasmon assisted hot electron generation for photodetection and photovoltaic applications. We made use of surface plasmon excitation on metal nanoparticles to confine the optical energy to metal layers and increase the optical absorption and hot electron generation in metals. Photogenerated hot electrons are collected at a Schottky junction over a potential barrier to generate photocurrent via the internal photoemission process. We discussed potential barrier formation, current generation and collection mechanisms and other electrical properties of Schottky junctions. Metal and semiconductor type, doping level of the semiconductor and the interface quality are the main considerations for the design of Schottky junctions.

For the excitation of surface plasmons, this study mostly focuses on the use of Au nanoparticles and Au nanoislands. The decay of both localized surface plasmon resonances (LSPRs) and the propagating surface plasmon polaritons (SPPs), which were triggered by LSPRs, were utilized to generate hot electrons. We reviewed the quasi-static approximation to solve the interaction of the electromagnetic field with a sub-wavelength nanoparticle and explained the LSPR excitation on metal nanoparticles. The main steps of plasmon assisted hot electron generation process are surface plasmon excitation on metal nanoparticles, the decay of surface plasmons to generate hot electrons, hot electron injection

from the metal nanoparticles and regeneration of the lost charge back to the nanoparticle. We also commented on the timescales of these steps and identified the charge regeneration step as the main bottleneck for this mechanism.

We investigated two different device configurations for plasmonically enhanced hot electron based photodetectors and photovoltaics. We demonstrated a near-infrared (NIR) photodetector monolithically fabricated on Si substrate. Sub-bandgap photodetection on silicon is achieved by the excitation of localized surface plasmon resonances (LSPRs) on Au nanoislands. The Au nanoislands are randomly distributed on Si substrate and are obtained by a simple and fast fabrication method. The decay of LSPRs on Au nanoislands results in the generation of hot electrons which are then injected into Si to generate photocurrent. Photoresponsivity values as high as 2 mA/W and 600 μA/W are measured at wavelengths of 1.3 μm and 1.55 μm, respectively. Finite-difference time-domain (FDTD) simulations are conducted by importing the scanning electron microscope (SEM) images of fabricated Au nanoislands in order to model the surface plasmon assisted hot electron generation mechanism for sub-bandgap photodetection on Si.

In our photodetectors, we have used atomic layer deposited AZO (aluminum doped zinc oxide) as a transparent conducting oxide (TCO) layer. This TCO layer makes electrical contact between Au nanoislands and it is also in contact with Si substrate. A thin (< 2 nm) interlayer dielectric layer would prove useful to prevent the contact of the Au nanoislands and TCO layer with the Si substrate and decrease the dark current. The interlayer dielectric layer would also passivate the interface states at the Au-Si junction and prevent the diffusion of the Au layer into Si substrate. Additionally, the properties of the electrical contact between the Au nanoislands and the TCO layer is crucial for fast device operation since the electron regeneration back to the Au nanoislands after the hot electron injection step is the slowest process for most cases.

We also demonstrated a hot electron based photovoltaic device in a double MIM configuration. Au nanoparticles randomly coated on a Au layer with an insulating spacer layer form one of the MIM junctions. This junction acts as

an optical antenna and couples the incident optical energy to the MIM device through the excitation of surface plasmons. The other MIM junction forms the tunneling diode, which collects the hot electrons generated by the decay of surface plasmons. Through the excitation of surface plasmons, more than an order of magnitude enhancement in photoresponsivity was recorded at the resonance wavelength of the surface plasmons.

A significant advantage of the double MIM architecture is the ability to separately design the electrical junction and the plasmon excitation structure. The hot electron collection efficiency at the MIM junction can be improved by decreasing the surface recombination at the metal-insulator interfaces and engineering the energy band structure of the MIM junction. An additional insulator or semiconductor layer can be incorporated into the MIM diode junction to increase the asymmetry of the diode and reduce the backflow of charge carriers. This device configuration enables such an MIM diode study without any significant change in the plasmon excitation structure. Similarly, various plasmon excitation structures and anti-reflection coatings can be fabricated on the MIM device without modifying the electrical properties. With this aim, we conducted finite-difference time-domain (FDTD) simulations of this double MIM structure to achieve high absorption in the absorber layer of the MIM structure and engineer the absorption spectrum. Double MIM devices with different metal types, nanoantenna dimensions and spacer layer thicknesses are simulated and the dependence of the excitation and decay of surface plasmons on these device parameters are investigated. FDTD simulation results indicate that broad-band absorbers for photovoltaics applications and narrow-band absorbers for photodetector applications can be designed.

With this double MIM device configuration, we have experimentally shown that the excitation of surface plasmons can significantly increase the device efficiency without altering the electrical junction. Our FDTD simulations have also showed that engineering the absorption spectrum and the spatial absorption profile is possible with this approach. Although, a significant amount of research is necessary to improve the electrical properties of MIM diodes and increase their efficiency as photovoltaic devices, the double MIM configuration proposed in this

study successfully addresses many key issues related to inherent optical properties of metals such as high reflection and low absorption. With careful design and process development, MIM structures can be fabricated as broad-band perfect absorbers on MIM diodes with the proposed device configuration.

Although reported efficiencies of hot electron based devices are not sufficiently high, large scale production compatibility and low cost have been a strong motivation for the development of hot electron based devices. This proof-of-concept study demonstrates the potential of exploiting surface plasmons for hot electron based photodetectors and photovoltaic devices. A better understanding of the mechanism of surface plasmon assisted hot electron generation on metals is likely to help the design of high efficiency devices. New device configurations, materials and fabrication methods can further improve the device performance and realize a new generation of solar cells and photodetectors.

Bibliography

[1] C. Clavero, "Plasmon-induced hot-electron generation at nanoparticle/metal-oxide interfaces for photovoltaic and photocatalytic devices," *Nature Photonics*, vol. 8, no. 2, pp. 95–103, 2014.

[2] G. Zhao, H. Kozuka, and T. Yoko, "Sol-gel preparation and photoelectrochemical properties of tio 2 films containing au and ag metal particles," *Thin Solid Films*, vol. 277, no. 1, pp. 147–154, 1996.

[3] G. Reich, "Near-infrared spectroscopy and imaging: basic principles and pharmaceutical applications," *Advanced drug delivery reviews*, vol. 57, no. 8, pp. 1109–1143, 2005.

[4] R. Raghavachari, *Near-infrared applications in biotechnology*. CRC Press, 2010.

[5] B. M. Onat, W. Huang, N. Masaun, M. Lange, M. H. Ettenberg, and C. Dries, "Ultra-low dark current ingaas technology for focal plane arrays for low-light level visible-shortwave infrared imaging," in *Defense and Security Symposium*, pp. 65420L–65420L, International Society for Optics and Photonics, 2007.

[6] M. MacDougal, A. Hood, J. Geske, J. Wang, F. Patel, D. Follman, J. Manzo, and J. Getty, "Ingaas focal plane arrays for low-light-level swir imaging," in *SPIE Defense, Security, and Sensing*, pp. 801221–801221, International Society for Optics and Photonics, 2011.

[7] A. K. Okyay, A. M. Nayfeh, K. C. Saraswat, T. Yonehara, A. Marshall, and P. C. McIntyre, "High-efficiency metal-semiconductor-metal photodetectors

on heteroepitaxially grown ge on si," *Optics letters*, vol. 31, no. 17, pp. 2565–2567, 2006.

[8] L. Tang, D. A. Miller, A. K. Okyay, J. A. Matteo, Y. Yuen, K. C. Saraswat, and L. Hesselink, "C-shaped nanoaperture-enhanced germanium photodetector," *Optics letters*, vol. 31, no. 10, pp. 1519–1521, 2006.

[9] D. Peters, "An infrared detector utilizing internal photoemission," *Proceedings of the IEEE*, vol. 55, no. 5, pp. 704–705, 1967.

[10] A. Akbari and P. Berini, "Schottky contact surface-plasmon detector integrated with an asymmetric metal stripe waveguide," *Applied Physics Letters*, vol. 95, no. 2, p. 021104, 2009.

[11] A. Akbari, R. N. Tait, and P. Berini, "Surface plasmon waveguide schottky detector," *Optics express*, vol. 18, no. 8, pp. 8505–8514, 2010.

[12] M. W. Knight, H. Sobhani, P. Nordlander, and N. J. Halas, "Photodetection with active optical antennas," *Science*, vol. 332, no. 6030, pp. 702–704, 2011.

[13] A. Sobhani, M. W. Knight, Y. Wang, B. Zheng, N. S. King, L. V. Brown, Z. Fang, P. Nordlander, and N. J. Halas, "Narrowband photodetection in the near-infrared with a plasmon-induced hot electron device," *Nature communications*, vol. 4, p. 1643, 2013.

[14] M. A. Nazirzadeh, F. B. Atar, B. B. Turgut, and A. K. Okyay, "Random sized plasmonic nanoantennas on silicon for low-cost broad-band near-infrared photodetection," *Scientific reports*, vol. 4, 2014.

[15] K. Yu, Y. Tian, and T. Tatsuma, "Size effects of gold nanaoparticles on plasmon-induced photocurrents of gold–tio2 nanocomposites," *Phys. Chem. Chem. Phys.*, vol. 8, no. 46, pp. 5417–5420, 2006.

[16] N. Sakai, Y. Fujiwara, Y. Takahashi, and T. Tatsuma, "Plasmon-resonance-based generation of cathodic photocurrent at electrodeposited gold nanoparticles coated with tio2 films," *ChemPhysChem*, vol. 10, no. 5, pp. 766–769, 2009.

[17] E. Kowalska, O. O. P. Mahaney, R. Abe, and B. Ohtani, "Visible-light-induced photocatalysis through surface plasmon excitation of gold on titania surfaces," *Physical Chemistry Chemical Physics*, vol. 12, no. 10, pp. 2344–2355, 2010.

[18] F. Wu, X. Hu, J. Fan, E. Liu, T. Sun, L. Kang, W. Hou, C. Zhu, and H. Liu, "Photocatalytic activity of ag/tio2 nanotube arrays enhanced by surface plasmon resonance and application in hydrogen evolution by water splitting," *Plasmonics*, vol. 8, no. 2, pp. 501–508, 2013.

[19] K. Chen, X. Feng, R. Hu, Y. Li, K. Xie, Y. Li, and H. Gu, "Effect of ag nanoparticle size on the photoelectrochemical properties of ag decorated tio 2 nanotube arrays," *Journal of Alloys and Compounds*, vol. 554, pp. 72–79, 2013.

[20] Z. Chen, Y. Tang, C. Liu, Y. Leung, G. Yuan, L. Chen, Y. Wang, I. Bello, J. Zapien, W. Zhang, *et al.*, "Vertically aligned zno nanorod arrays sentisized with gold nanoparticles for schottky barrier photovoltaic cells," *The Journal of Physical Chemistry C*, vol. 113, no. 30, pp. 13433–13437, 2009.

[21] H. M. Chen, C. K. Chen, C.-J. Chen, L.-C. Cheng, P. C. Wu, B. H. Cheng, Y. Z. Ho, M. L. Tseng, Y.-Y. Hsu, T.-S. Chan, *et al.*, "Plasmon inducing effects for enhanced photoelectrochemical water splitting: X-ray absorption approach to electronic structures," *ACS nano*, vol. 6, no. 8, pp. 7362–7372, 2012.

[22] S. T. Kochuveedu, D.-P. Kim, and D. H. Kim, "Surface-plasmon-induced visible light photocatalytic activity of tio2 nanospheres decorated by au nanoparticles with controlled configuration," *The Journal of Physical Chemistry C*, vol. 116, no. 3, pp. 2500–2506, 2012.

[23] F. Wang and N. A. Melosh, "Plasmonic energy collection through hot carrier extraction," *Nano letters*, vol. 11, no. 12, pp. 5426–5430, 2011.

[24] S. Grover and G. Moddel, "Applicability of metal/insulator/metal (mim) diodes to solar rectennas," *Photovoltaics, IEEE Journal of*, vol. 1, no. 1, pp. 78–83, 2011.

[25] F. B. Atar, E. Battal, L. E. Aygun, B. Daglar, M. Bayindir, and A. K. Okyay, "Plasmonically enhanced hot electron based photovoltaic device," *Optics express*, vol. 21, no. 6, pp. 7196–7201, 2013.

[26] K. Aydin, V. E. Ferry, R. M. Briggs, and H. A. Atwater, "Broadband polarization-independent resonant light absorption using ultrathin plasmonic super absorbers," *Nature communications*, vol. 2, p. 517, 2011.

[27] M. G. Nielsen, A. Pors, O. Albrektsen, and S. I. Bozhevolnyi, "Efficient absorption of visible radiation by gap plasmon resonators," *Optics express*, vol. 20, no. 12, pp. 13311–13319, 2012.

[28] C. Wadell, T. J. Antosiewicz, and C. Langhammer, "Optical absorption engineering in stacked plasmonic au–sio2–pd nanoantennas," *Nano letters*, vol. 12, no. 9, pp. 4784–4790, 2012.

[29] R. H. Fowler, "The analysis of photoelectric sensitivity curves for clean metals at various temperatures," *Physical Review*, vol. 38, no. 1, p. 45, 1931.

[30] W. Spitzer, C. Crowell, and M. Atalla, "Mean free path of photoexcited electrons in au," *Physical Review Letters*, vol. 8, no. 2, p. 57, 1962.

[31] H. Kanter, "Slow-electron mean free paths in aluminum, silver, and gold," *Physical Review B*, vol. 1, no. 2, p. 522, 1970.

[32] Y.-C. Yeo, P. Ranade, Q. Lu, R. Lin, T.-J. King, and C. Hu, "Effects of high-/spl kappa/dielectrics on the workfunctions of metal and silicon gates," in *VLSI Technology, 2001. Digest of Technical Papers. 2001 Symposium on*, pp. 49–50, IEEE, 2001.

[33] M. Kobayashi, A. Kinoshita, K. Saraswat, H.-S. P. Wong, and Y. Nishi, "Fermi level depinning in metal/ge schottky junction for metal source/drain ge metal-oxide-semiconductor field-effect-transistor application," *Journal of applied physics*, vol. 105, no. 2, p. 023702, 2009.

[34] H. Card and E. Rhoderick, "Studies of tunnel mos diodes i. interface effects in silicon schottky diodes," *Journal of Physics D: Applied Physics*, vol. 4, no. 10, p. 1589, 1971.

[35] W. Gericke and W. Ludwig, "Fowler-nordheim tunneling in mim structures with ultra-thin al2o3 films," *physica status solidi (a)*, vol. 1, no. 1, pp. 189–192, 1970.

[36] D. L. Pulfrey, "Mis solar cells: a review," *Electron Devices, IEEE Transactions on*, vol. 25, no. 11, pp. 1308–1317, 1978.

[37] H. Card and E. Yang, "Mis-schottky theory under conditions of optical carrier generation in solar cells," *Applied Physics Letters*, vol. 29, no. 1, pp. 51–53, 1976.

[38] A. Rogalski, "Infrared detectors: an overview," *Infrared Physics & Technology*, vol. 43, no. 3, pp. 187–210, 2002.

[39] A. Rogalski, "Infrared detectors: status and trends," *Progress in quantum electronics*, vol. 27, no. 2, pp. 59–210, 2003.

[40] W. Anderson, A. Delahoy, and R. Milano, "An 8% efficient layered schottky-barrier solar cell," *Journal of Applied Physics*, vol. 45, no. 9, pp. 3913–3915, 1974.

[41] H. A. Atwater, "The promise of plasmonics," *Scientific American*, vol. 296, no. 4, pp. 56–62, 2007.

[42] K. Catchpole and A. Polman, "Plasmonic solar cells," *Optics express*, vol. 16, no. 26, pp. 21793–21800, 2008.

[43] J. A. Schuller, E. S. Barnard, W. Cai, Y. C. Jun, J. S. White, and M. L. Brongersma, "Plasmonics for extreme light concentration and manipulation," *Nature materials*, vol. 9, no. 3, pp. 193–204, 2010.

[44] G. Lozano, D. J. Louwers, S. R. Rodríguez, S. Murai, O. T. Jansen, M. A. Verschuuren, and J. G. Rivas, "Plasmonics for solid-state lighting: enhanced excitation and directional emission of highly efficient light sources," *Light: Science & Applications*, vol. 2, no. 5, p. e66, 2013.

[45] L. Hirsch, R. Stafford, J. Bankson, S. Sershen, B. Rivera, R. Price, J. Hazle, N. Halas, and J. West, "Nanoshell-mediated near-infrared thermal therapy

of tumors under magnetic resonance guidance," *Proceedings of the National Academy of Sciences*, vol. 100, no. 23, pp. 13549–13554, 2003.

[46] X. Sheng, J. Hu, J. Michel, and L. C. Kimerling, "Light trapping limits in plasmonic solar cells: an analytical investigation," *Optics express*, vol. 20, no. 104, pp. A496–A501, 2012.

[47] S. A. Maier, *Plasmonics: fundamentals and applications: fundamentals and applications*. Springer Science & Business Media, 2007.

[48] K. A. Willets and R. P. Van Duyne, "Localized surface plasmon resonance spectroscopy and sensing," *Annu. Rev. Phys. Chem.*, vol. 58, pp. 267–297, 2007.

[49] S. Nie and S. R. Emory, "Probing single molecules and single nanoparticles by surface-enhanced raman scattering," *science*, vol. 275, no. 5303, pp. 1102–1106, 1997.

[50] C. F. Bohren and D. R. Huffman, "Absorption and scattering by a sphere," *Absorption and Scattering of Light by Small Particles*, pp. 82–129, 1983.

[51] G. Mie, "Pioneering mathematical description of scattering by spheres," *Ann. Phys*, vol. 25, p. 337, 1908.

[52] C. Sonnichsen, T. Franzl, T. Wilk, G. von Plessen, J. Feldmann, O. Wilson, and P. Mulvaney, "Drastic reduction of plasmon damping in gold nanorods," *Physical Review Letters*, vol. 88, no. 7, pp. 077402–077402, 2002.

[53] J. Hofmann and W. Steinmann, "Plasma resonance in the photoemission of silver," *physica status solidi (b)*, vol. 30, no. 1, pp. K53–K56, 1968.

[54] J. Endriz and W. Spicer, "Surface-plasmon-one-electron decay and its observation in photoemission," *Physical Review Letters*, vol. 24, no. 2, p. 64, 1970.

[55] J. Lehmann, M. Merschdorf, W. Pfeiffer, A. Thon, S. Voll, and G. Gerber, "Surface plasmon dynamics in silver nanoparticles studied by femtosecond time-resolved photoemission," *Physical review letters*, vol. 85, no. 14, p. 2921, 2000.

[56] T. P. White and K. R. Catchpole, "Plasmon-enhanced internal photoemission for photovoltaics: Theoretical efficiency limits," *Applied Physics Letters*, vol. 101, no. 7, p. 073905, 2012.

[57] C. Berglund and W. Spicer, "Photoemission studies of copper and silver: experiment," *Physical Review*, vol. 136, no. 4A, p. A1044, 1964.

[58] T. Inagaki, K. Kagami, and E. Arakawa, "Photoacoustic observation of nonradiative decay of surface plasmons in silver," *Physical Review B*, vol. 24, no. 6, p. 3644, 1981.

[59] A. J. Leenheer, P. Narang, N. S. Lewis, and H. A. Atwater, "Solar energy conversion via hot electron internal photoemission in metallic nanostructures: Efficiency estimates," *Journal of Applied Physics*, vol. 115, no. 13, p. 134301, 2014.

[60] L. Du, A. Furube, K. Hara, R. Katoh, and M. Tachiya, "Ultrafast plasmon induced electron injection mechanism in gold–tio 2 nanoparticle system," *Journal of Photochemistry and Photobiology C: Photochemistry Reviews*, vol. 15, pp. 21–30, 2013.

[61] L. Du, A. Furube, K. Yamamoto, K. Hara, R. Katoh, and M. Tachiya, "Plasmon-induced charge separation and recombination dynamics in gold-tio2 nanoparticle systems: dependence on tio2 particle size," *The Journal of Physical Chemistry C*, vol. 113, no. 16, pp. 6454–6462, 2009.

[62] Y. Tian, X. Shi, C. Lu, X. Wang, and S. Wang, "Charge separation in solid-state gold nanoparticles-sensitized photovoltaic cell," *Electrochemistry Communications*, vol. 11, no. 8, pp. 1603–1605, 2009.

[63] M. Nazirzadeh, F. B. Atar, B. B. Turgut, and A. K. Okyay, "Ultra-low-cost near-infrared photodetectors on silicon," in *SPIE OPTO*, pp. 93671I–93671I, International Society for Optics and Photonics, 2015.

[64] R. A. Ismail, A. Al-Naimi, and A. A. Al-Ani, "Studies on fabrication and characterization of a high-performance al-doped zno/n-si (1 1 1) heterojunction photodetector," *Semiconductor Science and Technology*, vol. 23, no. 7, p. 075030, 2008.

[65] J. Kimling, M. Maier, B. Okenve, V. Kotaidis, H. Ballot, and A. Plech, "Turkevich method for gold nanoparticle synthesis revisited," *The Journal of Physical Chemistry B*, vol. 110, no. 32, pp. 15700–15707, 2006.

[66] K.-C. Lee, S.-J. Lin, C.-H. Lin, C.-S. Tsai, and Y.-J. Lu, "Size effect of ag nanoparticles on surface plasmon resonance," *Surface and Coatings Technology*, vol. 202, no. 22, pp. 5339–5342, 2008.

[67] S. M. Sze and K. K. Ng, *Physics of semiconductor devices*. John Wiley & Sons, 2006.

[68] W. Li and J. Valentine, "Metamaterial perfect absorber based hot electron photodetection," *Nano letters*, vol. 14, no. 6, pp. 3510–3514, 2014.

[69] P. B. Johnson and R.-W. Christy, "Optical constants of the noble metals," *Physical Review B*, vol. 6, no. 12, p. 4370, 1972.

[70] E. D. Palik, *Handbook of optical constants of solids*, vol. 3. Academic press, 1998.

[71] S. V. Zhukovsky, V. E. Babicheva, A. V. Uskov, I. E. Protsenko, and A. V. Lavrinenko, "Electron photoemission in plasmonic nanoparticle arrays: analysis of collective resonances and embedding effects," *Applied Physics A*, vol. 116, no. 3, pp. 929–940, 2014.

[72] G. Moddel and S. Grover, *Rectenna Solar Cells*. Springer, 2013.

[73] N. Shinohara, "Power without wires," *Microwave Magazine, IEEE*, vol. 12, no. 7, pp. S64–S73, 2011.

[74] F. Wang and N. A. Melosh, "Theoretical analysis of hot electron collection in metal-insulator-metal devices," in *SPIE Solar Energy+ Technology*, pp. 81110O–81110O, International Society for Optics and Photonics, 2011.

[75] C. Scales and P. Berini, "Thin-film schottky barrier photodetector models," *Quantum Electronics, IEEE Journal of*, vol. 46, no. 5, pp. 633–643, 2010.

[76] J. Fisher and I. Giaever, "Tunneling through thin insulating layers," *Journal of Applied Physics*, vol. 32, no. 2, pp. 172–177, 1961.

[77] T. Bright, J. Watjen, Z. Zhang, C. Muratore, and A. Voevodin, "Optical properties of hfo 2 thin films deposited by magnetron sputtering: From the visible to the far-infrared," *Thin Solid Films*, vol. 520, no. 22, pp. 6793–6802, 2012.

[78] Y.-C. Chang, S.-M. Wang, H.-C. Chung, C.-B. Tseng, and S.-H. Chang, "Observation of absorption-dominated bonding dark plasmon mode from metal–insulator–metal nanodisk arrays fabricated by nanospherical-lens lithography," *Acs Nano*, vol. 6, no. 4, pp. 3390–3396, 2012.

[79] Y. Lu, Y. Yin, Z.-Y. Li, and Y. Xia, "Synthesis and self-assembly of au@ sio2 core-shell colloids," *Nano Letters*, vol. 2, no. 7, pp. 785–788, 2002.

[80] E. Mine, A. Yamada, Y. Kobayashi, M. Konno, and L. M. Liz-Marzán, "Direct coating of gold nanoparticles with silica by a seeded polymerization technique," *Journal of colloid and interface science*, vol. 264, no. 2, pp. 385–390, 2003.

[81] F. P. Garcia de Arquer, A. Mihi, D. Kufer, and G. Konstantatos, "Photoelectric energy conversion of plasmon-generated hot carriers in metal–insulator–semiconductor structures," *ACS nano*, vol. 7, no. 4, pp. 3581–3588, 2013.

[82] N. J. Halas, S. Lal, W.-S. Chang, S. Link, and P. Nordlander, "Plasmons in strongly coupled metallic nanostructures," *Chemical reviews*, vol. 111, no. 6, pp. 3913–3961, 2011.

[83] E. Prodan, C. Radloff, N. J. Halas, and P. Nordlander, "A hybridization model for the plasmon response of complex nanostructures," *Science*, vol. 302, no. 5644, pp. 419–422, 2003.